Background Reduction in Gamma Beam Experiments Using Segmented Germanium Detectors

Thesis submitted in accordance with the requirements of
University of Liverpool for the degree of Doctor of Philosophy by

FAN ZHU

Department of Physics, University of Liverpool
August 2023

Acknowledgement

Completing a PhD is a monumental achievement, and I still find it hard to believe that I have reached this milestone (extra marks for doing this in different countries!). Here, I want to raise a toast to everyone who has been a part of this incredible journey with me. This work would have been never possible without the help of many people, especially during the Covid-19 pandemic.

First and foremost, I would like to thank my supervisor, Prof. Rolf-Dietmar Herzberg. Thank you for your invaluable guidance, support and encouragement throughout my PhD journey. your unwavering belief in my abilities and encouragement have been instrumental in bringing this thesis to fruition. Also, equal gratitude to my other supervisors, Prof. David Joss and Dr. Călin Alexandru Ur. Having your help and support during my research has been an absolute privilege.

I would like to thank the whole nuclear physics group here at the University of Liverpool, both past and present. I have been so lucky to be surrounded by some of the most incredible genius in the field. A huge thanks also go to the GDED group in ELI-NP, Romania. The experience of working in ELI-NP has been a precious gift to me, it was not easy but inspired and motivated me to grow as a person.

It's hard to express how fortunate I feel for the opportunity to collaborate with such amazing people, but still I would like to thank all my friends both in the PhD office (both Liverpool and ELI-NP) and at home in China, and of course my mum and dad. Special thanks to my loving boyfriend and best friend, Dr. Hongzhi Chen. Thank you for all the support and love, as you said, welcome to my graduation.

致父母：寸草春晖，难以为报。谢师恩：师者如光，揖礼还授。
敬挚友：愿岁并谢，与友长兮。愿自己：一生坦荡，天天开心。
行文至此，已是深夜，异乡求学，一晃八年，百感交集，思绪万千，落笔为终。

Abstract

ELIADE is a new gamma-ray detector array being developed for installation at the new under construction, Extreme Light Infrastructure Nuclear Physics (ELI-NP) facility in Magurele, Romania. It is composed of eight segmented HPGe clover detectors and additional four $CeBr_3$ detectors. It will be fitted with passive lead shielding and segmented Comption-suppression shields when completed. The combined operation of both a ELIADE detector and a suppression shield has been tested. The focus of this work is the GEANT4 simulations of segmented clover Germanium detector in the ELI-NP experimental conditions of high intensity with a spectral density higher than 0.5 x 10^4 photons/eV/s and high degree of linear polarization at more than 95%., the study of the experimental setups and the associated background radiation sources, and the study of the compromise between adding absorbers/active shielding to the array and the use of detector segmentation. The performance of measurements and simulation based optimisation of segmented clover HPGe detector is presented in this thesis. A complete and validated model of ELIADE geometry in the simulation toolkit GEANT4 along with a set of measurements of the ELIADE array detectors with standard calibration sources ^{60}Co, ^{22}Na, ^{152}Eu, ^{137}Cs and a plutonium-beryllium neutron source which is available at the Horia Hulubei National Institute of Physics and Nuclear Engineering, Romania, is presented. Peak to total ratios, relative photopeak efficiencies, and energy resolution functions have been determined in order to characterise the performance of ELIADE. The information was then used to refine a GEANT4 simulation of the full detector array. This model will help to design Nuclear Resonance Fluorescence (NRF) experiments for forthcoming experimental campaigns at ELI-NP using gamma beams from 2023.

Contents

List of Figures

List of Tables

Chapter 1

Introduction

Photon scattering experiments provide a unique insight into the inner workings of atomic nuclei. The purely electromagnetic detector allows the model-independent extraction of observables, such as energies and lifetimes across a wide range of excitation energy. This allows systematic studies of the dipole response of nuclei from low-lying collective excitation, such as the scissors mode, all the way up to the giant resonances located above the neutron separation threshold.

To perform such experiments one needs a tunable source of photons and a sensitive detection system. Here the photon source is provided by the new Extreme Light Infrastructure Nuclear Physic (ELI-NP) facility, while the detection system, the ELIADE (ELI Array of DEtectors), is the subject of the present thesis.

The initial demonstration of Nuclear Resonance Fluorescence (NRF) was finally reported by Moon et al. [Moo51], who successfully addressed the energy loss caused by photon recoil. They achieved this by utilising a high-speed centrifuge to induce a Doppler up-shift in the energy of gamma-ray photons emitted from the gamma-ray source. In 1958, the NRF process garnered significant attention when Goldhaber et al. [MS58] conducted a clever experiment involving gamma-ray photons from the weak decay of the radioisotope ^{152}Eu. They were able to establish the negative helicity of the neutrino. In that same year, Mößbauer discovered recoilless gamma-ray emission and subsequent resonance absorption, a phenomenon known as Mößbauer spectroscopy [Mös58]. This breakthrough established a new and highly accurate method for studying atomic hyperfine interactions, leading to

numerous applications in atomic or molecular physics, chemistry, geology, biology, material sciences, and fundamental physics. Notably, it enabled the first terrestrial test of the gravitational red-shift predicted by Einstein's general theory of relativity, performed by Pound and Rebka [PJ60].

The challenge of recoil-energy detuning was overcome by the use of continuous-energy photon beams, such as bremsstrahlung. The concept of utilising bremsstrahlung for nuclear reactions was initially proposed by Schiff in 1946 [Sch46]. It was not until a decade later that Hayward and Fuller achieved the first observation of Nuclear Resonance Fluorescence (NRF) induced by a bremsstrahlung beam [HF57]. The availability of high-current, high-duty factor electron accelerators facilitated the generation of intense bremsstrahlung sources for photonuclear reactions. In the energy range under discussion, various bremsstrahlung facilities worldwide conducted studies on NRF, photofission, and photoactivation experiments.

As early as 1959, Metzger published a review article providing an overview of these activities [Met59]. In the 1980s, the NRF research gained momentum with the discovery of the low-energy M1 nuclear scissors mode by Richter and his team at Darmstadt [Boh+84]. Subsequently, Kneissl and collaborators have regularly updated the field's progress through review articles [BK87b], [UZ96], [UZ06].

Researchers have long desired a tunable quasi-monochromatic source of gamma-rays in the MeV range. In the 1960s, attempts were made using positron annihilation-in-flight [FF61] and tagged photons [JA62]. However, these sources were either lacking in intensity or monochromaticity. In the 1990s, significant advancements were made in the development of tunable quasi-monochromatic gamma-ray sources based on elastic scattering. This involved intense photon beams from high-intensity lasers colliding head-on with highly-relativistic electron beams. These processes, known as Laser Compton Backscattering (LCB), currently provide the most brilliant sources of photons in the gamma-ray energy range. Importantly, experimentalists have control over parameters such as energy, bandwidth, time structure, and polarization.

A proof-of-principle demonstration of Nuclear Resonance Fluorescence (NRF) studies using LCB photon beams was conducted by Ohgaki et al. in 1994 [Ohg+94]. Over time, the NRF technique with LCB photon beams evolved into a superior method for exploring

nuclear structure discoveries [PB02], [Pie+02b], [Po03], [Wel+09]. This progress was realised with the instrumental advancements of LCB beams at the High Intensity gamma-ray Source (HIγS) at the Duke Free Electron Laser Laboratory (DFELL) [LM96], [Lit+98].

Following the initial Nuclear Resonance Fluorescence (NRF) experiments at the HIγS facility in 2001, NRF studies on nuclear structure became a significant focus of the photonuclear program at HIγS [PB02], [Pie+02b], [Po03]. Recently, a notable breakthrough was achieved by Löher et al.[Loh+13], who successfully operated a γ-γ-coincidence spectroscopy setup at the LCB photon beam at HIγS. This development allows for the combination of an intense mono-energetic photon beam, which determines the excitation energy, with gamma-gamma coincidence spectroscopy for studying the decay behavior of photo-excited states in detail. The experiences and scientific findings accumulated over the past decade [Wel+09], [Loh+13], [Pie+02a], [Fra+04], [Sav+05], [Li+06], [Pie+09], [Ton+10] clearly demonstrate the substantial scientific potential of an NRF experimental facility at a next-generation LCB source, such as the one at ELI-NP.

The ELI-NP facility plans to provide the most exceptional high-energy gamma beams worldwide, featuring unparalleled bandwidth and spectral density. However, achieving such performance necessitates a complex time structure, placing significant demands on the detectors employed for experiments. The ELIADE array, designed for Nuclear Resonance Fluorescence experiments with applications in both fundamental research and practical usage, comprises eight segmented high-purity Germanium clover detectors and four large CeBr3 scintillation detectors. By utilising segmented clover detectors, the aim is to minimise the potential influx of photons reaching the detector while maintaining the overall efficiency of the system. Although the detectors respond straightforwardly to NRF photons emitted by the target, investigating the beam-related background proves more intricate due to the vast number of photons generated within the target, surrounding structural materials, and the temporal characteristics of the beam. This study aims to meticulously examine the background and develop digital data filtering techniques for the ELIADE array, optimising the utilisation of the designated beam time. Also different approaches by using the segmentation of HPGe detector and Compton suppression is developed.

Details about the Variable Energy Gamma rAy (VEGA) system and ELIADE array is presented in chapter 3 and chapter 5. The test of a prototype ELIADE detector and

Compton suppression is presented in chapter 4. A GEANT4 simulation is presented in chapter 6. Two optimisation schemes regarding segments add-back and Compton suppression were developed and will be discussed in chapter 7.

The project primarily centers around simulating the segmented clover Germanium detector using GEANT4 software under the experimental conditions of the ELI-NP facility, which involves a highly intense gamma beam. The objectives include examining the experimental setups and the various sources of background radiation. Additionally, the project aims to investigate the trade-off between incorporating absorbers or active shielding into the array and utilising detector segmentation.

Chapter 2

Principles of radiation detection

The fundamental operation of a semiconductor detector relies on the generating of an electric signal that corresponds to the energy of the incoming radiation. To investigate the properties of the nucleus, it is necessary to analyze the resulting by-products from nuclear reactions. This study specifically focuses on the field of gamma-ray spectroscopy. A comprehensive understanding of the interaction mechanisms between photons and matter as well as the basic principles of radiation detection, is crucial for effectively interpreting the detector's response function.

In this chapter, the following topics will be discussed: the interaction of gamma rays with matter and the generation of the secondary charge carriers; the material and features of germanium detectors; the signal generation process and detector operational characteristics.

2.1 Interaction of gamma rays with matter

Gamma-rays interact with matter in a number of possible ways depending on their energy (Figure 2.1). For the energy range of interest in this work, the important interactions in radiation are:

- photoelectric absorption.
- Compton scattering, and
- pair production

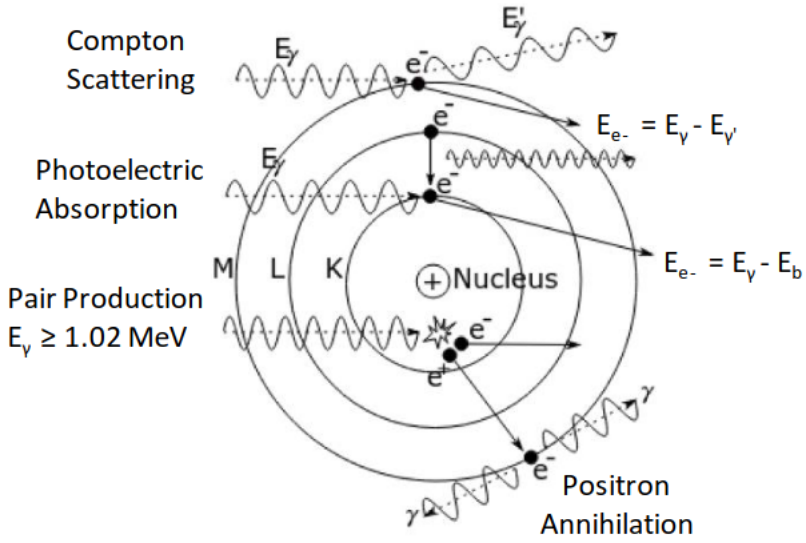

Figure 2.1: Gamma-ray interactions with atomic electrons (PA, CS) and the nuclear field (PP). (Adapted from Knoll)

2.1.1 Photoelectric absorption

The incident photon of energy E_γ is absorbed by an atomic electron. The photoelectron ionised, and its kinetic energy is given by

$$E_e = E_\gamma - E_b, \tag{2.1}$$

where E_b is the binding energy of the electron in its atomic shell. Besides generating the photoelectron, the interaction also results in the production of an ionised atom that emits characteristic x-rays as it undergoes de-excitation.

When it comes to gamma rays (or x-rays) with low energy levels, the photoelectric process is the primary method of interaction. This process is even more effective when the absorber material has a high atomic number Z. Although there is no single mathematical formula that applies to the probability of photoelectric absorption per atom across all ranges of E_γ

and Z, but a rough estimate can be given by the crosses section τ [Kno10]:

$$\tau = constant \times \frac{Z^n}{E_\gamma^{3,5}}, \tag{2.2}$$

where Z is the atomic number of the absorber material, E_γ is the energy of the photon, and n is a constant depending on the energy varies between 4 and 5 over the gamma-ray energy region of interest. This indicates that higher Z materials are preferred in detectors as they are more likely to absorb the gamma rays through photoelectric absorption.

2.1.2 Compton scattering

The incident photon is scattered by an atomic electron, which receives part of the photon energy during the interaction. After being scattered at an angle θ, the photon's energy can be calculated using the Compton scattering formula, Eq 2.3. As the excited atom returns to its stable state, x-rays are released. The Compton scattering formula outlines the correlation between the energies of the gamma-rays (incident E_γ and scattered $E_{\gamma'}$) and the scattering angle θ :

$$E_{\gamma'} = \frac{E_\gamma}{1 + \frac{E_\gamma}{m_e c^2}(1 - \cos\theta)}, \tag{2.3}$$

where $m_e c^2$ is the rest mass energy of the electron. The energy transferred to the electron during the scattering process is given by

$$E = E_\gamma - E_{\gamma'} - E_b. \tag{2.4}$$

In general, $E_b \ll E$ and is therefore neglected in the calculation of the energy transferred to the electron.

The angular distribution of scattered gamma rays as a function of the scattering angle θ can be described using the Klein-Nishina differential cross section formula [Kno10]:

$$\frac{d\sigma}{d\Omega} = Z r_0^2 \left(\frac{1}{1 + \alpha(1 - \cos\theta)}\right)^2 \left(\frac{1 + \cos\theta^2}{2}\right) \left[1 + \frac{\alpha^2(1 - \cos\theta)^2}{(1 + \cos\theta^2)[1 + \alpha(1 - \cos\theta)]}\right], \tag{2.5}$$

where $\alpha \equiv E_\gamma / m_e c^2$ and r_0 is the classical electron radius (2.817×10^{-13} cm). Figure 2.2 shows the angular distribution of Compton scattered gamma-rays with incidence from the left. Forward scattering probability increases with gamma-ray energies.

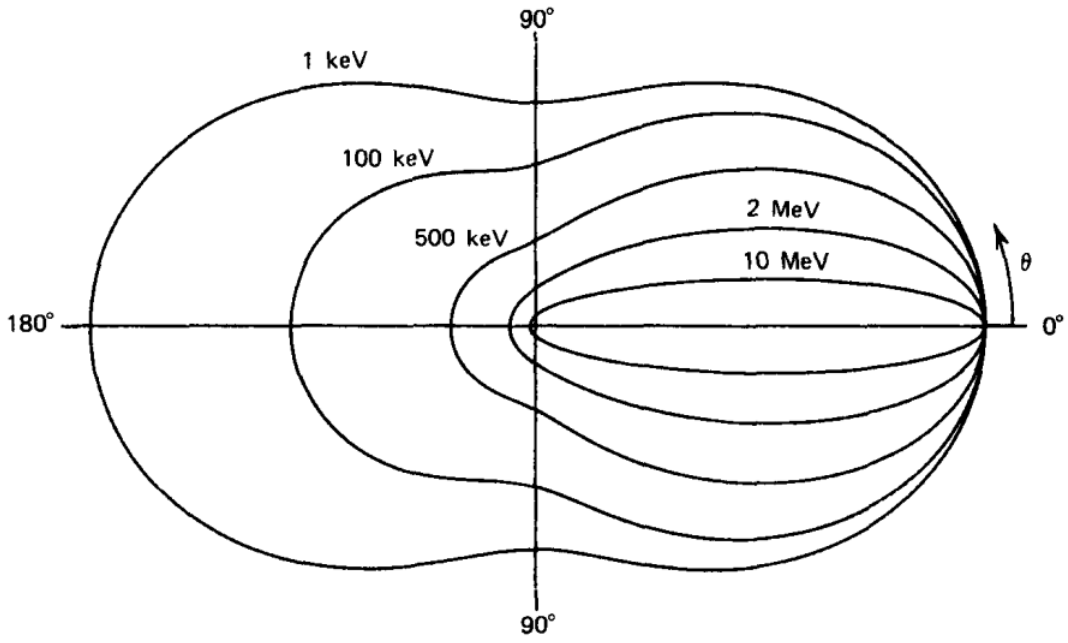

Figure 2.2: A polar plot of the number of photons (incident from the left) Compton scattered into a unit solid angle at the scattering angle θ. The curves are shown for the indicated initial energies. (from [Knoll])

2.1.3 Pair production

According to quantum mechanics, the phenomenon known as pair production occurs when a photon, with an energy equal to or greater than twice the rest mass energy of an electron (1.022 MeV), interacts directly with the Coulomb field of a nucleus (see Figure 2.1). During this interaction, the high-energy photon ceases to exist, and instead, a pair consisting of an electron and its antiparticle, the positron, is generated. The positron, having a limited range, decelerates as it moves through matter until it reaches thermal equilibrium. Eventually, it will annihilate when it encounters a free electron, resulting in the emission of two gamma rays with an energy of 511 keV each, propagating in opposite directions.

Figure 2.3 shows the relative importance of the three main types of gamma-ray interaction for different absorber materials and gamma-ray energies. For the VEGA system that will be installed in ELI-NP, energies of interest are particularly in higher range (up to 19.5 MeV), Compton scattering is the dominant interaction around 5 MeV, and pair production dominants in 5 - 20 MeV.

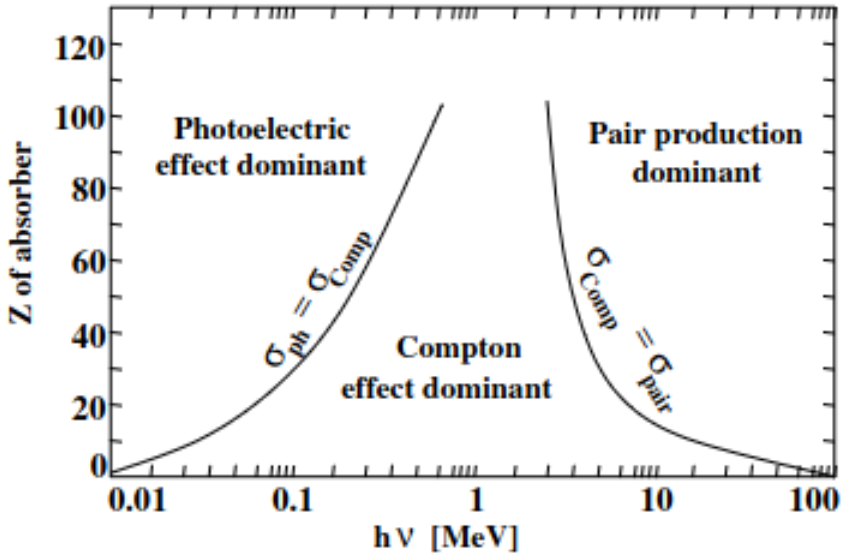

Figure 2.3: The relative importance of the three major types of gamma-ray interaction. The lines show the values of Z and $h\nu$ for which the two neighboring effects are just equal. (from [Knoll])

2.1.4 Attenuation coefficients

Each interaction process within the system eliminates the gamma-ray photon from the beam through absorption or scattering, causing it to deviate from the detector's direction. These processes can be defined by a consistent probability of occurrence per unit path length traveled through the absorber. The combined probabilities of these interactions represent the overall probability per unit path length that the gamma-ray photon will be

taken out of the beam:

$$\mu = \sigma(\text{photoelectric}) + \sigma(\text{Compton}) + \sigma(\text{pair}), \tag{2.6}$$

and is called the *linear attenuation coefficient*. This linear attenuation coefficient describes the fraction of a beam of x-rays or gamma rays that is absorbed or scattered per unit thickness of the absorber.

As the relative importance of the photoelectric absorption effect, Compton scattering and pair production interaction processes are shown in Figure 2.1. The *total absorption coefficient*, which is the probability for an interaction per unit length, and is obtained by multiplying σ by the density of atoms N:

$$\mu = N\sigma = \left(\frac{N_\alpha \rho}{A}\right)\sigma, \tag{2.7}$$

where: N_α is Avogadro's number, ρ is the material density and A is the molecular weight. The fraction of photons transmitted through a thickness, t, of material is then given by

$$I = I_0 e^{-\mu t}, \tag{2.8}$$

where: I is the number of transmitted photons, and I_0 is the number of photons without an absorber.

The *mean free path* λ of gamma-ray photons refers to the average distance travelled in the absorber before an interaction occurs. It can be calculated as:

$$\lambda = \frac{\int_0^\infty x e^{-\mu x}}{\int_0^\infty e^{-\mu x}} = \frac{1}{\mu}, \tag{2.9}$$

and it is simply the reciprocal of the total absorption coefficient. The value of λ typically ranges from a few millimeters to tens of centimeters in solids for common gamma-ray energies.

2.2 Production of charge carriers

In the preceding section, it was emphasised that when gamma radiation is absorbed, it generates one or more highly energetic electrons. These electrons subsequently dissipate their energy within the material by producing additional charged particles. Since the range of primary electrons in germanium, even at energies exceeding several hundred keV, is less than a millimeter, the creation of secondary charge carriers is considered to be a localised phenomenon. [TMu76] The energy loss is influenced by two mechanisms:

- the process of ionisation and excitation resulting from collisions with atomic electrons
- the emission of electromagnetic radiation (known as Bremsstrahlung) caused by scattering in the electric field of the nucleus

$$\left(\frac{dE}{dx}\right)_{tot} = \left(\frac{dE}{dx}\right)_{coll} + \left(\frac{dE}{dx}\right)_{rad}. \tag{2.10}$$

The energy loss due to electromagnetic collisions is given by the Bethe-Bloch formula [Leo94]:

$$-\left(\frac{dE}{dx}\right)_{coll} = \frac{2\pi e^4 NZ}{m_e v^2}\left(\ln\frac{m_e v^2 E}{2I^2 k}\right), \tag{2.11}$$

where: E is the relativistic energy, m_e is the rest mass, v is the electron moving velocity, Z is atomic number and N is density, $k \equiv 1-\beta^2$ with $\beta \equiv v/c$, and I is the average ionisation and excitation through elastic and inelastic scattering with nuclei and bound atomic electrons.

Below a few MeV energies, the primary contribution to energy loss is through collisions with other particles. At higher energies, however, the low mass of electrons allows for processes to occur. In fact, for energies exceeding tens of MeV, these radiative processes become the dominant factor in energy loss. The specific formula that describes the energy loss through Bremsstrahlung is used to quantify this [Kno10]:

$$-\left(\frac{dE}{dx}\right)_{rad} = \frac{NEZ(Z+1)e^4}{137 m_e^2 c^4}\left(4\ln\frac{2E}{m_e c^2} - \frac{4}{3}\right), \tag{2.12}$$

where $\alpha = 1/137$, E is the initial energy of the electron and $f(Z)$ is a correction factor accounting for the Coulomb interaction of the electron in the field of the nucleus.

The energy loss caused by the radiative term is significantly smaller compared to the energy losses from collisions, and the ratio of the specific energy losses is given approximately by:

$$\frac{(dE/dx)_r}{(dE/dx)_c} \cong \frac{EZ}{700}, \tag{2.13}$$

where E is in units of MeV, For the electrons of interest here such as beta particles or secondary electrons from gamma-ray interactions, typical energies are less than a few MeV.

2.3 Germanium detectors

The understanding of structure and characteristics of the detector materials is helpful for comprehending the observed performance. A summary of the important aspects related to the work in this thesis is presented below.

2.3.1 The choice of materials

Solid-state materials are frequently employed in various radiation detection applications. The advantage of using solid-state detectors, as opposed to gas-filled detectors, lies in their higher density, allowing for smaller detector sizes. While scintillation detectors made from solid-state materials can exhibit high efficiency, they suffer from limited energy resolution due to the substantial energy required to generate the charge carriers responsible for signal generation (approximately 100 eV). Consequently, the number of carriers produced by the interaction of gamma-rays is relatively small, resulting in a significantly lower energy resolution (around 10 %). In contrast, semiconductor materials generate a much larger number of charge carriers, making them superior in terms of energy resolution performance. The distinctive electrical characteristics of semiconductor materials stem from their specific band structure, as shown in Figure 2.4. Unlike metals, which possess a partially filled highest occupied energy band, or insulators, which exhibit a significant energy gap between the valence and conduction bands, semiconductors have a relatively small energy gap of approximately 1 eV.

When it comes to gamma-ray detection in semiconductors, germanium is the preferred material. Germanium has a higher atomic number (Z = 32) compared to silicon (Z = 14),

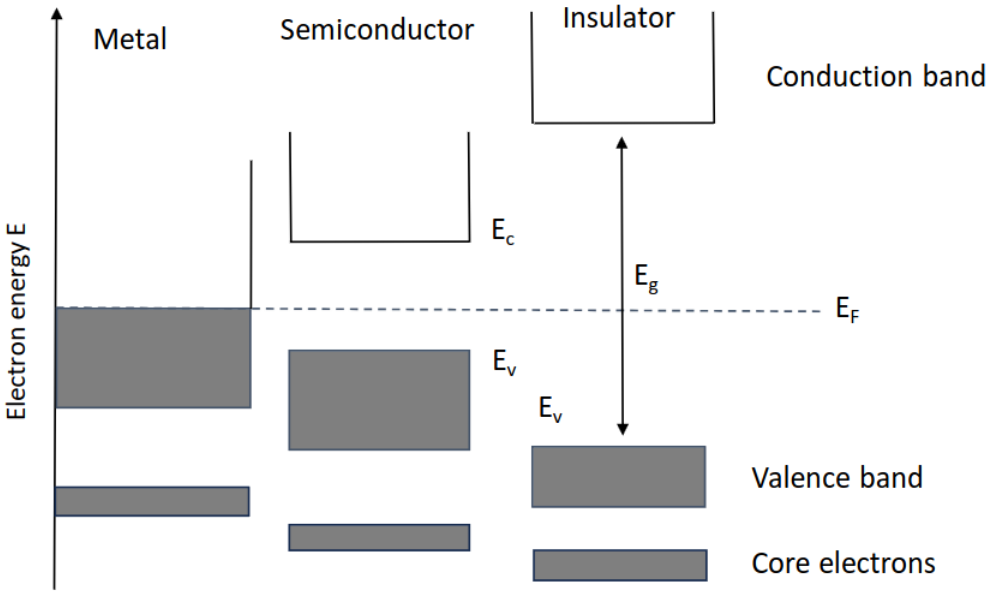

Figure 2.4: Band structure for electrons in metal, semiconductor and insulator. Even at T = 0 K, metals have partially occupied bands (shaded). For semiconductors and insulators the Fermi level lies between the occupied valence band and the unoccupied conduction band.

resulting in a greater attenuation coefficient. Additionally, germanium exhibits a smaller energy gap (at T = 0 K, $E_b = 0.75$ eV) in contrast to silicon ($E_g = 1.17$ eV), thereby leading to improved energy resolution ($\approx 0.3\%$).

2.3.2 Properties of germanium

Germanium, classified as a semiconductor in Group IV, possesses various physical properties outlined in Table 2.1. The crystalline structure of germanium is based on a face-centered cubic (FCC) diamond lattice structure, is depicted in Figure 2.5 and Figure 2.6. Despite being at room temperature, germanium exhibits a small band gap, leading to thermal excitation of electrons into the conduction band, allowing them to move freely. When electrons transition to the conduction band, they leave behind holes in the valence band, forming *electron-hole pairs*. Under the influence of an electric field, the movement of

electrons in the conduction band and holes in the valence band facilitates the flow of electric current.

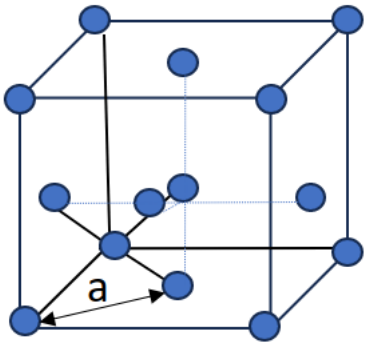

Figure 2.5: Face-centred cubic structure. The lattice constant, a, represents the spacing between the atoms. Adapted from [Whi05]

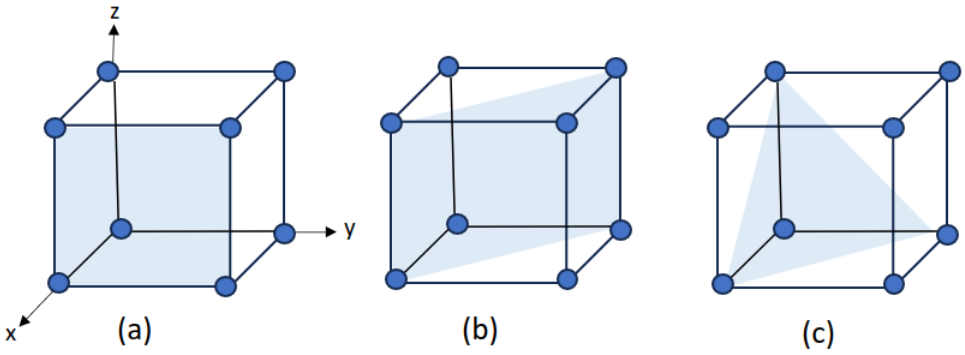

Figure 2.6: Examples of Miller indices which are used to describe crystal planes: (a) (001) plane, (b) (110) plane, (c) (111) plane. Adapted from [Whi05]

Both electrons and holes contribute to the overall conduction of the material. Due to the presence of a non-zero temperature, semiconductors will always contain thermally generated

electron-hole pairs, as indicated by the following equation:

$$p(T) = C \cdot T^{\frac{3}{2}} \cdot e^{(-\frac{E_g}{2kT})}, \tag{2.14}$$

where T is the temperature, E_g is the band-gap energy, k is the Boltzmann constant and C is a constant depending on the material.

Germanium has a narrow energy gap of 0.66 eV, leading to the saturation of the crystal with thermally generated carriers at room temperature. Consequently, Germanium detectors need to be approximately 77 K, equivalent to the temperature of liquid nitrogen (LN2), to eliminate this thermal influence.

Property	**Value**
Atomic number, Z	32
Atomic weight, A	72.6
Atoms/cm^3	4.41×10^{22}
Density	5.32 g/cm^3
Dielectric constant ϵ_r	15.8
Crystal structure	FCC (diamond)
Lattice parameter	5.658 Å
Intrinsic carrier density n_i (300 K)	2.4×10^{13}cm^{-3}
Intrinsic resistivity (300 K)	47 Ωcm
Forbidden energy gap (300 K)	0.665 eV
Forbidden energy gap (0 K)	0.746 eV
Electron mobility, u_n (300 K)	3900 cm^2/V·s
Hole mobility, u_p (300 K)	1900 cm^2/V·s
Electron mobility, u_n (77 K)	3.6×10^4 cm^2/V·s
Hole mobility, u_p (77 K)	4.2×10^4 cm^2/V·s

Table 2.1: Physical properties of Germanium [from Knoll]

2.3.3 The P-N junction

The principles of operation of a semiconductor detector are based on the physical properties of the $p-n$ *junction* (refer to Figure 2.7). The term "junction" refers to the boundary

between two halves of a semiconductor crystal that are doped with different types of impurities. This doping creates variations in the concentration of electrons and holes, as well as differences in the position of the Fermi level in the two regions. Consequently, the band structure of the semiconductor bends, leading to the diffusion of charge carriers in the transition layer.
Specifically, electrons diffuse from the n-side to the p-side, leaving an excess of positively ionised acceptor atoms behind. Conversely, holes diffuse from the p-side to the n-side, leaving an excess of negatively ionised donor atoms. This process results in the creation of a depletion region, also known as a space charge region, where there are no charge carriers present. Additionally, an electric field is generated as a consequence of this charge separation.

The diffusion of charge carriers leads to a slight voltage across the junction known as the contact voltage ($V_c \approx 0.4$ V in the case of Germanium.) By applying a significantly higher bias voltage than the contact voltage (V_b can reach up to 5000 volts for germanium), a reverse biased junction is established. This involves applying a positive voltage to the n-side to attract electrons and a negative voltage to the p-side to attract holes. The resulting electric field propels the induced charge carriers, generating a current.

The Table 2.1 shows the typical electron and hole mobility for germanium. Germanium exhibits significantly higher hole mobility compared to silicon or other semiconductors, indicating that it possesses superior electronic properties among all semiconductors. While there are differences in mobility become comparable in magnitude. This characteristic results in a faster response from germanium detectors.

Compared to other semiconductor materials, germanium exhibits the lowest ionisation energies, At 0 K, it has a band gap of 0.75 eV. Furthermore, the average energy required to generate an electron-hole pair in germanium is 2.96 eV at 77 K. As a result, germanium has a larger number of charge carriers, which is one of the factors contributing to its superior energy resolution in gamma-ray detection.

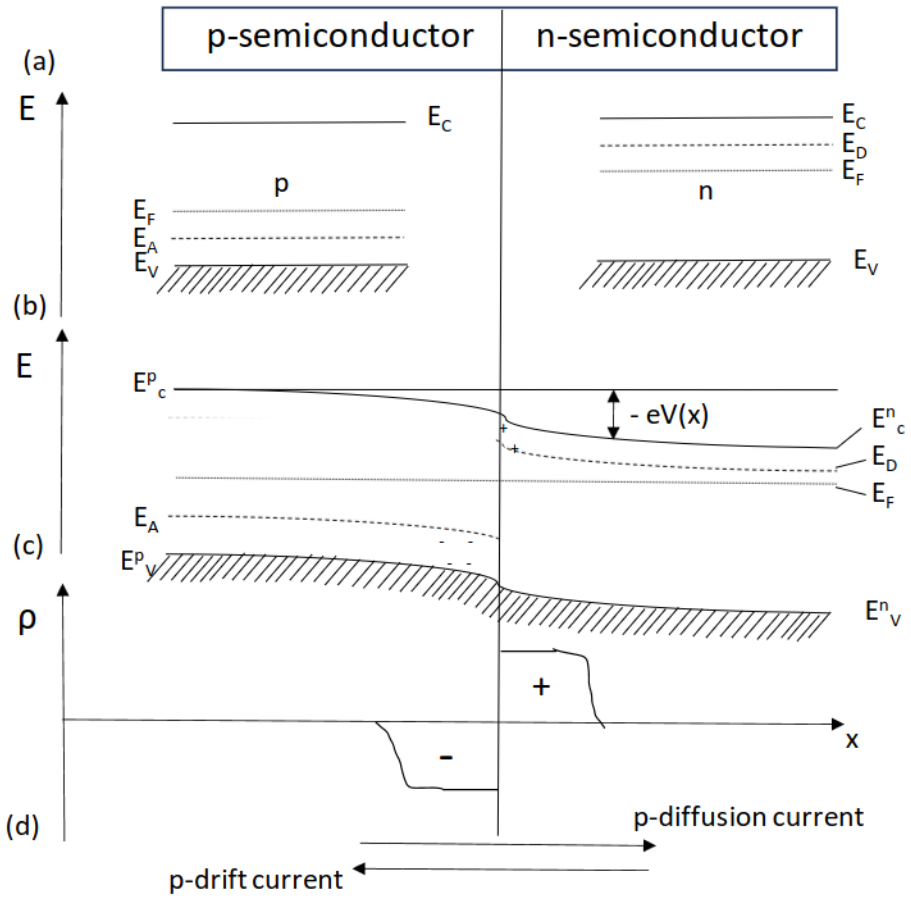

Figure 2.7: Schematic representation of a $p-n$ junction in thermal equilibrium: (a) a semiconductor crystal doped on one side with acceptors (N_A) and on the other side with donors (N_D); (b) band scheme for the n and p sides for the imaginary case of total decoupling of the two sides. E_A and E_D indicate the ground states of the acceptors and donors; E_F is the Fermi level; (c) band scheme of the $p-n$ junction when the two sides are in thermal equilibrium with another. The transition from the p to the n region is assumed to be abrupt. The position of the conduction and valence edges are denoted $E^n_{C,V}$ on the n-side and $E^p_{C,V}$ on the p-side. In the region of the junction an electrostatic potential is induced; (d) The fixed space charge $\rho(x)$ in the region of the junction due to the ionised impurities. This region is free from charge carriers and therefore is also known as the *depletion region*. Adapted from [IL95]

2.3.4 Detector geometry

A radiation detector is based on a fully depleted junction. To effectively stop gamma radiation, the thickness of the depletion region needs to be several centimeters, considering the high penetrability of gamma rays. However, achieving such a depletion volume is challenging with standard germanium due to the inherent impurity concentration in Ge crystals, which is typically around 10^{15} atoms/cm^3. The thickness of the depletion region is inversely proportional to the impurity concentration.

To fabricate a germanium detector, the impurity concentration must be significantly reduced either through advanced refining techniques, allowing for an impurity concentration of approximately 10^{10} atoms/cm^3, or by compensating the material with interstitial lithium donor atoms, known as the *lithium drifting process*. Detectors made from intrinsic germanium are referred to as high-purity germanium (HPGe) detectors, while detectors produced through the lithium drifting process are called Ge(Li) detectors.

One notable advantage of HPGe detectors over Ge(Li) detectors is their larger size and the ability to warm them to room temperature when not in use, as well as the option to perform annealing. On the other hand, Ge(Li) detectors must be constantly maintained at the temperature of liquid nitrogen due to the high mobility of lithium impurities within the germanium material.

The planar configuration, illustrated in the Figure 2.8, is the simplest geometry for a detector. It involves placing two electrodes on the surfaces of a germanium disk. However, this type of detector has a limitation in terms of thickness. It is not feasible to manufacture a detector with an active depth exceeding approximately 2 cm. Consequently, the closed-ended coaxial detector, depicted in Figure 2.9, has become the most widely used detector in nuclear physics experiments.

The closed-ended coaxial detector is constructed using a cylindrical germanium crystal. A portion of the central core is removed to create space or a contact on the inner surface. The second contact is placed on the outer surface. These contacts are formed by doping the germanium crystal through boron implantation for the p+ contact and lithium drifting for the n+ contact. The thickness of the contacts is approximately 0.5 μm and 500 μm,

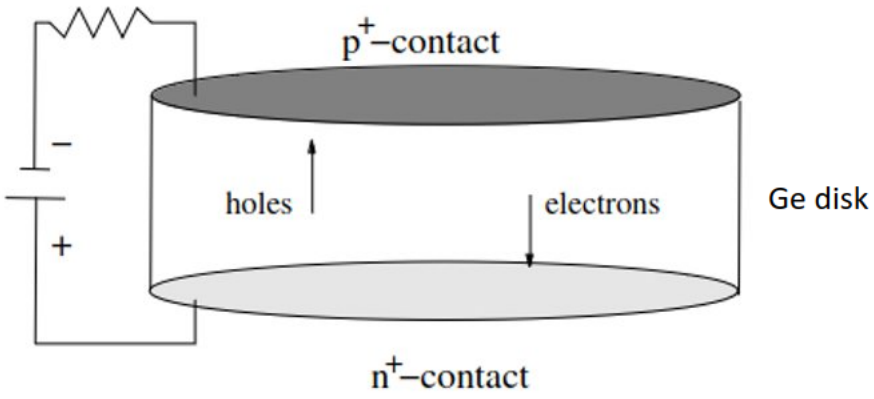

Figure 2.8: Configuration of a planar n-type detector; the n^+ contact is lithium drifted and p^+ one is boron implanted. The secondary charge carriers produced in the depleted region, instead of recombining, drift towards the electrodes, the electrons towards the anode and the holes toward the cathode. [Kno10]

respectively. Due to the greater thickness of the lithium-drifted contact, the n+ electrode is situated inside the hole of the detector, while the p+ electrode is implanted on the exterior. In the bulletised geometry, the front corner of the detector and the core hole are beveled to promote a more even distribution of the electric field lines across the detector volume. To cool the detector to liquid nitrogen temperature, a cold finger is utilised, which is located at the site of the central core.

The coaxial geometry offers several advantages, such as the ability to achieve full depletion in large crystals and relatively low capacitance. However, there is a drawback associated with the electric field distribution within the closed-ended section of the detector. The closed-ended detector can be divided into three distinct parts, each exhibiting different characteristics: a true coaxial part at the back (1), a closed-ended part at the front edge (2), and a circular planar part at the front center (3). Crystal orientation effects are observed in the closed-ended part of the detector due to the weaker electric field present in that region. While n-type and p-type detectors of the same geometry exhibit similar fundamental

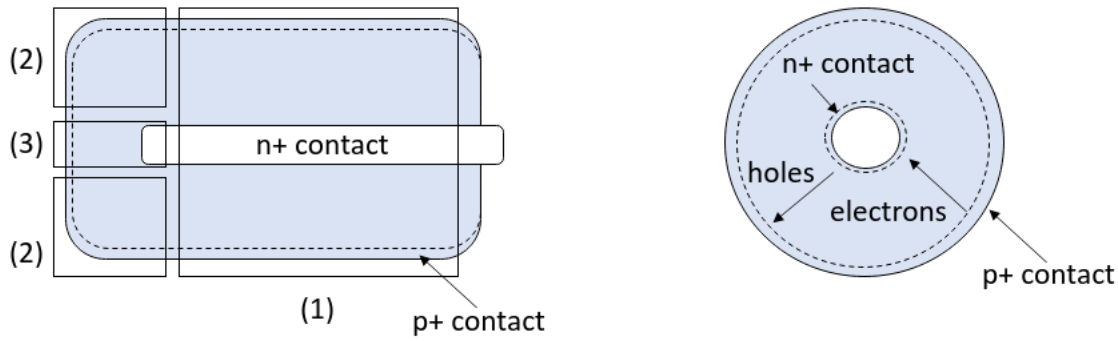

Figure 2.9: Cross section and front view of a n-type coaxial closed-ended bulletised germanium detector; the n+ lithium drifted and p+ boron implanted contacts are indicated.

characteristics such as detection efficiency and energy resolution, the historical preference has been to use n-type germanium. This preference stems from the improved radiation hardness offered by n-type germanium detectors.

2.4 Signal generation process

Within a depleted junction, when gamma-ray interactions generate electron-hole pairs, recombination is avoided, and instead, the charges drift towards the electrodes due to the electric field. As a charge carrier approaches a conducting electrode with a constant electric potential, it induces a current in the external circuit [Dab89]. Ramo [SRa39] resolved the task of calculating the instantaneous value of the induced current. For a planar configuration, he derived a straightforward formula referred to as Ramo's theorem:

$$i(t) = q\frac{\epsilon(x,t)v_d(x,t)}{\psi}. \tag{2.15}$$

Where q represents the charge of the carrier, v_d is the drift velocity of the charge carrier ϵ represents the magnitude of the electric field at the charge's current position, and ψ corresponds to the electric potential of the electrode. x and t are the variables to define the velocity of the charge carriers.

Applying Ramo's theorem to semiconductor junctions is not straightforward due to the non-uniform distribution of the electric field, which is influenced by the space-charge distribution. The validity of Ramo's theorem in semiconductor detectors has been examined by Deshpande [Des70], Vass [Vas70], and Martini [MO69]. To address this, Green's "reciprocity theorem" extends Ramo's theorem and provides the induced charge on one electrode of a multi-electrode device while all other electrodes are grounded (For details please see reference [Rad88a], [KB01]).

Figure 2.10 provides a qualitative illustration of the generation of current pulses in a planar multi-electrode system. It showcases two scenarios in which charges traverse the distance between two electrodes: one represents the accumulation of a net charge, while the other represents the induction of a transient charge without any net charge deposition [Rad88a].

The conductivity of germanium exhibits an anisotropy, meaning that the mobility of electrons and holes varies depending on the orientation of the applied electric field relative to the lattice vectors [Mih+00]. This characteristic has a significant impact on the signal generation process. The literature includes theoretical calculations and simulation results on the anisotropy ([Shi55], [Nat63], [JR83]), while experimental evidence has been observed in studies such as [Ott+75], [Can+74] and [Reg+77]. Germanium is categorised as an indirect band gap semiconductor. Figure 2.11 presents a plot of the calculated band structure of germanium in reciprocal space representation.
The unique arrangement of energy bands in germanium gives rise to its conductivity anisotropy. Figure 2.11 illustrates the variation of electron drift velocity with the electric field for three different orientations relative to the crystallographic directions. It is evident that the drift velocity is influenced by the crystallographic orientation, with the minimum value observed along the (111) direction. Additionally, the drift velocity saturates at electric fields exceeding approximately 10^3 V/cm.

The anisotropy in germanium conductivity has significant implications for two key aspects of the charge collection process:

- the collection time
- the trajectories of the charge carriers

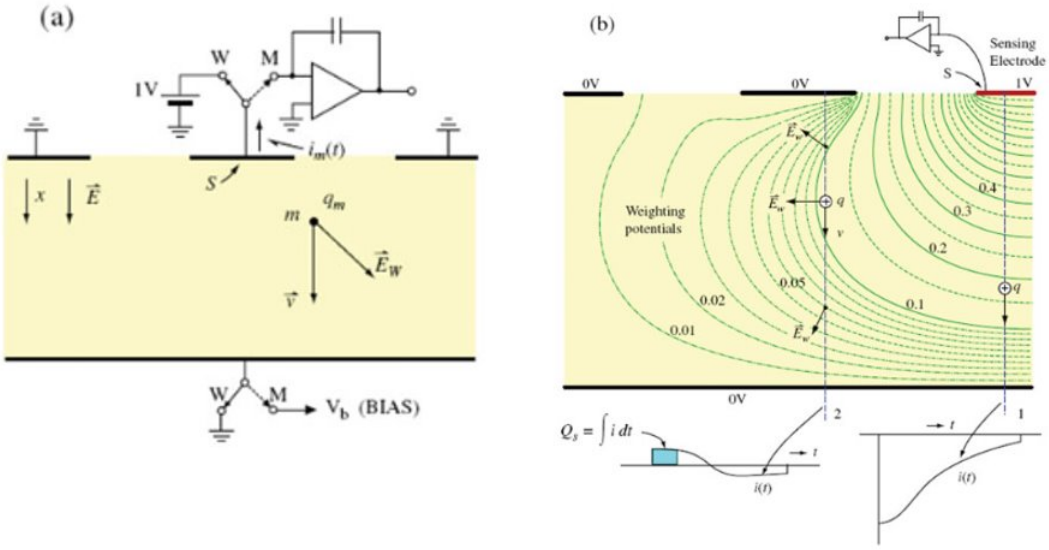

Figure 2.10: Definition of the weighting potential: Solution of the Laplace equation for unity potential at the sensing electrode and zero potential at all other electrodes. (a) Determination of the induced current by the weighting field concept, illustrated on a planar multi-electrode strip configuration. The weighting field is defined conceptually as the field for unity potential on the sensing electrode S (switch in position W) and zero potential on all other electrodes. In actual operation, the sensing electrode is connected to a charge amplifier and uniform operating field is applied to the detector by connecting the opposite electrode to a voltage source (switch in position M). The weighting field calculated numerically for this case is shown as a plot of equipotential lines in (b) for the left half of the electrode structure in (a). Two examples of charge transit from top to bottom are shown.The induced current pulse shapes, resulting from Eq 2.15 for a localised charge moving at a constant velocity, are shown at the bottom of the figure. Note the change in scale of equipotential lines from 0.01/step to 0.05/step. Charge q traversing the full distance between the electrodes along line 1 is observed as Q = -q, while the current decreases with distance from electrode 1, as the electrostatic coupling decreases. For a charge moving along line 2, the induced charge is zero if the measurement time is longer than the transit time. For a short measurement time a net induced charge is observed (the induced current pulse shape is bipolar, since the weighting-field direction changes along the path) [Rad88b]

The first effect is a direct result of the alterations in the drift velocity magnitude and directly impacts the signal shape. On the other hand, the second effect arises from the

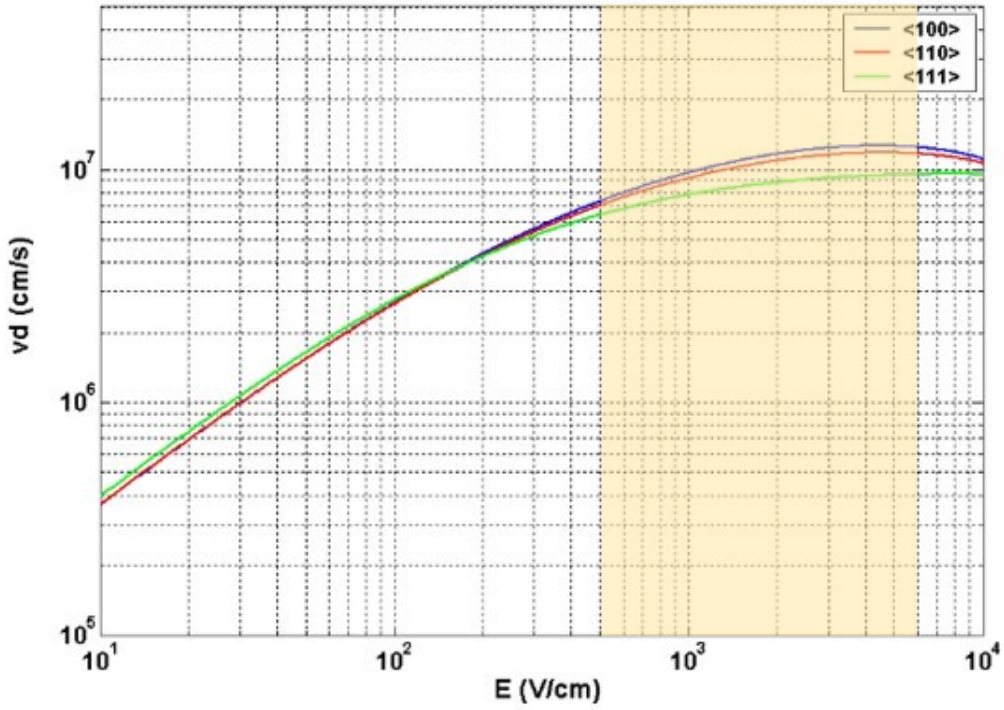

Figure 2.11: Calculated dependence between the drift velocity and the electric field in Germanium along the three main (111), (100) and (110) directions. The differences between the drift velocities are largest for electric fields in the region of around 500 to 6000 V/cm, indicated in Yellow.

fluctuation in the angle between the drift velocity and electric field vectors. This effect holds particular significance in segmented detectors, as it establishes a preferred direction, specifically for charge collection. Figure 2.12 displays the calculated charge trajectories for various drift directions relative to the crystal orientation, as detailed in the previously mentioned reference [Mih+00].

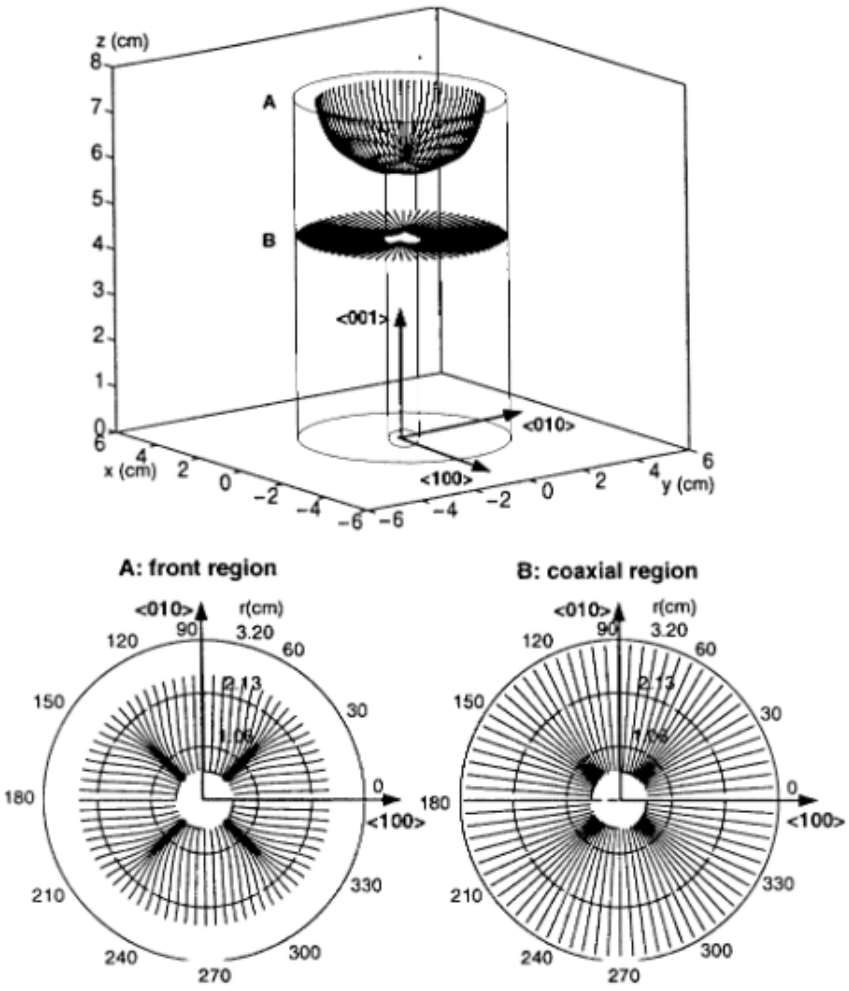

Figure 2.12: Charge carrier trajectories in a closed-end HPGe detector, from interactions of gamma-quanta in the front part (a) and in coaxial part (b) of the Ge detector. The upper drawing shows a full spatial representation, and the lower drawings show front views [Mih+00].

2.5 Detector characteristics

2.5.1 Preamplifier

The objective of the preamplifier is to retrieve the output signals from the detector while minimising any loss in quality and to condition them for further signal processing. There

exist three fundamental categories of preamplifiers: the current sensitive preamplifier, the parasitic preamplifier, and the charge sensitive preamplifier.

In HPGe detectors, where accurate energy determination is crucial, it is essential for the preamplifier to exhibit low noise and consistent sensitivity. To achieve this, a charge-sensitive preamplifier employing a Field-Effect Transistor (FET) is employed. Ideally, the lowest noise levels can be achieved by employing a cooled FET, which is typically positioned within the cryostat. This setup offers the additional advantage of maintaining proximity between the preamplifier and the detector, thereby minimising input capacitance caused by cabling and reducing the likelihood of crosstalk. Crosstalk, in this context, refers to the capacitive coupling between different sections or components of the electronics/circuit.

The stability of the charge-sensitive preamplifier is achieved through the integration of charge on a feedback capacitor, which ensures that the gain remains unaffected by variations in detector capacitance. Subsequently, the integrated charge is discharged through a resistive feedback (RF), resulting in a prolonged pulse decay time. Figure 2.13 depicts a schematic representation of the charge-sensitive preamplifier. This generates a pulse characterised by a rapid initial rise (rise time), representing the duration of charge collection in the detector, followed by a gradual exponential decay (fall time), as illustrated in Figure 2.14. In an ideal scenario, the rise time of the output pulse matches the width of the detector's current pulse.

In order to achieve a quick response, specifically a signal with a brief rise time (RT), a preamplifier with a wide bandwidth (BW) is necessary. The relationship between the rise time of the pulse and the bandwidth of the preamplifier can be deduced by assuming that the preamplifier signal exhibits an exponential decay:

$$V_t = V_0(1 - e^{-t\omega_c}). \tag{2.16}$$

Where V_t is the voltage (i.e. the amplitude of the pulse) at the time t, V_0 is the final voltage and ω_c is the decay constant of the exponential function. Typically, the rise time is defined as the duration between the 10% (t_{10}) and 90% (t_{90}) points of the final amplitude. Taking

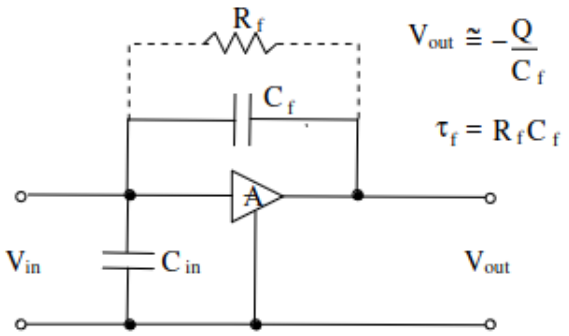

Figure 2.13: Simplified diagram of a resistive feedback charge sensitive preamplifier configuration. The output pulse amplitude is proportional to the charge produced by the gamma-ray interaction. The time constant $R_f C_f$ determines the decay rate of tail of the output pulse (from [Knoll]).

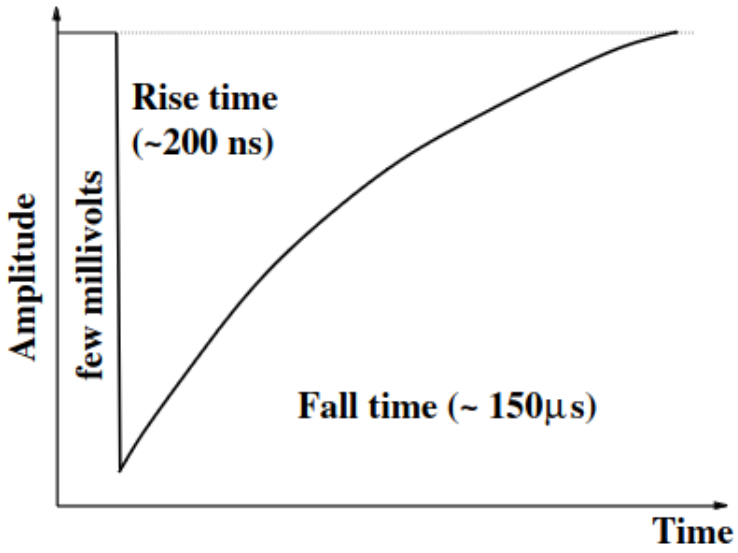

Figure 2.14: Sketch of a preamplifier signal consisting of a fast leading edge and a slow exponential tail.

into account Eq 2.16, we can evaluate the values of t_{10} and t_{90}:

$$0.1V_0 = v_0(1 - e^{-t_{10}\omega_c}) \qquad 0.9V_0 = V_0(1 - e^{-t_{90}\omega_c}), \tag{2.17}$$

and by relating the decay constant to the bandwidth ($\omega_c = 2\ \pi$ BW), we can derive the following equation:

$$RT = t_{90} - t_{10} = \frac{2.2}{2\pi \times BW}. \tag{2.18}$$

Here, the rise time is expressed in seconds and the bandwidth in Hertz (s^{-1}).

The complex electronics employed in segmented detectors, as detailed in the upcoming section, along with the need for a compact cryostat, impose constrains on the size of the preamplifiers and the length of the connection wires. Cross-talk is a common issue encountered with segmented detectors. It occurs when signals from adjacent segments couple together, leading to the detection of a net charge in segments unrelated to the gamma-ray interaction. This problem arises due to inadequate shielding and the crossing of wires from different electronic channels. To mitigate cable capacitance, cross-talk, and the influence of stray electromagnetic fields, a solution is to position the preamplifiers in close proximity to the detector.

2.5.2 Noise performance

Noise encompasses all the random fluctuations that are present alongside the detector signal. It is crucial to comprehend the key sources of noise and their impact on the read-out signal to ensure precise analysis in gamma-ray spectroscopy. In this section, A concise overview of the noise sources in semiconductor detectors will be presented. For a comprehensive examination of this topic, a recommendation referring to the papers authored by Redeka [Rad88a], Dabrowski [Dab89] and Goulding [Gl82].

The signal quality is assessed by the signal-to-noise (S/N) ratio, which determines the minimum amplitude of a distinguishable signal component above the noise level. It is crucial to have a favorable S/N ratio at the initial stage of the signal chain, as any noise generated at this point will be amplified alongside the signal. Both the detector and the electronics contribute to the S/N ratio, particularly the detector capacitance and the field effect transistor (FET) of the preamplifier. In the case of conventional charge-sensitive preamplifiers, the electronic noise is quantified as an equivalent noise charge (ENC), representing the

charge that would produce the same output amplitude [Pei92a]:

$$ENC = A + B \cdot C, \tag{2.19}$$

where A and B are constants depending on the preamplifier, while C is the detector capacitance.

The assessment of noise must also consider the contributions from the leakage current and the bias resistor. The equivalent noise charge resulting from the leakage current can be calculated using the following expression:

$$ENC = \frac{e}{q}\sqrt{\frac{qIT_p}{4}}, \tag{2.20}$$

in this equation, e represents the natural logarithm base, q represents the charge of an electron, I denotes the detector leakage current, and T_p corresponds to the peaking time, which is equivalent to the integration time of the shaper.

The equivalent noise charge (ENC) associated with the bias resistor can be determined using the equation:

$$ENC = \frac{e}{q}\sqrt{\frac{T_p kT}{2R}}, \tag{2.21}$$

where k is the Boltzmann's constant, T denotes the temperature, and R is the value of the bias resistor. Enhancing the detector design to achieve lower detector capacitance, higher bias resistance, and minimal leakage current will result in an improved signal-to-noise ratio.

Noise sources in semiconductor detectors can be categorised as either parallel or series noise, depending on their coupling with the signal [GJ98]. For instance, fluctuations in the leakage current and the gate-source current of the FET are considered parallel noise sources, while noise associated with series resistances and the thermal noise of the input FET are classified as series noise sources. It is worth noting that although the signal's frequency band is narrow, both series and parallel noise components have broad frequency distributions that can be considered uniform or "white." Consequently, high-pass and low-pass filters can be employed to eliminate low and high-frequency noise components without affecting the signal's shape. As a result, it is common practice to analyze the noise characteristics

of a detector using power spectrum and integrated power measurements across different frequencies, employing detailed Fourier analysis techniques [Pre+99].

2.5.3 Energy resolution

The energy resolution of a detector refers to the full width at half maximum (FWHM) of the spectral peak. This measurement assumes that the peak exhibits a Gaussian shape and is free from any background or continuum interference. In the case of a germanium detector, its intrinsic energy resolution is influenced by three main factors:

$$(FWHM)^2_{overall} = (FWHM)^2_{statistical} + (FWHM)^2_{noise} + (FWHM)^2_{drift}. \tag{2.22}$$

- $(FWHM)^2_{statistical}$ is the inherent statistical fluctuation in the number of charge carriers created. This is given by:

  $$(FWHM)^2_{statistical} = (2.35)^2 F \epsilon_{pair} E_\gamma. \tag{2.23}$$

  Where F is the Fano factor, ϵ_{pair} is the ionisation energy, i.e. the energy required to form an electron-hole pair, and E_γ is the gamma-ray energy.

- $(FWHM)^2_{noise}$ is the electronic noise, dominated by the capacitance of the strips of the detector, increases the noise level of the detected pulse, this effect is more prominent in the detection of low-energy gamma rays.

- $(FWHM)^2_{drift}$ depends on the position of the interaction in the detector. This effect is significant in large detector geometries.

Typically, the intrinsic energy resolution of HPGe detector is around 1.7 to 2.3 keV at 1333 keV.

The overall energy resolution of a germanium detector is determined by the combined influence of two factors:

1. the intrinsic energy resolution of the germanium system, denoted as ΔE_{intr} and

2. the contributions resulting from the Doppler effect, denoted as ΔE_{Dopp}.

This can be written as:

$$(\Delta E_{total})^2 = (\Delta E_{intr})^2 + (\Delta E_{Dopp})^2. \tag{2.24}$$

Doppler broadening

The energy spectrum obtained from radiation emitted by fast-moving nuclei exhibits a phenomenon known as a shift and broadening of the spectral lines. This energy shift can be calculated by transforming the frame of reference from the centre of mass (CM) to the laboratory reference system. The calculation is given by the equation [NS79]:

$$E_\gamma = E_\gamma^0 \frac{\sqrt{1-\beta^2}}{1-\beta\cos\theta}, \tag{2.25}$$

where E_γ represents the energy in the laboratory reference system, E_γ^0 represents the energy in the CM system, θ denotes the angle between the scattered projectile and the emitted gamma ray, and $\beta = \mathrm{v/c}$ represents the velocity of the moving nucleus in the laboratory frame (see Figure 2.15). By knowing the emission angle of the gamma-ray, it is possible to recover the relative transition energy.

The observed Doppler broadening is a result of the combination of three factors, which are added together using the quadratic summation. These factors are as follow:

$$(\Delta E_{Dopp})^2 = (\Delta E_{open})^2 + (\Delta E_{ang})^2 + (\Delta E_{vel})^2. \tag{2.26}$$

1. ΔE_{open} represents the broadening due to the geometry of the detector and is influenced by the opening angle, $\Delta\theta$.
$$\frac{\Delta E_\gamma}{E_\gamma} = \frac{\beta\sin\theta}{1-\beta\cos\theta}\Delta\theta. \tag{2.27}$$
It can be reduced by minimising the value of $\Delta\theta$.

2. ΔE_{ang} accounts for the angular spread of the recoiling nuclei, which occurs as a result of the interaction between an ion beam and a solid target. The spread in angular distribution also includes the effect of the size of the beam spot.

3. ΔE_{vel} represents the variation in the recoil velocity, ΔE_γ^{vel}. Since the recoiling nuclei decelerate within the target material, their velocity at the moment of gamma-ray

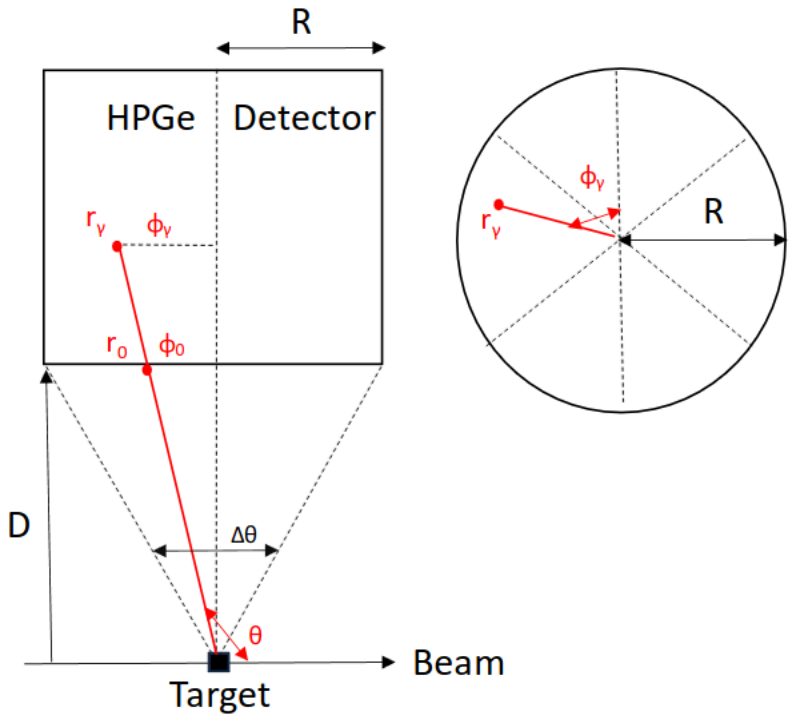

Figure 2.15: The reference system refers to the coordinate system that describes the direction of gamma-ray emission relative to the front face of the detector. In this system, the position of the gamma interaction is denoted by (r_γ, ϕ_γ) and is represented in cylindrical coordinates.

emission is not precisely known. Although the relative variation of recoil velocity is typically around 10% in typical experiments, it is possible to correct for this factor by measuring the velocity of each recoiling nucleus.

By substituting the expression for Doppler broadening into Eq 2.24, the following equation is obtained [Gla98]:

$$\left(\frac{\Delta E_\gamma}{E_\gamma}\right)^2 = \frac{(\Delta E_{intr})^2}{(E_\gamma)^2} + \left(\frac{\beta \sin\theta}{1-\beta\cos\theta}\right)^2 (\Delta\theta)^2 + \left(\frac{-\beta+\cos\theta}{(1-\beta^2)(1-\beta\cos\theta)}\right)^2 (\Delta\beta)^2. \quad (2.28)$$

The Doppler broadening, which contributes to the overall energy resolution of the detector, is more significant for large detectors positioned at a 90° angle relative to the beam direction.

However, this broadening can be mitigated by reducing the detector's opening angle, $\Delta\theta$. One effective approach to achieve this is by segmenting the detectors into smaller parts while maintaining the same total volume.

2.5.4 Efficiency

The evaluation of the counting efficiency of a germanium detector can be done using various primary methods. In this study, we will focus on two specific types: the absolute efficiency and the relative efficiency.

- The absolute efficiency, denoted as ϵ_{abs}, is a measure of the total number of detected events relative to the total number of photons emitted by the source. It takes into account the specific geometry of the detector and the source, as they can influence the efficiency.

- The relative efficiency, referred to as ϵ_{rel}, compares the efficiency of the geranium detector to that of a NaI(Tl) crystal. The NaI(Tl) crystal used for comparison has a diameter of 76 mm and a length of 76 mm, and the measurement is performed at a distance of 25 cm from the source. The relative efficiency is obtained by dividing the absolute efficiency by a factor of 1.244×10^{-3} in the energy of 1332 keV.

When considering counting efficiency, it is important to consider the nature of the detected event. Specifically, the photopeak efficiency focuses on events where the gamma ray deposits its full energy in the detector. The photopeak efficiency, denoted as ϵ_{ph}, can be mathematically expressed as:

$$\epsilon_{ph} = (PT) \times \epsilon_{abs}. \tag{2.29}$$

In this equation, (PT) represents a quality factor known as peak-to-total ratio.

To measure the peak-to-total ratio, a standard procedure involves summing the net peak areas of ^{60}Co and dividing it by the total number of counts in the spectrum within the energy range of 100 keV to 1350 keV. Sometimes, the peak-to-total ratio is also referred to as the peak-to-background ratio.

An additional parameter used to assess the quality of a spectrum is the peak-to-Compton ratio. This ratio is determined by dividing the counts in the highest channel of a photopeak

by the counts in a representative channel of the Compton continuum associated with that peak. Typically, this ratio is reported for the 1332 keV peak of ^{60}Co. The Compton continuum is defined as the energy interval between 1040 keV and 1096 keV.

2.5.5 Time resolution

The time resolution of a germanium detector is typically evaluated by comparing it to a fast scintillator detector equipped with fast analog electronics. A common value for the time resolution of a germanium detector is approximately 5 ns.

2.6 Compton suppressed detectors

Compton suppressed detectors offer a significant enhancement in the peak-to-total ratio. These detectors consist of a germanium crystal surrounded by a Compton suppression shield, resulting in a device known as an escape suppressed spectrometer (ESS), Figure 2.16. The shield is composed of scintillator detectors, typically bismuth germanate (BGO), which placed around the germanium crystal. Their purpose is to detect gamma rays that undergo Compton scattering outside the germanium. These are electronically rejected using an analog electronics timing circuit. The improved spectral quality achieved with a suppressed spectrum is illustrated in Figure 2.17. Typically, the peak-to-total ratio of a suppressed spectrometer is approximately 60%, which is a significant improvement compared to the approximately 20% achieved by an unsurpassed detector [PJ 85].

2.7 Composite detectors and segmentation

Multi-element detectors refer to detectors that have been divided into multiple parts, either physically or electronically, in order to provide multiple output signals. There are two classifications of such detectors:

- Composite detectors: These detectors are composed of multiple germanium crystals that are closely packed together in the same cryostat. Examples of composite detectors include the Clover detector, which consists of four tapered germanium crystals arranged in the shape of a four-leaf clover [PF94], [Duc+92], [Duc+99], [She+99], and the Cluster detector, which comprises seven crystals. The Cluster detector utilises crystal

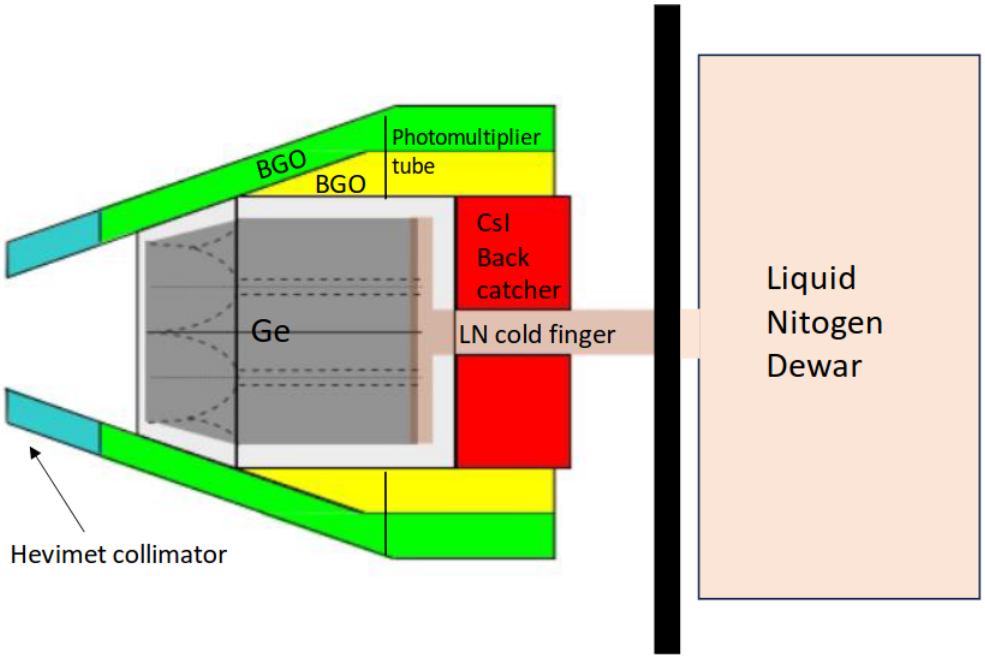

Figure 2.16: A schematic diagram of a Compton-suppressed detector, showing a Germanium crystal inside its BGO suppression shield and CsI back catcher. The shield suppresses the Compton scattered gamma rays that escape from the germanium and also acts as a collimation system, to prevent the scattering of gamma rays from a Ge detector to its neighbour.

encapsulation, a technique developed to enhance the reliability of composite detector technology [Ebe+92]. In an encapsulated detector, each crystal is enclosed in a sealed aluminum capsule with a wall thickness of 0.7 mm and fixed at a distance of 0.5 mm from the crystal's surface. This design ensures separation between the vacuum of the crystal and the cryostat vacuum.

- Segmented detectors: These detectors consist of a single germanium crystal, where the readout contact (typically the outer contact) has been divided into segments electrically. Recent studies have explored various segmentation geometries for segmented detectors. Examples include the 2-fold Gammasphere detector [DD88], the 6-fold encapsulated Miniball detector [Ebe+97], the 16-fold segmented Exogam Clover detector [Sim+00],

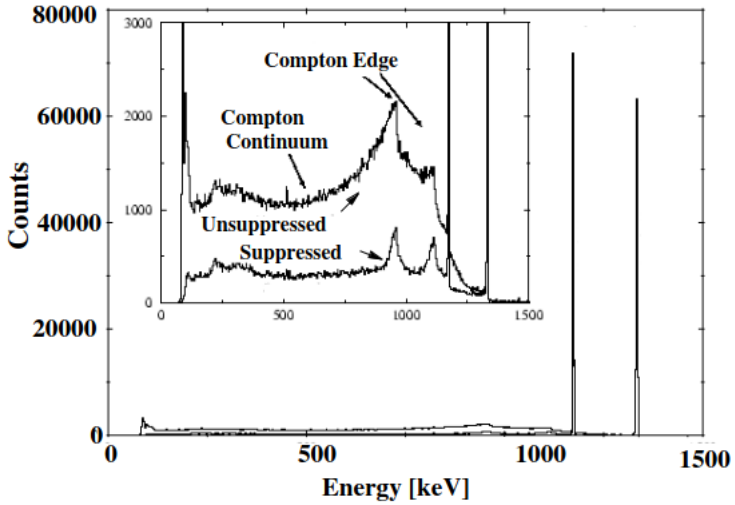

Figure 2.17: Un-suppressed and suppressed ^{60}Co spectra, measured with a n-type HPGe detector which has an efficiency of 25% (relative to a 76 mm x 76 mm sodium iodide (NaI) at 25 cm). In the insert, the y-axis has been re-scaled to show the detail of the background, while the full photopeak intensity relative to the background indicates the overall quality of the spectrum. [PJ 85]

the 25-fold MARS detector, and the main focus of this work [Baz+99], the 32-fold segmented ELIADE Clover detector.

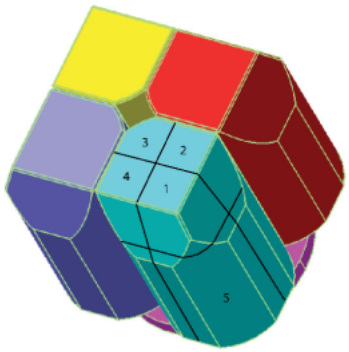

Figure 2.18: Schematic picture of the 32-fold segmented ELIADE clover detector. The peculiarity of this detector is, that it is both composite and segmented [Ur+16].

The depicted Figure 2.18 illustrates the geometry of the 32-fold segmented ELIADE clover detector, which serves as an example of a composite segmented detector. Multi-element detectors offer improved energy resolution performance, while maintaining high efficiency, due to their enhanced angular resolution and smaller opening angle. When combined with digital pulse shape analysis techniques, segmented detectors enable superior position resolution compared to the size of each individual segment.

Although segmentation technology is a relatively recent development in the field of nuclear instrumentation, it has been widely used in the construction of detectors for high-energy physics experiments. Silicon micro-strip detectors, for instance, have served as vertex detectors in colliding beam experiments for many years [Pei92b].
Composite and segmented detectors share several similar characteristics in various aspects.

Add-back performance

The efficiency of a composite detector surpasses that of a single-crystal detector with the same total volume. This enhanced efficiency stems from two primary factors that contribute to the overall efficiency of a composite detector.

The first factor is the direct detection efficiency, denoted as ϵ_D. This efficiency is determined by the photopeak efficiencies of each crystal when considered as a standalone detector. To measure the direct detection efficiency, the complete absorption of gamma-rays is recorded separately in each individual crystal. For a composite detector composed of n crystals, i is the number of crystals, the direct efficiency can be calculated using the following equation:

$$\epsilon_D = \sum_{i=1}^{n} \epsilon_{D,i}. \tag{2.30}$$

The second factor is the coincidence detection efficiency, also referred to as the add-back efficiency, denoted as ϵ_{AB}. This efficiency is determined by summing the energy deposited in the composite detector on an event-by-event basis. Coincidence events primarily occur due to Compton scattering of gamma-rays between two or more crystals. By summing the partial energy deposited in the individual crystals, the total energy of the gamma-ray can be recovered, thereby determining the coincidence detection efficiency.

In summary, the efficiency of a composite detector is higher than that of a single-crystal detector with the same total volume. The overall efficiency of a composite detector is a combination of the direct detection efficiency, which considers the photopeak efficiencies of individual crystals, and the coincidence detection efficiency, which accounts for the recovery of total gamma-ray energy through the summing of energy deposited in the composite detector.

Thus, the total detection efficiency can be expressed as:

$$\epsilon = \epsilon_D + \epsilon_{AB} \approx n\epsilon_{D,1} + \epsilon_{AB}, \tag{2.31}$$

assuming that the n crystals have equal efficiencies. The increase in efficiency achieved by combining coincidence signals is quantified by the add-back factor $F_{a,b}$, as given by:

$$F_{a,b} = 1 + \frac{\epsilon_{AB}}{\epsilon_D}. \tag{2.32}$$

However, it is important to note that coincidence events can also arise from multiple hits, where two different gamma rays simultaneously strike the detector. If the energies of these multiple hit events are combined in the spectrum, they contribute to the background signal. A segmented composite detector, such as the segmented ELIADE clover, offers an additional advantage. As depicted in Figure 2.19, a segmented clover detector allows for differentiation between multiple hit events and gamma ray Compton scattering events occurring between two adjacent crystals. This capability enables improved event discrimination and characterization in the detector.

Linear polarisation

In heavy-ion fusion evaporation reactions, the residual nuclei exhibit alignment of their spin vectors within a plane perpendicular to the beam axis. Consequently, gamma-ray transitions that de-excite the aligned nuclear state display an angular distribution anisotropy and linear polarization, which depend on the nuclear alignment and the de-excitation cascade. To determine the electromagnetic nature of a gamma-ray transition, the linear polarization of the photon can be measured using a Compton polarimeter.

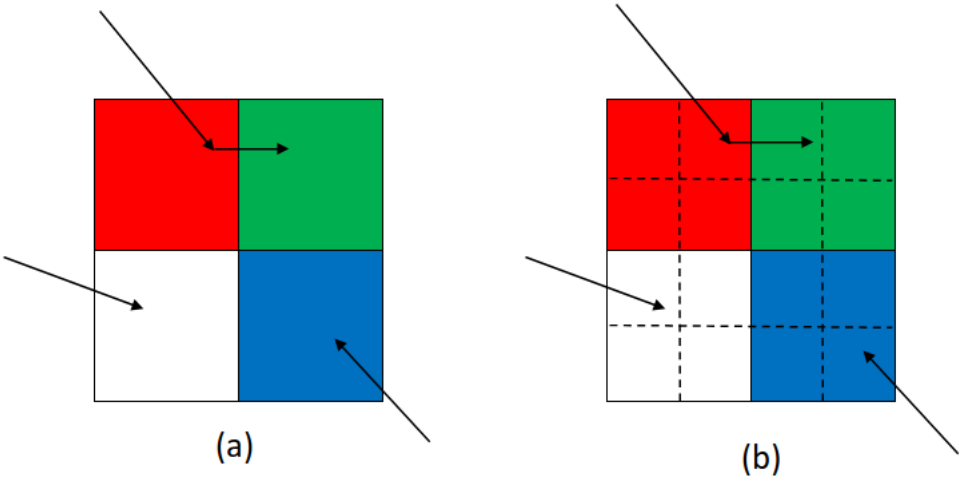

Figure 2.19: Schematic front face of original clover and segmented ELIADE clover. The segmented detector enables Compton scattered (a) and multiple hits events (b) to be distinguished. [She98]

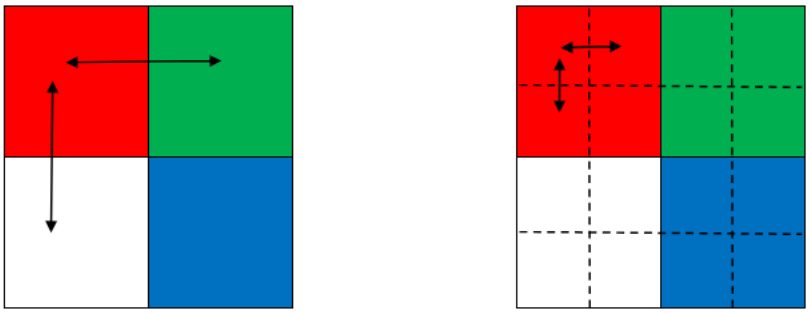

Figure 2.20: Advantages in using segmented detectors as a Compton polarimeter. [She98]

A Compton polarimeter enables the measurement of the scattering angle between the first and second interaction points of the gamma-ray within the detector. It has been observed that electric transitions tend to favor perpendicular Compton scattering, whereas magnetic transitions tend to favor parallel Compton scattering [Sch+94], [Sch+98]. A typical Compton polarimeter consists of three detectors: one scatterer and two absorbers, which can be either Ge crystals or scintillators.

Existing Compton polarimeters suffer from low efficiency due to multiple scattering and absorption within the scatterer detector. However, segmented germanium detectors can be employed as Compton polarimeters, as illustrated in Figure 2.20. These detectors offer advantages such as higher efficiency resulting from reduced dead material between the scatterer and analyzer, as well as improved energy resolution.

2.8 Summary

In this chapter, general principles of radiation detection are presented. As discussed in chapter 2.1, gamma-rays demonstrate three distinct interaction patterns based on their energy levels. For low-energy gamma rays (up to 200 keV), there is a higher probability of being absorbed through the photoelectric effect when interacting with dense materials. Gamma rays in the energy range of 200 to 2 MeV are more likely to engaged in Compton scattering for interaction, while gamma rays with energies exceeding 2 MeV have a greater chance to interact through pair production.

The Variable Energy Gamma rAy system in ELI-NP will have the energy range of 0 to 19.5 MeV, which means the test of ELIADE detector should cover the whole range ideally, especially in higher energies since the much more complicated interactions and detection requirements. Thus, another focus of this work is based on the higher energy Compton scattering and pair production, how the summing schemes and suppression schemes changes as the energy goes up.

Upon the interaction of a gamma ray with matter, both negative and positive charge carriers, i.e., electrons and holes, are liberated. These charge carriers then engage in Coulomb interactions with other electrons, leading to the formation of a charge cloud at the point of interaction. According to the Bethe-Bloch formula, the radiative losses are always a small fraction of the energy loses due to ionisation and excitation and are significant only in absorber materials of high atomic number.

The ELIADE array consists of 8 segmented HPGe clover detectors, germanium have

the best energy resolution compared with other semiconductors as a consequence of the small ionisation energy, leading to the largest charge carrier number. Semiconductors function as diodes using a P-N junction, a configuration involving the combination of two materials, one being p-type and the other n-type. By applying a reversed bias, a depletion region, sensitive to incoming radiation, is formed. By using the segmentation, the interaction point of the gamma rays with the detector can be found and used in the analysis.

Semiconductors are employed in conjunction with charge-sensitive preamplifiers featuring resistive feedback, aimed at minimising capacitive noise. The preamplifier pulse is channelled through the resistive feedback circuit, where the pulse amplitude is directly linked to the energy of the incoming gamma ray.

In nuclear instrumentation, the effectiveness of a detector is evaluated based on three key metrics: energy resolution, peak-to-total ratio, and efficiency. Variability in energy resolution arises from the statistical characteristics of the radiation, electronic noise, and incomplete charge collection. Efficiency, either in absolute or intrinsic terms, is computed by dividing the detected interactions by the emitted or incident radiation, respectively.

In the next chapter, details of the VEGA system and ELIADE detection system will be presented. This is crucial because comprehending how the system operates is essential for precise simulation and prediction of its performance.

Chapter 3

VEGA system

ELI-NP aims to establishing a prominent installation, known as the High-Power Laser System (HPLS), to serve the global scientific community. The HPLS will comprise two separate laser arm segments, each capable of delivering a maximum power of 10 PW (10^{16} W). Additionally, a high-brilliance and high-intensity γ beamline, named the Variable Energy Gamma rAy (VEGA) system, will be incorporated. The VEGA system will leverage the Compton backscattering process to generate gamma rays of varying energies.

The layout of the whole experimental area at ELI-NP is depicted in Figure 3.1. The VEGA system operates independently from the HPLS, with the exception of target area E7. In this specific area, high-power laser pulses and high-intensity gamma flashes, reaching energies of up to 19.5 MeV and exhibiting a remarkably high linear polarization of over 95%, can be combined to facilitate nuclear experiments. ELIADE array is placed in E8 area. Additional target areas, including E3, E8, and the newly installed E9 (neutron experiments area) annex, are also depicted in Figure 3.1.

The Variable Energy Gamma rAy(VEGA) System is a dedicated system for delivering gamma-ray beams to users, is currently being implemented at ELI-NP. This newly developed VEGA ray system will be utilised for investigating significant nuclear reactions relevant to nucleosynthesis. One such reaction is the fusion of α particles and carbon nuclei, resulting in the production of oxygen ($^4He + ^{12}C \rightarrow ^{16}O$), which plays a fundamental role in supporting life on Earth.

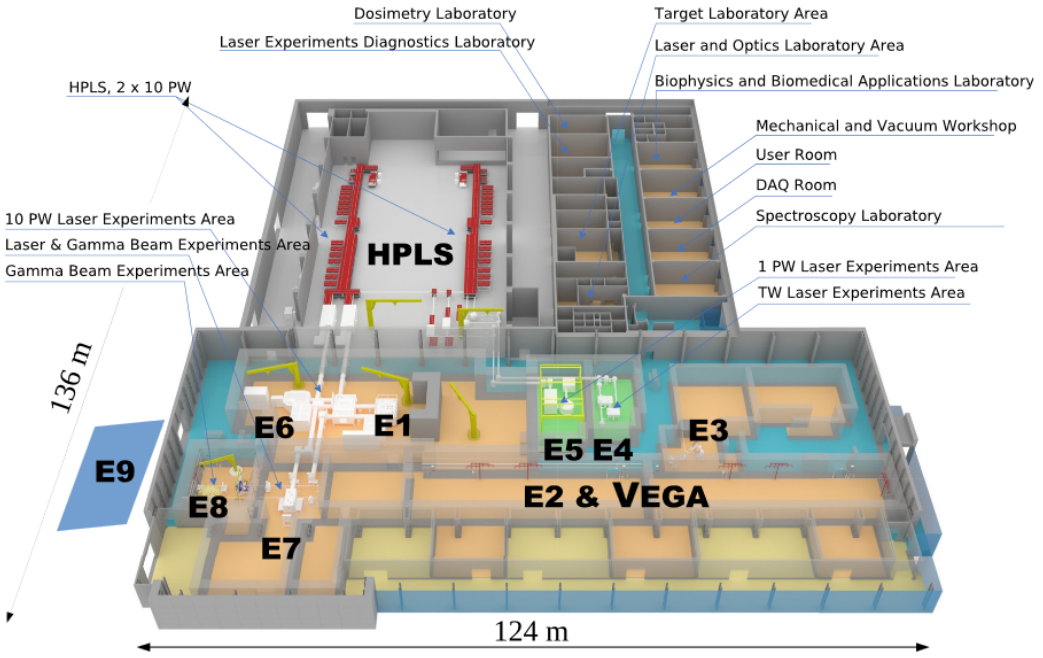

Figure 3.1: Schematic overview of the HPLS and the VEGA system and associated target areas at ELI-NP. The two laser arms are depicted in red. The target areas E1, E4, E5, E6, and E7 show the 3D CAD designs of the target chambers currently under construction. The positions of the target areas E3, E8, and E9 associated with the VEGA system are indicated. The E9 area sits in the newly installed annex sketched by the blue footprint adjacent to the left side of the main building. The target area E2 will be facilitated for VEGA system related experiments in the future. [from ELI-NP]

Moreover, the VEGA system will enable high-resolution measurements of Nuclear Resonance Fluorescence (NRF). This intense and tunable beam of gamma radiation, with energies reaching up to $E_\gamma = 19.5$ MeV, allows for precise NRF measurements. These NRF-based techniques have the potential for various applications, including imaging and gamma tomography, which can significantly contribute to the field of nuclear security.

In this chapter, the general principle of high intensity gamma sources, bremsstrahlung and laser Compton-backscattered photon NRF will be discussed, along with the status of the VEGA system, this will help to understand the experiments using the VEGA system and

ELIADE array in the future.

3.1 Photon sources and instrumentation

Gamma rays are a form of electromagnetic radiation characterised by an energy threshold of 100 keV. Their discovery can be attributed to Paul Villard in 1900 during his investigations of radium radiation. Subsequently, Ernest Rutherford coined the term "gamma ray" to describe this type of radiation. Gamma rays quickly gained significant attention and interest due to their remarkable ability to penetrate matter deeply. Researchers have detected abundant gamma rays in various cosmic phenomena, including terrestrial thunderstorms, solar flares, cosmic rays, pulsars, and gamma-ray bursts. On Earth, natural sources of gamma rays primarily arise from radioactive decay processes. To harness their potential, numerous artificial methods have been developed, leading to significant advancements in improving the properties of gamma-ray sources.

Gamma-ray sources have found widespread applications in various fields, including medical treatments [C+16], industrial measurements [D+16], and scientific research [CZS16]. They are utilised for tasks such as radiographic imaging of objects [Gli+05] [Ben+11] [Cor+13] [AJ01], exploring nuclear physics [NVZ14], laboratory astrophysics, and high energy density physics [Yu+19]. Notably, there is a mention of the gamma-gamma collider, which is considered a potential means to create a Higgs factory. To fulfill the diverse requirements of these applications, the development of gamma-ray sources is currently focused on achieving high energy, short pulse durations, small energy resolutions, and high brightness. These advancements aim to generate versatile gamma-ray sources capable of meeting the demands of different fields and applications.

In 1969, F.R. Metzger firstly played a pioneering role in utilising Van de Graaff accelerators to generate stable and intense beams of electrons with adjustable energies for studying nuclei through bremsstrahlung [FRM69]. This approach enabled the acquisition of photon scattering data with enhanced sensitivity and quality. Subsequently, advancements were made with the introduction of dedicated high-current electron linear accelerators capable of producing bremsstrahlung photons and the utilisation of Ge semiconductor detectors, known for their excellent energy resolution, to detect the scattered photons

[Wie+81] [Mor+82] [Gov+94]. Numerous photonuclear experiments were conducted using the high-current continuous-wave electron beams of the Stuttgart Dynamitron [Kne90] and the superconducting electron linear accelerator, also known as the 'S-DALINAC', at the Technische Universität Darmstadt [Ric95].

Bremsstrahlung facilities generate a continuous spectrum of photons, with the intensity increasing rapidly at lower energies. While this broad energy range is suitable for many purposes, there are specific tasks that benefit from using energy-tunable (quasi-)monochromatic photon beams in the MeV range. These applications include detailed spectroscopy or targeted manipulation of specific nuclear excitations. Compared to bremsstrahlung sources, which produce a significant amount of low-energy background radiation, the use of quasi-monoenergetic photon beams with variable energy can be advantageous. Efforts have been made to develop such quasi-monoenergetic photon sources. In 1953, Colgate and Gilbert published pioneering experiments demonstrating the production of photons through positron annihilation in flight [CG53]. Subsequently, this method was employed at various facilities, such as those in Saclay [Vey+79], Livermore [Ful+62], and Giessen [Kne+75], to investigate the photoresponse of atomic nuclei.

An alternative method to achieve (quasi-)monochromatic excitation of nuclei is through the use of tagged photons. This involves the generation of thin-target bremsstrahlung photons while simultaneously detecting the corresponding decelerated electrons. Notably, research conducted at the photon tagger facility at the Illinois electron accelerator facility has made significant contributions to the study of the dipole response of nuclei below the neutron binding energies across a wide range of masses [OCo61] [OCo+62] [Kno+82]. This research has yielded valuable insights, as evidenced by references [Axe+63] [Las86] [Las+87] [Las+88].
A significant advancement in generating MeV photons was achieved through the concept and practical implementation of Laser Compton Backscattering (LCB) [Mil63] [AT63]. This approach enables the production of photon beams with unprecedented intensities that are both quasi-monoenergetic and fully polarised.

In the following sections, bremsstrahlung, tagged photon techniques and laser Compton backscattering will be discussed in details.

3.2 Bremsstrahlung

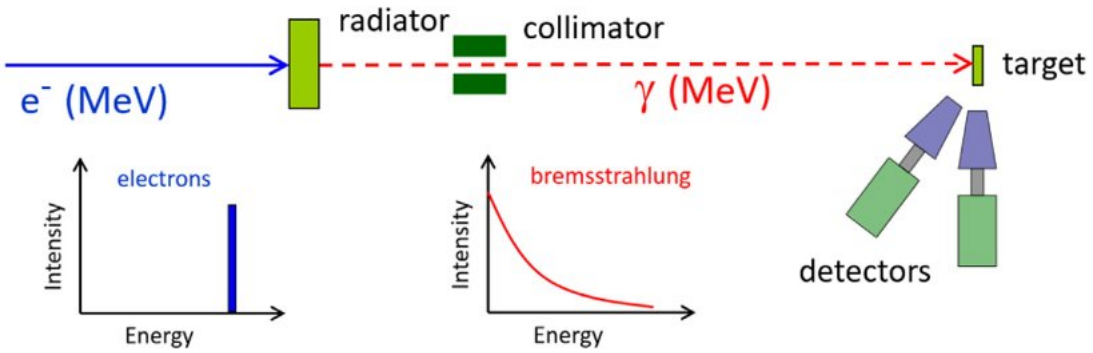

Figure 3.2: Principle of generating a photon beam by bremsstrahlung. Figure from [Zil+22]

An effective method for generating a highly intense photon field with a continuous energy distribution is through electron bremsstrahlung. The basic principle is illustrated in Figure 3.2. An electron beam is decelerated or, depending on the thickness of the radiator, completely stopped in a radiator target. The photon flux, integrated over energy and angle, scales quadratically with the charge Z of the nuclei in the radiator target. When considering only a single interaction, the bremsstrahlung spectrum produced by a thin radiator target can be approximated using Schiff's analytical formula [Sch51]. Schiff employed the symbols E_0 for the energy of the incident electron, E for the energy of the scattered electron, k for the energy of the emitted photon, μ for the rest energy of the electron, θ for the angle between the photon and electron, Z for the atomic number of the radiator target, and the screening constant C = 111. This approximation holds when E_0, E, and k are significantly larger than μ. By replacing θ with the reduced angle x = $E_0\theta$ /μ, the cross-section for the energy-angle distribution can be derived:

$$\sigma(k,x)dkdx = \frac{4Z^2}{137}\left(\frac{e^2}{mc^2}\right)\frac{dk}{k}xdx\left[\frac{16x^2E}{(x^2+1)^4E_0} - \frac{(E_0+E)^2}{(x^2+1)^2E_0^2} + \left(\frac{E_0^2+E^2}{(x+1)^2E_0^2} - \frac{4x^2E}{(x^2+1)^4E_0}\right)\ln(M(x))\right] \tag{3.1}$$

$$\frac{1}{M(x)} = \left(\frac{\mu k}{2E_0E}\right)^2 + \left(\frac{Z^{1/3}}{C(x^2+1)}\right)^2. \tag{3.2}$$

To derive the energy spectrum, the equation mentioned above needs to be integrated over x. It is important to note that this calculation is not applicable for large angles; however, the majority of the radiation is concentrated in forward angles:

$$dk \int_0^\infty \sigma(k,x)dx = \frac{2Z^2}{137}\left(\frac{e^2}{mc^2}\right)^2 \frac{dk}{k}\left[\left(\frac{E_0^2+E^2}{E_0^2} - \frac{2E}{3E_0}\right) \times \left(\ln(M(0)) + 1 - \frac{2}{b}\tan^{-1}(b)\right) + \frac{E}{E_0}\left(\frac{2}{b^2}\ln\left(1+b^2\right) + \frac{4(2-b^2)}{3b^3}\tan^{-1}(b) - \frac{8}{3b^2} + \frac{9}{2}\right)\right]. \tag{3.3}$$

An additional parameter, b, can be defined as b = $(2E_0\mathrm{E}Z^{1/3}/\mathrm{C}\mu\mathrm{k})$ in the context of the Schiff formula. Later on, more advanced versions of the Schiff formula have been published in subsequent works, as referenced in [Roc+72] [DB91] [Hau08].

Since 1990s, the energy spectrum of bremsstrahlung photons is commonly determined using various Monte Carlo simulation codes [Lin+91] [Sch+05] [Kos+10]. One of the primary challenges in these calculations is accurately extracting the bremsstrahlung flux near the endpoint energy of the spectrum. This task heavily relies on the energy of the electron beam and its fluctuations. Consequently, precise monitoring of the electron beam energy is crucial for many experiments.

The outer region of the bremsstrahlung cone emitted from a thin radiator (with a thickness less than 10^{-3} radiation lengths) exhibits partial polarization [MW51]. The optimal degree of polarization, achieved with an electron beam energy E_e, can be obtained at an off-axis angle $\theta = m_e c^2/E_e$. However, as the energy of the bremsstrahlung photons increases, the degree of polarization decreases, typically reaching a maximum value of only 10% to 20% [Gov+94] [Sch+07]. Furthermore, using a thin radiator results in a lower intensity of photons compared to a thicker radiator with a similar electron current [BK87a]. Nonetheless, this technique has been employed in several seminal experiments to determine the parity quantum number of excited states in nuclei.

3.3 Tagged photon techniques

Photon tagging is a method employed to generate quasi-monochromatic photons by detecting a secondary product resulting from the process in which the photon originated. Figure 3.3 shows the principle of photon tagging. The device used to detect this secondary product is known as the tagging detector. By measuring the energy or angle of the secondary product in the tagging detector, the energy of an individual photon can be determined. If the secondary product is coincident with a product stemming from the target that intercepts the photon flux, it can be inferred, after discounting random coincidences, that the reaction product was produced by the original single photon.

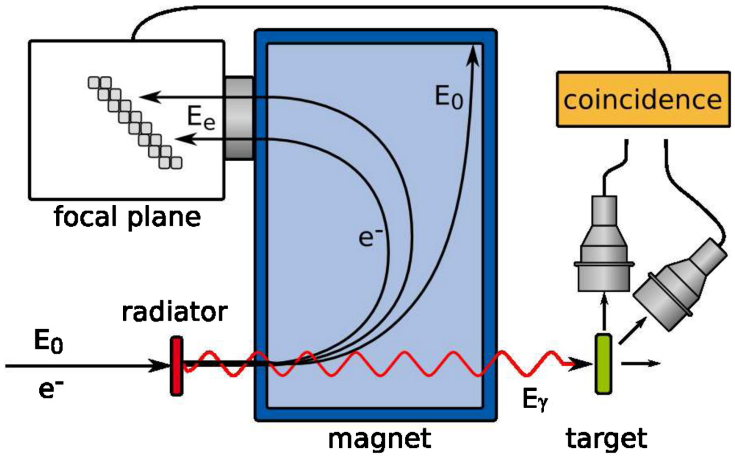

Figure 3.3: Principle of photon tagging. The energy of the produced bremsstrahlung photon E_γ is determined from the energy difference between the incident and the scattered electron energy E_0 and E_e, respectively. Figure from [Zil+22]

By counting the number of events in the tagging detector, it becomes possible to determine the corresponding number of incident photons on the target. However, it should be noted that not all photons produced may actually reach the target due to the collimation of the photon beam. Therefore, it is crucial to accurately determine the probability that an event detected in the tagging detector is associated with a photon that has reached the target. This knowledge enables the determination of the magnitude of the incident photon flux. This factor is known as the tagging efficiency, and it is desirable for the tagging efficiency

to be as close to 100% as possible.

In the majority of cases, the tagging efficiency of a system can be determined through measurement. One common approach involves placing a photon detector with a known efficiency directly in the photon beam. By recording the count rates in the tagging detector, photon detector, and the coincidence rate between the two, the efficiency can be evaluated. Additionally, measurements are conducted in the absence of the photon beam to account for background rates. This comprehensive approach provides a reliable measure of the tagging efficiency.

The tagging efficiency can be determined using the following equation:

$$E = \frac{I_m}{L_m - (t_m/t_b)L_b}. \tag{3.4}$$

In this equation, I_m represents the rate of coincidences between the photon detector and the tagging detector. L_m and L_b denote the rates of the tagging detector for the measurement and background, t_m and t_b represent the live time for the measurement and background data, respectively.

The effective flux of the tagged photon beam generated is limited by the occurrence of random coincidences and the allowable counting rate of the tagging detector. There are two main sources of random coincidences. Firstly, there are coincidences where two events are detected within the system's coincidence resolving time. These events need to be disregarded as they introduce uncertainty in the photon energy measurement. Secondly, there are coincidences where the particle detector event is triggered by a photon that falls outside the energy range covered by the tagging detector. As a result, these coincidences produce erroneous photon energy values. In some cases, it may be possible to identify and reject such events based on kinematic considerations.

The evaluation of a tagging system's performance can be based on several key factors, including the magnitude of the tagged photon flux, the tagging efficiency, and the relative rates of real to random coincidences. Achieving optimal values for these quantities is a crucial objective in the design of a tagging facility, as it determines the overall effectiveness and utility of the system. [WM53] [CM61] [JA62]

Recently, three primary tagging techniques have been used [BB80] [Car83]:

- Laser backscattering
- In-flight positron annihilation
- Tagged bremsstrahlung

3.4 Laser Compton backscattering

The fundamental principle of this method is relativistic Compton scattering. It involves the interaction of a photon, initially produced by a low-energy laser, with a high-energy electron beam. When a laser beam is directed at a shallow angle onto an ultra-relativistic electron beam, photons that emerge in the same direction as the electron beam undergo backscattering, as shown in Figure 3.4.

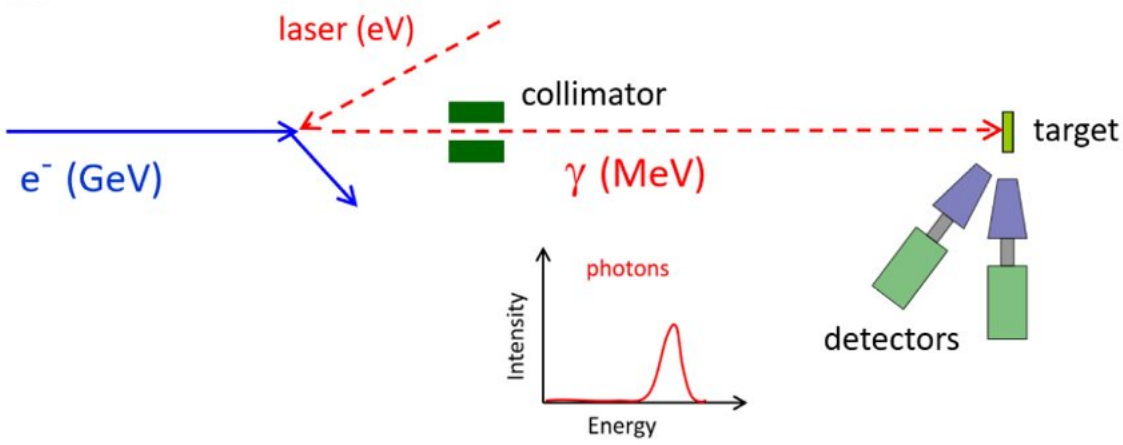

Figure 3.4: Principle of generating a photon beam by laser Compton backscattering. Figure from [Zil+22]

To ensure that only the high-energy backscattered photons reach the photonuclear target, both the residual electron beam and the Compton electrons are magnetically deflected

away from the beam path. This deflection separates them from the path of the desired backscattered photons.

The Compton electrons are subjected to momentum analysis. An approximate calculation for the energy of a backscattered photon, E_γ, can be obtained using the equation:

$$E_\gamma = \frac{4\gamma^2 E_L}{\frac{4\gamma E_L}{m_e c^2} + \theta^2\gamma^2 + 1}, \tag{3.5}$$

where θ represents the angle at which the photon emerges relative to the direction of the electron, E_L denotes the energy of the laser beam, and γ is defined by the equation:

$$\gamma = \frac{E_0}{m_e c^2}, \tag{3.6}$$

where E_0 is the primary electron beam energy, c denotes the speed of light, and m_e represents the rest mass of the electron. The expression in Eq 3.5 is only valid for small angles. Upon examining these equations, it becomes apparent that E_0 must be exceedingly large in order to generate photons in the intermediate energy range. In fact, an electron beam of several GeV is required for this purpose.

The equation also suggests that achieving good energy resolution is feasible by minimising the angular acceptance, $\delta\theta$, through collimation of the photon beam. Additionally, ensuring a small energy and angular spread in the electron beam can contribute to improved energy resolution. However, it's important to note that these measures to enhance the energy resolution can result in a reduction of the tagged photon flux.

Alternatively, the energy information can be derived from the energy of the scattered electron, $E^{'}$, using the equation:

$$E_\gamma = E_0 - E'. \tag{3.7}$$

This method offers a moderate level of photon energy resolution but yields larger tagged fluxes compared to the previous approach. The magnitude of the tagged flux is influenced by factors such as the electron beam current, the laser power, and the required degree of collimation.

Tagged photon beams generated through this method have faced a significant drawback thus far: limited tagged photon fluxes. Nonetheless, the laser backscattering technique offers a significant advantage in that a polarised laser beam can be used as the initial photon source. As the polarization is preserved during the scattering process, practical applications can achieve a linear polarization ranging from 75% to 100%.

Laser Compton scattering is the only practical method for producing energy-tunable and quasi-monoenergetic photon beams in the MeV energy range. Compton sources utilising electron storage rings have been developed to supply MeV photons for various applications. Two notable user facilities that offer MeV photons are NewSUBARU at Hyogo University and HIGS at Duke University. At NewSUBARU, laser pulses from an external laser are introduced into an electron storage ring, with the laser operating in continuous wave (CW) or Q-switched mode at kilohertz repetition rates [Ama+09]. On the other hand, HIGS employs a free-electron laser for laser Compton scattering [Wel+09].

MeV-energy photons offer valuable opportunities for studying nuclear physics, as they engage in electromagnetic interactions with atomic nuclei. Detecting photo-nuclear reactions, such as (γ, n) and (γ, γ'), is a common method for exploring nuclear structure and dynamics. These reactions also have potential applications in industries. One promising application is the non-destructive detection and measurement of fissile material using NRF, as highlighted by Hajima et al [Haj+08].

3.5 VEGA facilities at ELI-NP

At ELI-NP, The Variable Energy Gamma rAy (VEGA) System, a Compton backscattering based gamma beam source is currently being constructed to generate MeV photons with higher spectral density compared to those produced by storage rings. The gamma source at ELI-NP will produce Compton photons with tunable energy ranging from 1 to 19.5 MeV. These photons will possess a very narrow bandwidth less than 0.5% and exhibit a high spectral density of 10^4 (photons/s/eV).

Over the past few decades, there has been continuous progress in the development of gamma-photon beams with optimised properties for both research and practical appli-

cations. Table 3.1 illustrates the categorization of photon sources into five generations, representing the past and potential future advancements [Zil+22]. The first generation of photon sources relied on artificially induced γ-radioactivity from various excited nuclei, but lacked energy-tunability. In the second generation, MeV-range photon sources emerged, offering either broad-band bremsstrahlung or low-intensity beams with limited energy resolution or energy-tagging capabilities. These sources have significantly contributed to the field of photonuclear science, as discussed earlier. Presently, the most advanced photon sources utilise the principle of laser Compton backscattering on electrons in synchrotrons or storage rings. The HIγS facility has exemplified notable productivity in this regard [Wel+09].

Generation	**Photon sources**
1st	radioactive atoms, (x, γ) reactions
2nd	bremsstrahlung, e^+ annihilation
3rd	Laser Compton Backscattering
4th	LCB with superconducting ERL, multi-bunch/multi-pulse LCB
5th	Gamma factory (partially stripped ions)

Table 3.1: Past and possible future generation of photon sources. Adapted from [Zil+22]

Several new Laser Compton Backscattering (LCB) facilities with enhanced parameters compared to existing ones are set to become operational in the coming years. An example of such a facility is the Variable Energy Gamma rAy System (VEGA) being constructed at the Extreme Light Infrastructure-Nuclear Physics (ELI-NP) international research center in Magurele, Romania. VEGA, developed by Lyncean Technologies, utilises a warm electron linac with a maximum energy of 750 MeV as an injector for a high-frequency storage ring, as depicted in Figure 3.5. The storage ring will operate in the top-off mode, ensuring continuous injection of electrons to maintain a nearly constant current. The collision frequency between electrons and laser photons will be approximately 35 MHz. This continuous wave (cw) beam minimises dead time losses in detectors commonly used with nanosecond-level time resolutions. VEGA employs two types of lasers, one in the infrared (IR) and the other in the green wavelength range. By selecting one of these lasers and tuning the energy of the electrons in the storage ring accordingly, the generated photon beams can be continuously varied between 1 and 19.5 MeV. The small emittance of the electron beam leads to a narrow bandwidth of approximately 0.5% or even less for the Compton

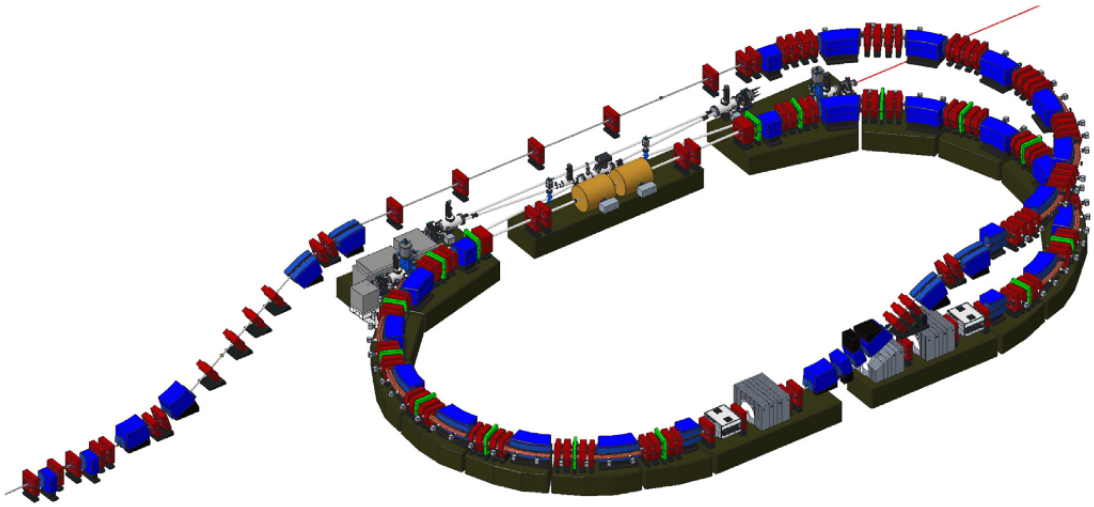

Figure 3.5: The VEGA laser Compton backscattering facility planned at ELI-NP.
Source: Figure courtesy of Lyncean Technologies, Fremont, USA.

backscattered laser photons. The total photon flux is expected to exceed 10^{11} photons per second, and the collimated, time-averaged spectral intensity at the peak position will be greater than 5×10^3photons/s/eV. Initially, the delivery, installation and acceptance of VEGA were scheduled to be completed in early 2023, however, it is now postponed for further discussions due to unexpected delays.

The VEGA system at ELI-NP is poised to become a state-of-the-art facility that surpasses current technology in delivering gamma beams with significantly improved photon spectral densities and bandwidths. Extensive preparations are underway for a versatile experimental research program utilising the VEGA system. These experiments will explore various aspects of photonuclear physics, capitalizing on the exceptional performance characteristics of the VEGA system, including its narrow beam bandwidth, high brilliance, and high degree of polarization. Recent works have provided comprehensive reviews of different aspects of the research program related to gamma beams [Gal+18] [Bal+17] [Fil+15].

3.6 General principle of photon scattering NRF

Nuclear Resonance Fluorescence (NRF) is a phenomenon in which a nucleus absorbs and emits high-energy photons called gamma rays. These emitted photons are commonly referred to as NRF gamma-rays. In material analysis applications, NRF is typically induced by stimulating nuclear states using a photon beam. The subsequent NRF gamma-rays are then detected using photon detectors like high-purity germanium (HPGe) or scintillation detectors. As NRF states correspond to excited nuclear levels, the absorption of photons and the energies of the resulting NRF gamma-rays can be used to identify the specific nucleus undergoing NRF. This identification process is analogous to passive gamma-ray spectroscopy employed in the identification of decaying radioactive nuclides.

Once the array geometry and the cross-section for NRF are known, it is possible to determine the number of atoms of the corresponding isotope by measuring the rate at which NRF takes place. The rate at which a specific nuclide undergoes NRF in thin targets can be described by:

$$R = \int N\Phi(E)\sigma(E)dE. \tag{3.8}$$

Where N is the number density of atoms in the target that undergo NRF with cross section, $\sigma(E)$. When using thicker targets, it becomes necessary to account for geometrical corrections because the energy-dependent photon flux, $\Phi(E)$, can vary as it passes through the target.

The cross section, σ, for photo-excitation of a nuclear state is given by the Breit-Wigner distribution:

$$\sigma(E) = \pi\gamma(\delta,\delta_0)\frac{(\hbar c)^2}{E^2}\frac{\Gamma\Gamma_0}{(E-E_c)^2+(\Gamma/2)^2}. \tag{3.9}$$

Where Γ is the full-width at half maximum (FWHM) of the state and is related to the state's mean lifetime, τ, by:

$$\Gamma = \frac{\hbar}{\tau}. \tag{3.10}$$

Γ_0, Γ_f, Γ are the decay widths to the ground state, the final level and the total decay width. E_c denotes the centroid energy of the resonance, while $\gamma(\delta,\delta_0)$ is a statistical factor that signifies the ratio between the number of available spin states for the excitation and the number of initial spin states. In the case of NRF events where the initial nuclear state is

the ground state, these parameters play a crucial role:

$$\gamma(\delta, \delta_0) = \frac{2J+1}{2J_0+1}. \tag{3.11}$$

Where J and J_0 are the angular momentum quantum numbers of the excited and ground states, respectively [Kne+96].

The probability of a state undergoing de-excitation through a specific mode, such as neutron emission or gamma-ray emission, resulting in a lower-energy state, can be described by the state's partial width for that particular mode:

$$p_i = \frac{\Gamma_i}{\sum_j \Gamma_j} = \frac{\Gamma_i}{\Gamma}, \tag{3.12}$$

where we have used:

$$\Gamma = \sum_j \Gamma_j. \tag{3.13}$$

By considering the summation over all possible de-excitation modes, the cross section for Nuclear Resonance Fluorescence (NRF) to occur through the emission of a single gamma-ray, leading to the ground state, can be derived by combining Eq 3.9 and Eq 3.12 as follows:

$$\sigma_{GS}(E) = \frac{\Gamma_0}{\Gamma}\sigma(E) = \pi\gamma(\delta, \delta_0)\frac{(\hbar c)^2}{E^2}\frac{\Gamma_0^2}{(E-E_c)^2 + (\Gamma/2)^2}. \tag{3.14}$$

In the rest-frame of the nucleus, photon wave functions in its vicinity decrease in magnitude as the angular momentum increases. As a result, the probability of interaction with the nucleus decreases accordingly with increasing angular momentum. In photonuclear interactions, the preference is for the lowest possible angular momentum transfer to occur [BW52].

3.7 Experiments using VEGA system

An extensive and diverse research program is being developed for the VEGA system, aiming to leverage its unique performance characteristics, including narrow bandwidth, high brilliance, and high degree of polarization. The experimental focus will be on various

aspects of photonuclear physics, such as nuclear resonance fluorescence (NRF), photonuclear reactions, studies of nuclear resonances, and photo-fission research. Recent works have extensively reviewed different aspects of the γ-beam-related research program [Gal+18] [Bal+17] [Fil+15].
Notably, NRF experiments will benefit from pencil-like, narrow-bandwidth, and highly polarised γ ray beams with a spectral photon density of approximately $10^4 s^{-1} eV^{-1}$. This feature enables higher sensitivity and improved yield in NRF studies, while reducing the mass of targets required. For instance, using only a few hundred milligrams of material will be possible at ELI-NP, making it feasible to study less abundant isotopes like p-process nuclei or actinides. Notably, the actinide region has been relatively underexplored in terms of NRF studies, with only a few cases studied, such as ^{232}Th or $^{236,238}U$ [KZ12]. The VEGA system at ELI-NP offers promising opportunities for novel and groundbreaking research in this area.

To perform the studies, the ELI-NP Array of Germanium Detectors (ELIADE) is currently being constructed at ELI-NP. It comprises eight TIGRESS-type HPGe clover detectors [Scr+05], arranged in two rings, with two detectors in the vertical and two in the horizontal plane. Each clover detector is composed of four encapsulated n-type HPGe crystals, made from a 60 mm diameter and 90 mm long crystal. The outer surface of each crystal is tapered over 30 mm to allow for close packing. Each crystal is further divided into four quadrants and two lateral sections using an outer boron-implanted contact, resulting in 36 signals per detector and a total of 288 electronic channels for the HPGe array.

To suppress background noise for high-energy γ-ray measurements, bismuth germanate (BGO) scintillators will be mounted as back plugs. Additionally, large LaBr3 (Ce) detectors can be positioned at 45° relative to the HPGe clover detectors, enhancing the overall efficiency of the array. The ELIADE array, shown in Figure 3.6, will have an absolute gamma-ray efficiency of approximately 6%. It will enable coincidence measurements and serve as an excellent gamma-ray polarimeter, allowing for studies of gamma-ray angular correlations. The completion of the ELIADE array will provide valuable capabilities for various research activities involving gamma-ray detection and analysis.

One of the commissioning experiments planned for ELIADE involves the photoactivation measurement of ^{180}Ta [Gal+18]. This measurement is an important component of

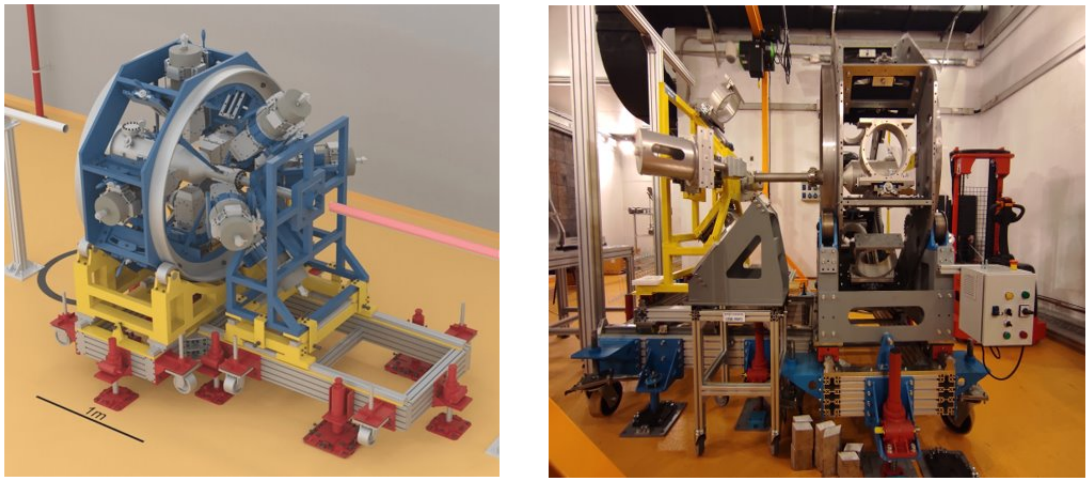

Figure 3.6: A 3D CAD view of ELIADE array with the HPGe detectors in (a) and a photo of the frame in (b). ELI-NP

the ELIADE research program, which focuses on high-resolution studies of various nuclear modes, including E1, M1, and E2 modes, in the region below the neutron evaporation threshold of nuclei. The unique capabilities of ELIADE's gamma-ray efficiency will allow for distinguishing and separating different excitations in the overlapping region of the pygmy dipole resonance (PDR) [DZ13], giant dipole resonance (GDR), magnetic dipole resonance (MDR), and pygmy quadrupole resonance (PQR) [TL11].

The high-resolution experiments enabled by ELIADE will provide detailed insights into the γ-ray decay of such excitations, including their decay to the ground state and to excited states. These investigations are crucial for informing theoretical models aimed at describing pygmy resonances in atomic nuclei. Additionally, these experiments will be highly sensitive to weak branches of different excitation modes. For instance, the measurement of electric dipole polarizability (α_D) is particularly sensitive to the low-lying E1 strength and is correlated to the neutron skin thickness in a robust and less model-dependent manner. Theoretical models have established connections between the slope of the symmetry term of the nuclear equation of state (EoS) and the neutron skin thickness. The polarizability

α_D is related to the photoabsorption cross-section σ_{abs} by:

$$\alpha_D = \frac{\hbar c}{2\pi^2} \int_0^\infty \frac{\sigma_{abs}(E)}{E^2} dE, \tag{3.15}$$

here E is the excitation energy and σ_{abs} is the absorption cross section. Note that σ_D is strongly depending on the E1 strength at low energies. For the stable nucleus ^{208}Pb, the neutron skin thickness was extracted from the measured α_D. These studies are expected to contribute significantly to our understanding of nuclear properties and enhance our knowledge of atomic nuclei's behavior [Tan+20].

Other detector systems related to VEGA include: experiments above the particle evaporation threshold (ELIGANT), for protons and α particles (ELISSA, ELITPC), for fission fragments (ELI-BIC, ELITHGEM) and for E and t spectra of annihilation gamma rays, e^+ lifetimes, Doppler shift, Auger electrons (ELIPS).

In summary, the VEGA system at ELI-NP offers the opportunity to study a variety of photonuclear reactions with scientific significance. These reactions include activation and (γ,γ') reactions, which can occur below and above the neutron evaporation threshold. Additionally, investigations into photodisintegration reactions and photofission are possible, along with the study of nuclear excitation modes to gain deeper insights into PDR and GDR. The diverse physics program covers a wide range of topics that are of general interest to the entire scientific community.

Chapter 4

Test of the prototype ELIADE detector and active shields

To validate the performance of the HPGe detectors and also begin the development of methodology that will be required during the ELIADE experiments, a number of tests have been conducted. The efficiency and resolution tests were done with Clover29 (CL29) which is without Compton suppression. However, the tests with Anti-Compton shield is only performed with Clover33 (CL33) due to the limited sets of Compton-suppression shields, and unfortunately Clover33 has only three crystals working during the measurements. **Therefore, all the simulations in comparison with Clover33 in this work, only 3 crystals are activated to compromise the experiments.**

This chapter will detail the tests conducted on the prototype of ELIADE detector and the Compton-suppression shields to evaluate their combined performance. The tests aimed to determine the relative efficiency curves and peak-to-total ratios for several well-known radioactive sources. Furthermore, the tests also obtained the energy resolution functions for the HPGe detector.

In this work, the general peak-to-total ratio (P/T) is defined as:

$$P/T = \frac{N_P}{N_T}. \tag{4.1}$$

Where N_P is the number of photopeak counts observed (full-energy gamma-ray depositions), for two or more photopeaks, the counts will be added from all peaks. N_T is the total number of counts in the spectrum, ranging from the thresholds to the photopeak to cover all the Compton backgrounds. The number of counts can be found by integral functions, a subtraction of noise signal from the total number of counts is applied by setting the thresholds (around 150 keV for ^{60}Co and 50 keV for ^{137}Cs and ^{22}Na) when taking measurements. In simulation, the thresholds were set to be the same for comparison.

For higher energy analysis, due to the small statistics in photon peak, a selection of energy region instead of the total number of counts in the spectrum will be applied.

A function that represents the detection efficiency of a detector's photopeak relative to the energy of gamma-rays is called a relative efficiency function. This function is established by comparing the counts of gamma-ray photopeaks within a particular energy range to their known relative intensities. Meanwhile, an energy resolution function reveals the width of the measured photopeaks relative to the energy of the gamma-rays.

The measurements were carried out for two purposes. First, to determine the sensitivity of HPGe detectors, which provides a basis for comparing ELIADE with other HPGe detectors and setting experimental guidelines that depend on the expected sensitivity of the array. Second, obtaining peak-to-total ratios and relative efficiencies and comparing them with results of an ELIADE GEANT4 simulation establishes a benchmark for the accuracy of the simulation. Additionally, the energy resolution functions allow for a comparison of the simulated and experimental spectra for the same reason.

4.1 Apparatus

To replicate experimental conditions, a testing apparatus was first created to mount a single ELIADE detector(CL33) at the VEGA system height, the highest position in the first ring was chosen since that's the easiest point to mount the suppression shield in place. A source holder was designed and 3D printed. It has two parts and was designed to allow small radioactive sources to be placed at distances up to 24 cm from the detector surface, every

1.5 cm as a step. These will be the largest distances between the centre of the array and each detector in the configurations of the full ELIADE array respectively.

During experiments, the detector was cooled to $\sim$ 78K via an external PT100 sensors (used for detection of overflow of LN2 from detectors during a filling process) attached to a LN2 dewar, and a bias voltage of +3500 V was applied to the central core contact of each of the three working crystals. Each segment of the Compton suppression shield was read out by the R1924A Hamamatsu photo-multiplier tubes (PMT), and the +950V high voltage was applied to each Anti-Compton shield detector via the eight-channel distribution box equipped with potentiometers to modify the gain for crystals individually. Signals from PMTs were directly fed to the CAEN v1730 digitiser controlled by the DELILA data acquisition system.

The 40 output signals (32 from HPGe segments and 8 from Compton suppression) from each clover are fed to inputs of CAEN v1725 digitisers (14 bit resolution at 250 MS/s). The data acquisition system, the (D)igital (E)xtreme (L)ight (I)nfrastructure (L)istmode (A)cquisition (DELILA), is designed by ELI-NP. It is based on the MiddlewareDAQ which is in use in different research laboratories and shows good real time operation and reliability. DELILA has web-based interface and allows online visualisation of the data using a root server.

The 3 in x 3 in CeBr3 detectors were provided by SCIONIX and had R1924A Hamamatsu photomultiplier tubes. The negative -900 V bias was applied by the CAEN AG7236DN high voltage board operated in the CAEN SY4527 crate. The output signal from the photomultiplier was fed up to a v1730 CAEN digitiser (14 bit resolution at 500 MS/s). The data acquisition was made using CoMPASS Multiparametric DAQ Software. The trigger for the data acquisition was any energy signal from one of the HPGe cores above the threshold energy ($\sim$20 keV).

4.2 Gamma-ray and plutonium-beryllium neutron source

During these tests, commonly used calibration sources with well-know gamma-ray energies and branching ratios were used. For the peak-to-total ratio measurements, ^{137}Cs ($T_{1/2}$ = 30.07y), ^{60}Co($T_{1/2}$ = 5.2714y) and ^{22}Na($T_{1/2}$ = 2.6019y) were used, since a small number

of gamma-rays were emitted. For the efficiency measurements, ^{152}Eu($T_{1/2}$ = 13.542y) was used, since each of these sources have a relatively large number of gamma-rays, which cover a wide range of the energies that will be of interest for ELIADE experiments.

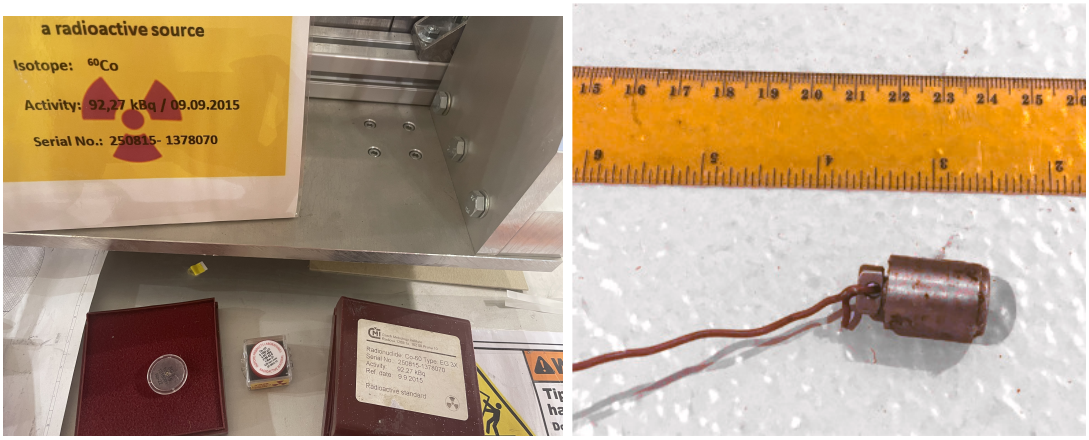

(a) (b)

Figure 4.1: Photograph of (a) calibration sources (^{22}Na, ^{137}Cs, ^{60}Co) and (b) PuBeNi source

For higher energy analysis, a plutonium-beryllium neutron source were used during the test. The isotopic composition for plutonium to be 75% ^{239}Pu and 24% ^{240}Pu, with a minor contribution from other isotopes. For more details about this source, please see [Söd+21].

4.3 DELILA: Digital Extreme Light Infrastructure List-mode Acquisition

Developing data acquisition (DAQ) software is a crucial task in modern experimental physics. In the past, researchers relied on various tools, such as pen and paper, to record scientific data. During the 19th century, mechanical oscillographs were employed for data recording. Progressing further, physicists began using silver halide film to track particles. The advent of computers enabled researchers to utilise software and hardware for data recording.

The DELILA system, as described, is designed to utilise CAEN digitisers as a key component. The CAEN digitiser handling tools form the central part of DELILA. The acquired data is transmitted through DAQ-Middleware and processed and stored using ROOT libraries.

DELILA incorporates specific components controlled by DAQ-Middleware to construct a customised DAQ system. Developers write these components by inheriting the base class of DAQ-Middleware. Each component operates independently and receives the current state from the DAQ-Middleware operator component every 10 ms. The states include config (configuration), unconfig (unconfigure), start (running), stop, and pause. In the work discussed here, the developer has added additional states as sub-states within the running state.

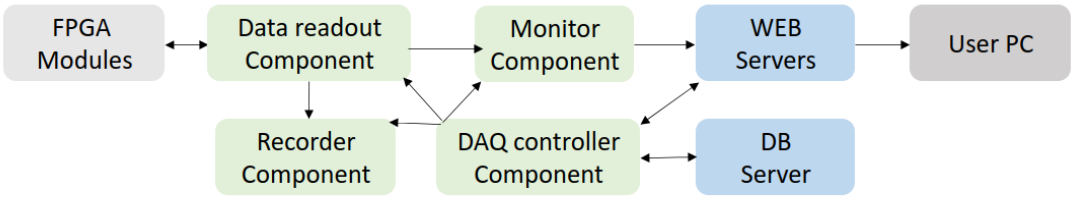

Figure 4.2: Schematic diagram of DELILA. Green show components of data taking, monitor and record, blue are the database servers. The arrows show the data transfer streams.

Figure 4.2 illustrates the schematic diagram of DELILA. The leftmost section of the diagram displays the CAEN digitisers, depicted as a light grey rectangle. The components of DELILA, based on the DAQ-Middleware template, are represented by green rounded corners and rectangles. All these components are implemented in the C++ programming language.

The data-readout component establishes communication with the CAEN digitisers to program the FPGA and retrieve experimental data. It utilises the threshold crossing information from the digitisers to calculate trigger timing. The readout component compiles the fetched data and relevant information into a packet, which is then transmitted to the

monitor and recorder components.

The recorder component is responsible for organizing the data based on timestamps and storing it. The fetched data is saved in the ROOT file format. The recorded information includes module number, channel number, timestamp, calculated trigger time, ADC (Analog-to-Digital Converters charge) information, and optionally, the trace of the signal.

In addition, the monitor component receives the packet and employs JSROOT, the JavaScript version of ROOT, to visualise and plot the data.

The chosen databases for DELILA are MongoDB and InfluxDB. MongoDB is used to store run information, such as start time, stop time, and comments for each run. On the other hand, InfluxDB is employed to record real-time event information.

For web servers, Apache is utilised to handle communication with the DAQ controller, while a web API server implemented in C++ using Oat++ is employed. Oat++ is a convenient framework that simplifies the implementation of ROOT data analysis libraries. The integration of all web server functionalities into the Oat++ server has been developed, consolidating their functions.

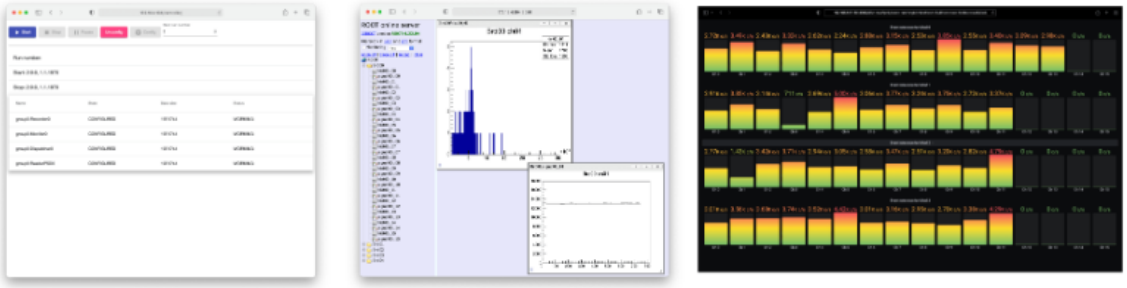

Figure 4.3: User interfaces of DELILA. From left to right, Controller of DELILA, Monitor by ROOT, Event rate monitor by Grafana.

Figure 4.3 depicts the user interfaces (UI) of DELILA. The left side showcases the controller web page, implemented using JavaScript and TypeScript. In the middle, the monitor is

displayed utilising ROOT libraries. On the right, the event rate monitor is shown using Grafana. Previously, these components were separate web pages, but efforts are being made to merge all web page applications into a single-page application.

The primary reason for developing an in-house DAQ system is to ensure future flexibility. DELILA is specifically designed to meet the requirements of experiments conducted at ELI-NP. To fulfill these needs, several requirements have been identified. The majority of codes, libraries, and the operating system used are open-source software, except for the CAEN libraries, which are proprietary. While open-source libraries could be created based on registered information from manuals, it involves the risk of illegal back-engineering and significant implementation time. Therefore, the developer opted not to use open-source libraries.

DELILA is currently deployed at the ELI-NP experimental hall and detector laboratory. Additionally, it has been tested at the IFIN-HH Tandem accelerator. The event rate monitor in Figure 4.3 displays the results obtained from that testing campaign. It is worth mentioning that DAQ-Middleware is also utilised at KEK and J-Parc in Japan.

The backend of DELILA is implemented in C++. The developer has the ability to call Linux device driver functions from DELILA and incorporate new hardware. However, if the hardware lacks manuals and driver sources, implementation becomes difficult or even impossible. In such cases, careful examination of the device driver for any new hardware is necessary.

DAQ-Middleware provides network transparency using TCP/IP and Linux's xinetd. When computers are connected within the same LAN, DELILA can handle multiple computers simultaneously. The user interfaces (UIs) are web pages, allowing control from any computer within the network.

The event rate monitor in Figure 4.3 displays an event rate of over 2,000 counts per second (cps) with 50 channels. The data size is still manageable, although the writing speed of the data poses a bottleneck. Writing data to ordinary hard disk drives (HDDs) sometimes causes the system to freeze. To address this, the developer designed the recorder component to have two main functions: sorting data and writing data. The writing function

is implemented as a child process, allowing DELILA to continue without waiting for data writing to complete. In the future, ELI-NP plans to employ a network storage system. As a result, the developer intends to create a separate data handling application that can handle large amounts of data, considering the potential challenges of a slow network environment.

4.3.1 Time gates

A method was implemented to eliminate random coincidences between X-rays and gamma rays by imposing a condition for event acceptance. In a random coincidence scenario, two gamma rays originating from separate decay events or a gamma ray and a fluorescent X-ray are detected either by the same crystal or different crystals within a specified post-trigger time window of approximately 10 microseconds. To reject these random coincidences, timing data from Time-to-Digital Converters (TDCs) were utilised to establish time acceptance gates. Events with TDC values falling within these gates were considered valid and accepted, while events outside the gates were deemed random and rejected.

Two types of time gates were employed: one for High Purity Germanium (HPGe) core timing and another for suppressor coincidence timing. These time gates were set to reject random events occurring within the crystals and suppressor segments, respectively. By applying these specific time gates, the rejection of random coincidences between X-rays and gamma rays was achieved.

- HPGe core timing

Figure 4.4 depicts a core timing spectrum for HPGe crystals. The time gate is set to 10000 ps to the triggered channel. The spectrum shows the HPGe self-timing peak near the center. Self-timing occurs for the crystal that generated the acquisition trigger, hence it appears on both sides of the beginning bin. Following this peak, there are progressively fewer counts spread over a wider range of times. Most of these counts are due to true coincidence events, wherein a gamma-ray has scattered between two or more HPGe crystals. The slight time offset is a result of variations in charge collection times, CFD (Constant Fraction Discriminator) resolution, and signal delays. At later times, any observed interactions are likely the result of randomly coincident x or gamma rays.

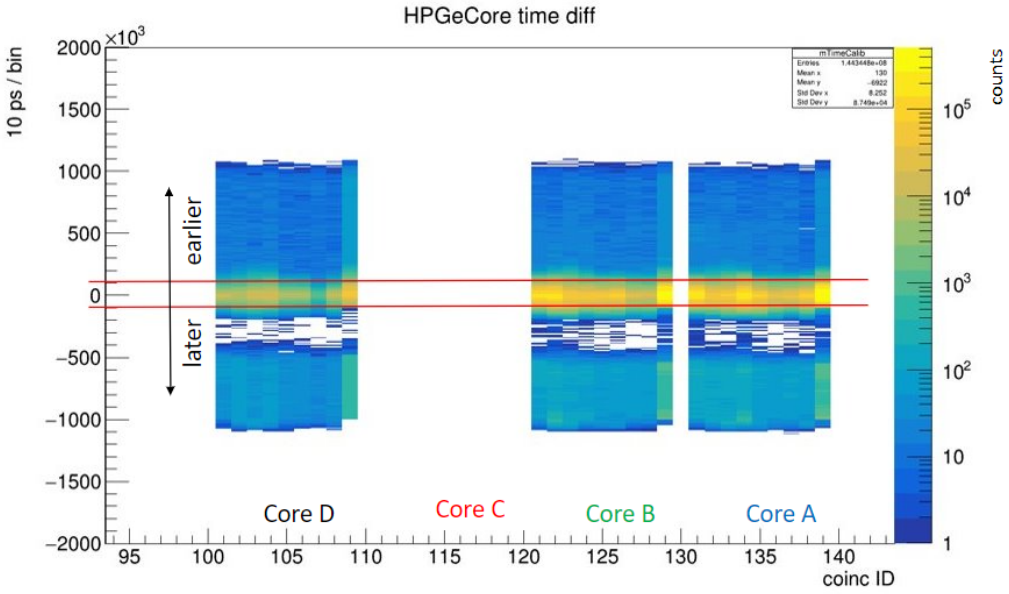

(a) matrix

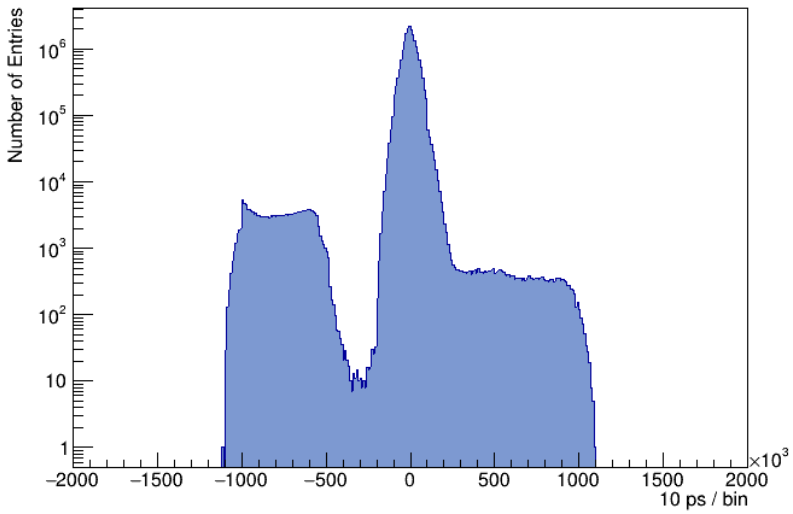

(b) projection

Figure 4.4: Top: Coincidence time difference matrix for HPGe segments to the core signals and, in red is the peaks of the time gate for the HPGe cores, which in both sides of 0 shows the interaction happened earlier or later than trigger. Bottom: Projection on time axis. The gate below zero is due to the dead time on the data acquisition.

To filter out randomly coincident events from the data, the time gate for the HPGe core spectra (as depicted in red in Figure 4.4a) was established to encompass the maximum observed true coincidence time. By applying this gate, energies recorded for a crystal were rejected if the interaction time occurred after the time gate. This rejection process effectively eliminated a significant number of randomly coincident events from the data set.

- Suppressor timing

A similar approach to the one utilised for rejecting events in the HPGe core data was implemented to eliminate random x-ray and gamma ray hits in the Compton-suppression shield. In this case, a time gate was applied to the suppressor coincidence time, which represents the duration between an HPGe core trigger event and the detection of an interaction in a suppressor channel.

Figure 4.5 illustrates a coincidence time spectrum for a suppressor channel, capturing the time differences between events. This spectrum includes events resulting from true Compton-scattered gamma rays between one of the HPGe crystals and the suppressor segment. By setting a gate on the line (highlighted in red), a significantly reduced number of randomly coincident x-rays and gamma rays were accepted as hits in the suppressor segments. This gating process effectively filtered out a substantial portion of the random coincidences, enhancing the quality and reliability of the data collected in the suppressor channels.

4.3.2 Energy thresholds

The readout process of all electronics channels using an energy trigger resulted in a significant presence of random, low-energy events caused by electronic noise. To eliminate these noise-induced events, calibrated spectra that included these counts were carefully examined. An energy threshold was determined by identifying an energy value below which the counts in the spectra were evidently attributed to noise.

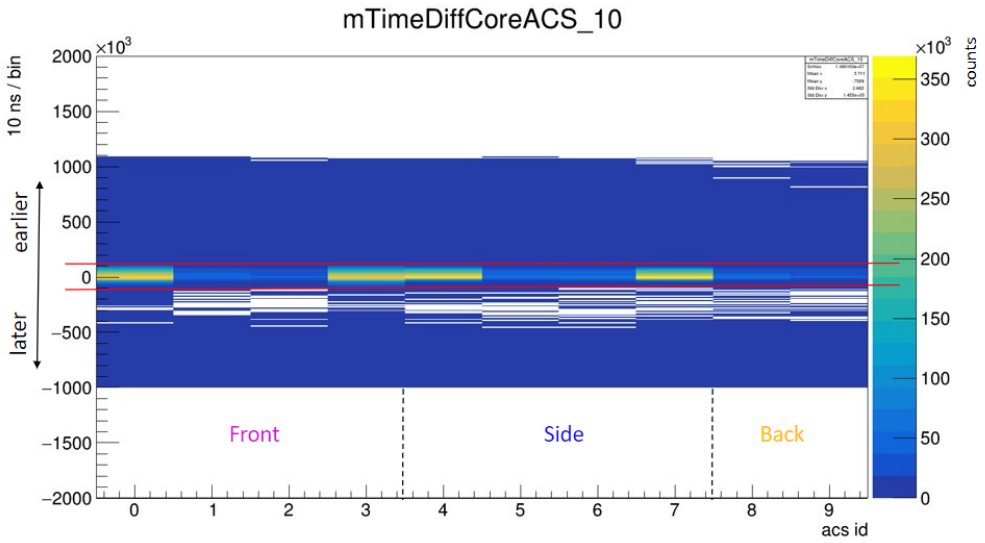

(a) matrix

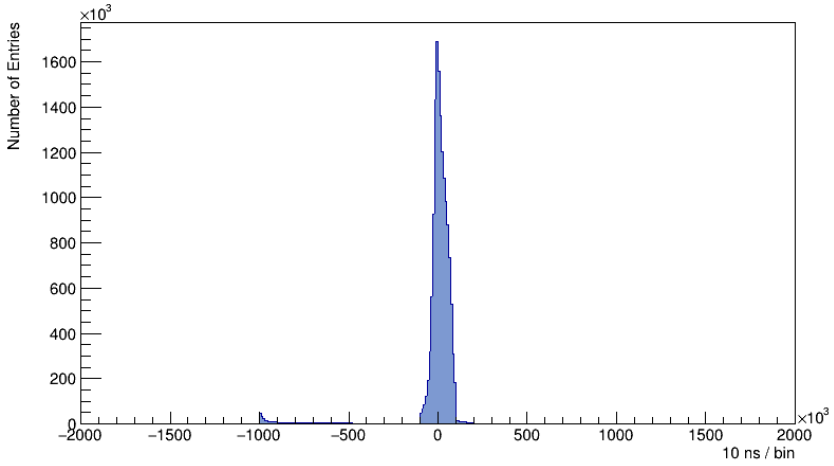

(b) projection

Figure 4.5: Top: Coincidence time difference matrix for suppressor segments to the crystals. In red is the peaks of the time gate for the suppressor segments, which in both sides of 0 shows the interaction happened earlier or later than the trigger. Bottom: Projection on x axis

Upon resorting the data, any counts below the established threshold were omitted. This

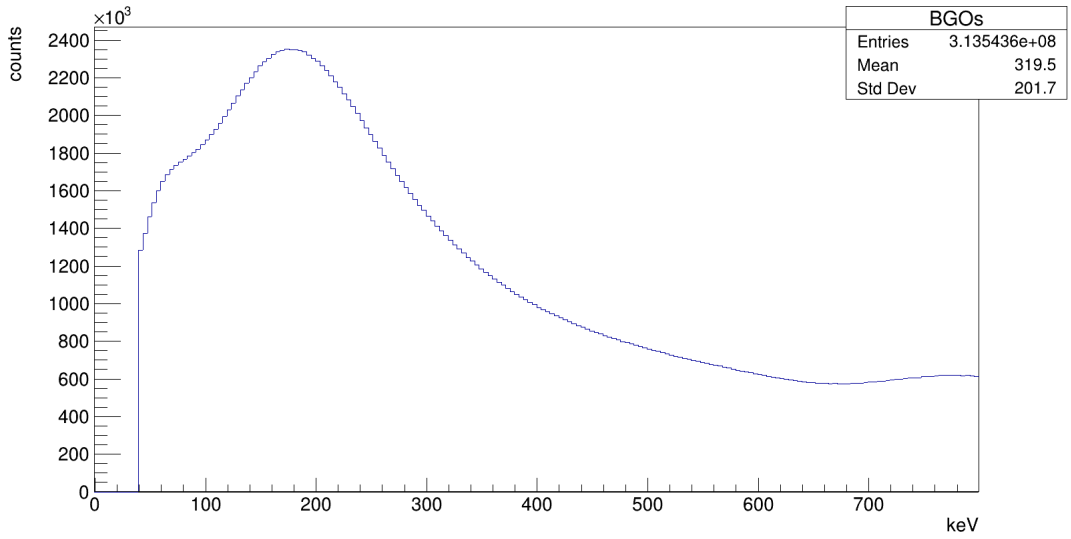

Figure 4.6: Energy spectrum for a suppressor channel in a side shield segment. An energy threshold set in software (around 40 keV) prevents counts due to electronic noise from suppressing valid events.

step ensured that only meaningful events above the noise level were retained for further analysis. As an example, Figure 4.6 shows a suppressor energy spectrum, demonstrating the effects of this threshold approach in removing noise-related counts from the data.

4.4 Analysis modes

Spectroscopy using VEGA at the ELI-NP environment encounters a big challenge due to the high intensity of the beam, which generates a very large gamma-ray background. This background stems from two sources: the pair-production of electrons and positrons that lead to a prominent 511 keV gamma-ray background, and the direct Compton scattering of the beam into the ELIADE detectors.

Although the ELIADE array's design is characterised by its high detection efficiency, this feature creates an issue when investigating high-multiplicity events, like those related to high-intensity gamma beam studies in nuclear structure. The substantial size of ELIADE crystals and their location close to the array's center contribute to this high efficiency,

increasing the chances of multiple gamma rays hit the same detector.

In the case of multiple gamma rays hitting a single HPGe clover simultaneously, even if one gamma ray transfers its full energy, the energy of that event will be subtracted from the photopeak, since it will be recognised as a single crystal event. Consequently, as the probability of multiple gamma-ray energy deposits in a crystal rises, the photopeak efficiency and peak-to-total ratio both decrease. Additionally, when one gamma-ray strikes an HPGe crystal and another hits a suppressor segment of the same detector, it may falsely suppress the signal, leading to a reduction in detection efficiency due to the rejection of actual full-energy deposits.

This chapter focuses on exploring various analysis techniques aimed at minimising the impact of high-multiplicity events' consequences. The chapter will describe the simulation-based tests conducted to evaluate the efficacy of these techniques. The objective of these tests was to enhance the sensitivity of ELIADE for different experimental conditions, especially high energy gamma-rays up to 19.5 MeV by maximizing the peak-to-total ratio and absolute efficiency.

Since the majority of the background consists of low-energy gamma-rays, in addition to optimising ELIADE sensitivity for different conditions by exploring analysis techniques, the effect of a thick attenuator in front of the detector will be examined for the same purpose. The two kinds of attenuators which tested in simulation are lead and densimet (mixture of W 97 %, Ni 1.5 %, Fe 1.5 %).

In this chapter, three analysis *modes* are discussed: *Crystals*, *Add-back* and *suppressed*.

4.4.1 Crystals

In order to generate a crystal spectrum, the energy that was deposited in each of the four crystals was added up separately to form individual spectra for each crystal. Afterwards, these individual spectra were summed to generate a spectrum that represented all the energy deposited in each crystal. In this analysis mode, peak-to-total ratio is expected to decreasing as the energy goes up, since the probability of multi-crystal events is increasing

and the chance of full energy deposited in each crystal is less.

Due to the high efficiency of the ELIADE detector, a noticeable number of random coincidence events were observed, despite the application of the time gates described earlier. Many of these events contribute energies to the spectra that are above the photopeak, with a "double peak" at twice the photopeak energy. As a result, this pile-up of gamma ray energies contributed undesired counts to the background of the spectra, this situation may dominates in this mode, especially in lower energy range since the non-selective sum up on each crystals.

4.4.2 Add-back

Instead of creating histograms of individual crystal energies and then summing them, the add-back spectra were produced by adding up the energies of all the crystals for each event and then generating histograms of the total energy. This technique allowed for the retrieval of full-energy events that occurred in multiple crystals. Consequently, there was a reduction in the number of non-photopeak counts, and an increase in the number of counts in the photopeak as compared to the individual crystal spectra. Due to the inclusion of full-energy deposition in a single crystal and the interaction of x ray or secondary gamma ray in another crystal, certain photopeak events were not captured, but in general, the add-back scheme produced a significant improvement in both the peak-to-total ratio and absolute efficiency for low gamma-ray multiplicity sources. However, it is expected that this add-back scheme will become more complicated as the energy goes up. In that case, for higher energy analysis, a measurement with a plutonium-beryllium neutron source with the energy up to 9 MeV was done in this work, the results are compared to the simulations. The increase in the number of counts in the photopeak is known as the add-back factor, $F_{a,b}$. It is defined as the ratio of the full efficiency in add-back mode over the efficiency in singles:

$$F_{a,b} = \frac{(\epsilon_p\omega)_{M=1} + (\epsilon_p\omega)_{M\geq 1}}{(\epsilon_p\omega)_{M=1}}, \tag{4.2}$$

where $\epsilon_p\omega$ is the full efficiency and M is the number of segments hitted in the event [FAB+92].

A comparison between the photopeaks from single crystals mode and add-back mode can be seen in Figure 4.7, both in experiment and simulation.

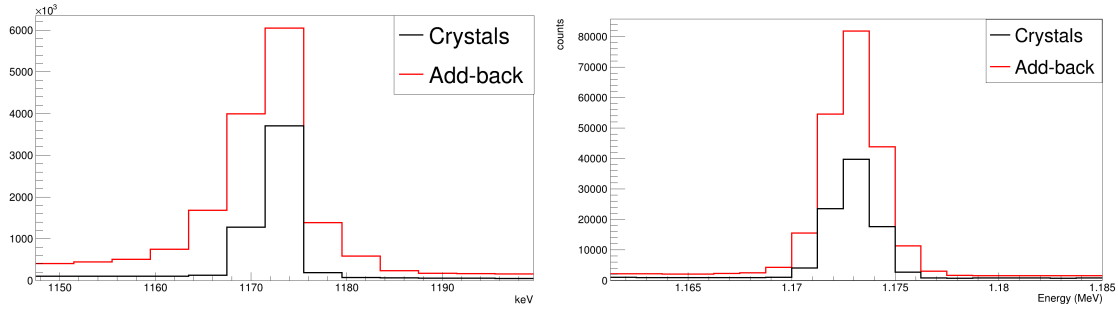

(a) Experiment (b) Simulation

Figure 4.7: A comparison between the photopeaks that result from the use of add-back analysis mode (in red) and crystal analysis mode (in black), using the 1173 keV gamma ray of ^{60}Co. The increased photopeak area for the Add-back compared to Crystals demonstrates the effect of the add-back factor. Measured with CL33, simulated in the same configuration.

4.4.3 Suppressed

The Suppressed Clover spectra were obtained by rejecting the events in which a valid crystal energy and a hit in the suppression shield occurred with the previously defined time coincidence window. Generally, using Compton suppression improved the peak-to-total ratio significantly as it prevented incomplete energy deposition events from being recorded. This can be seen from a good reduction of secondary gamma-rays in the background rather than improve the counts in the photopeak. However, it was observed that there was a slight decrease in photopeak efficiency due to false suppression. This was caused by gamma-rays interacting with the suppression shield directly. The false veto probability, which is the percentage reduction in photopeak area in a suppressed spectrum compared to a crystals spectrum, measures the amounts of false suppression that occurs. Figure 4.8 shows a comparison of the background obtained from suppression mode and crystals mode, both in experiment and simulation.

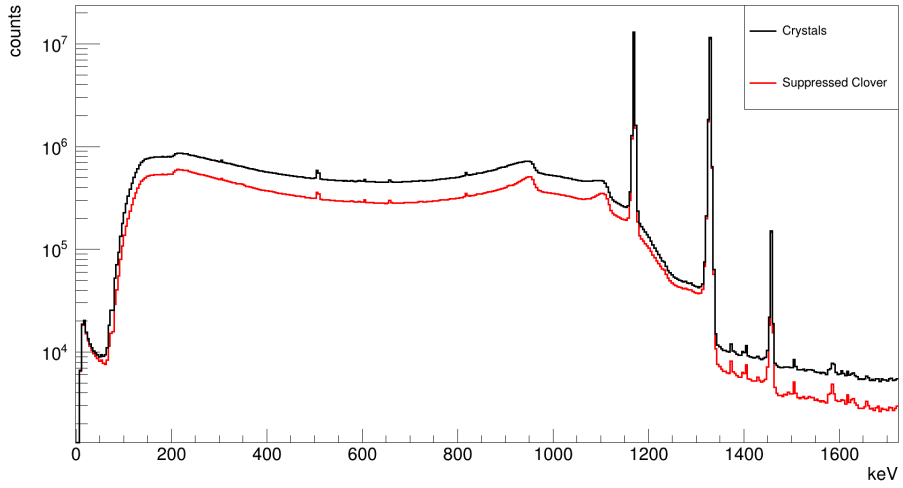

(a) Experiment

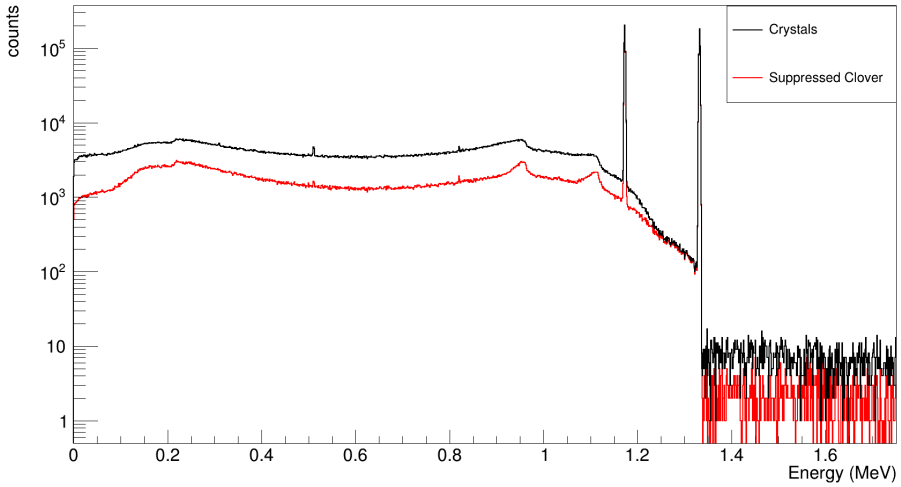

(b) Simulation

Figure 4.8: A comparison between the photopeaks that result from the use of suppressed analysis mode (in red) and crystal analysis mode (in black), using the 1173 keV and 1332 keV gamma ray of ^{60}Co source. (Measured with CL33, located near the wall, the spectrum includes a room background peak of ^{40}K in 1460 keV. Simulated in the same configuration, without natural room background.)

4.5 Passive shielding

A design of lead cover as passive shielding was used for ELIADE array initially, however due to technical issues with the local workshop and some other reasons, the lead shielding has not been mounted and measured with ELIADE detectors yet. In this work, the passive shielding was only simulated results. As for the Ge detectors one has to use passive shielding of these detectors to protect them from the scattered radiation off the surrounding materials. Those absorbers will be used in front of the detectors to reduce the level of background radiation.

One method for decreasing the radiation background detected by the sensors is to increase the distance between the detector and the target. This will result in a decrease in the solid angle covered by the detectors. Unfortunately, this approach also reduces the detection efficiency for the specific gamma rays of interest. In the case of high-energy gamma rays, a way to reduce the background radiation below 500 keV is to place lead and copper absorbers in front of the detectors. The impact of using a thick Pb shield in front of the detector was evaluated using GEANT4 simulation, which calculated the response of the clover detector to photons with energies ranging from 500 keV to 10 MeV emitted from the center of the array. The simulation results are shown in the Figure 4.9. The significance of these absorbers is well-known based on previous NRF configurations. [Ur+16]

These graphs illustrate the variations in absolute efficiencies and peak-to-total ratios as a function of photon energy, comparing scenarios with and without a 2 cm Pb absorber positioned in front of the Ge detectors. The figures demonstrate that the Pb absorber effectively decreases the radiation background caused by gamma-rays with energies below 500 keV. However, this reduction comes at the expense of a considerable decline in the absolute detection efficiency at higher energies, as well as a notable deterioration in the quality of the gamma-ray spectra, evident in lower peak-to-total values.

Considering the potential influence of shielding material on the higher energies, we also run the simulation to see the effect on absolute efficiencies and peak-to-total ratios with an alloy of densimet instead of lead. The parameters used to define densimet is W 97%, Ni 1.5% and Fe 1.5%, with a density of 18.5 g/cm^3. In this simulation, the energy range from

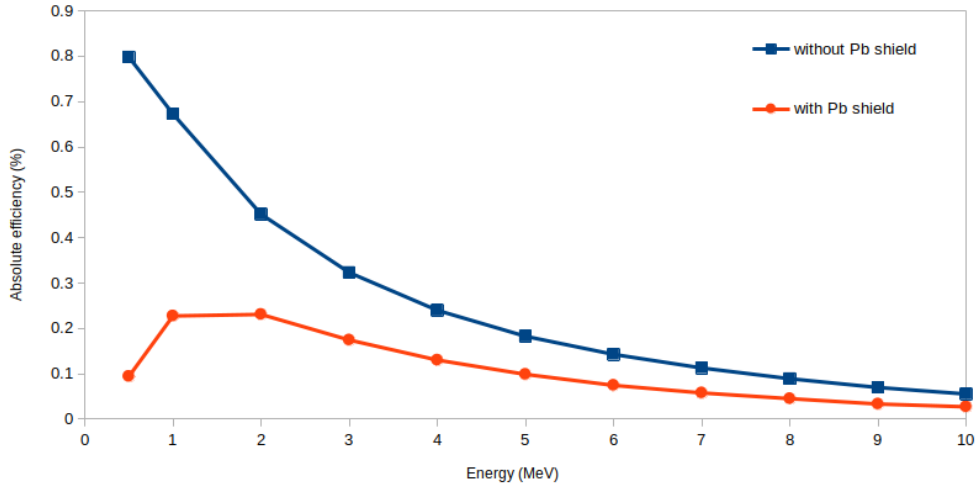

(a) Efficiency

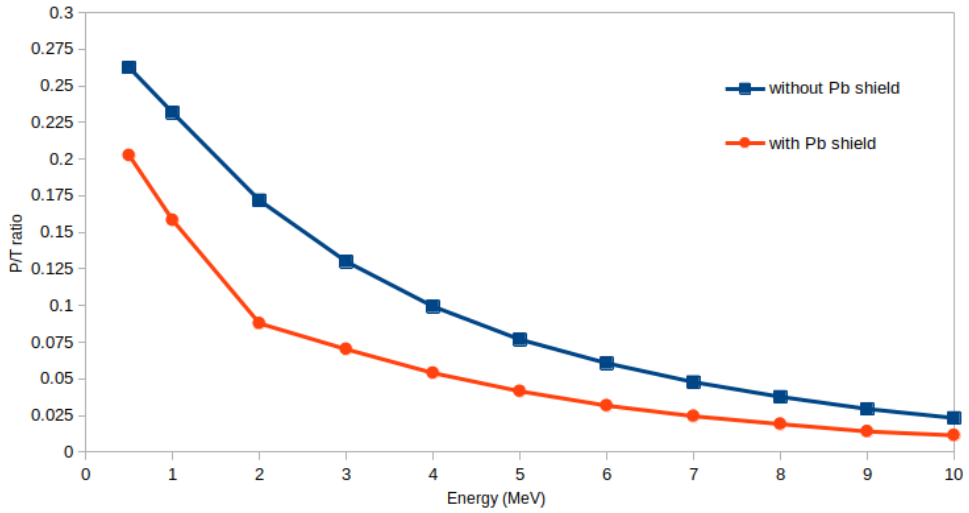

(b) Peak-to-Total

Figure 4.9: GEANT4 simulation of the clover detectors response to photons with energies between 500 keV and 10 MeV with (filled orange circles) and without (filled blue squares) a 2 cm thick Pb absorber in front of the detector. Error bars are too small to be seen from the figures.

1 to 20 MeV was employed since higher energies are of greater interest to this program.

The absolute efficiencies and the peak-to-total (P/T) ratios are plotted as a function of the photons energy with a 2 cm Pb absorber and Densimet absorber placed in front of the Germanium detectors. It can be seen in Figure 4.10, the difference of absolute efficiencies and peak-to-total ratios becomes very small as the energy goes up, therefore the choice of materials for passive shielding is limited to the cost.

4.6 Results

The sorting and histogramming procedures described in the previous section were performed on data taken for the sources described in chapter 4.2. Data were collected for each source with CL33, with suppressor segments and passive shieldings.

4.6.1 Peak-to-Total

Four sets of spectra were created for the four sources used for the determination of peak-to-total ratios, which can be seen in Figures 4.11 and 4.12. The peak-to-total ratios for all measurements obtained with ^{137}Cs, ^{60}Co, ^{22}Na and PuNeBi neutron source, all placed in a source to detector surface distance of 14.5 cm, are summarised in Table 4.1. In determining these numbers, counts in x-rays peaks (due to fluorescence from the detector or source materials), as well as counts due to back-scattered gamma-rays from the opposing wall, were subtracted from the overall total in order to determine the denominator for each peak-to-total calculation.

The peak-to-total ratios for ^{60}Co source were calculated with the sum of area in two peaks, 1172 keV and 1332 keV. For ^{22}Na source, the interested energy peak is 1274 keV, therefore the peak-to-total ratios were calculated with the area of 1274 keV peak only. The peak-to-total in simulation for ^{22}Na source is also designed to use only 1274 keV peak,

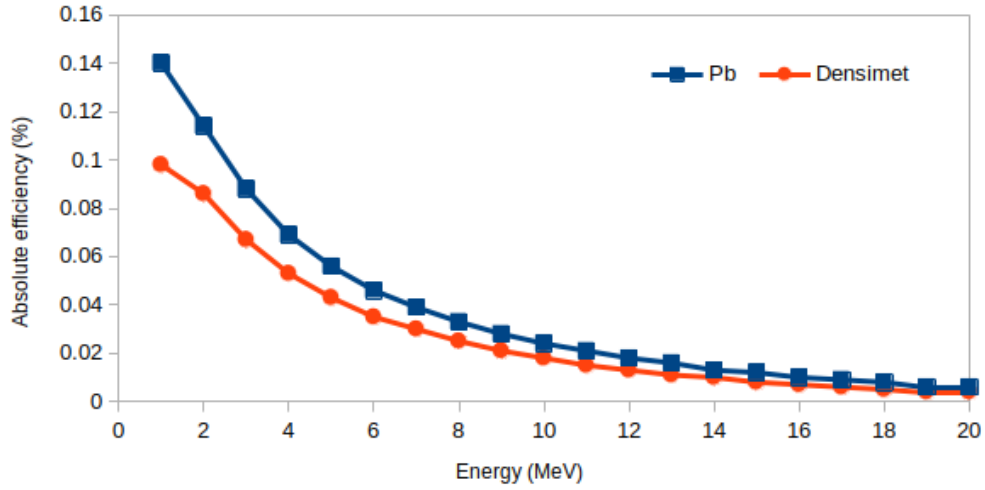

(a) Efficiency

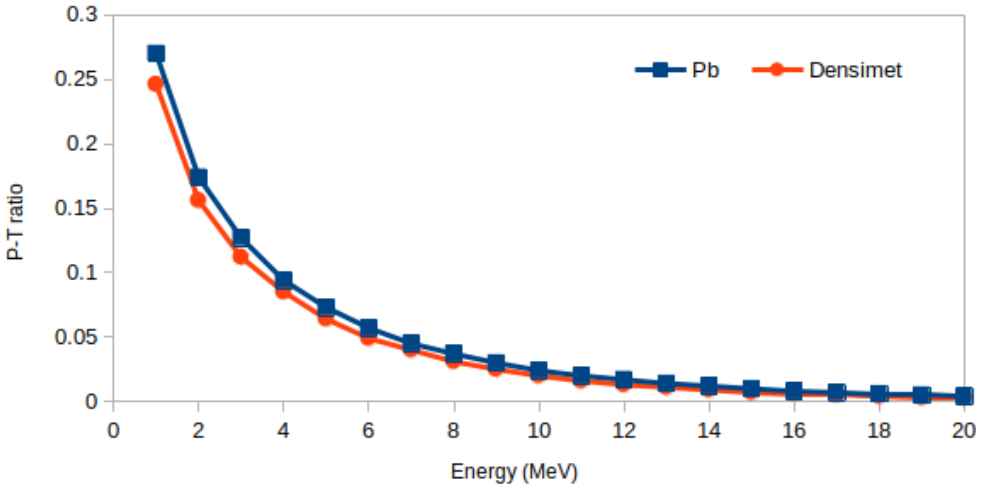

(b) Peak-to-Total

Figure 4.10: GEANT4 simulation of the clover detectors response to photons with energies between 1 MeV and 20 MeV with a 2 cm thick Pb absorber (filled blue squares) and Densimet absorber (filled orange circles) in front of the detector.

Source	P/T	Exp	Sim
^{137}Cs	P/T Crystals (%)	26.7(3)	26.3(3)
	P/T Suppressed (%)	45.4(2)	45.9(2)
	Add-back Factor	1.32(6)	1.28(4)
^{22}Na	P/T Crystals (%)	27.2(3)	21.4(1)
	P/T Suppressed (%)	36.6(3)	40.2(1)
	Add-back Factor	1.30(1)	1.28(1)
^{60}Co	P/T Crystals (%)	16.2(8)	18.0(9)
	P/T Suppressed (%)	35.3(8)	35.5(7)
	Add-back Factor	1.48(1)	1.30(1)
PuBeNi	P/T Crystals (%)	5.5(3)	29.8(5)
	P/T Suppressed (%)	14.6(7)	48.3(4)
	Add-back Factor	2.32(1)	2.32(1)

Table 4.1: Experimental and simulated peak-to-total ratios (P/T) for test sources, measured with the prototype ELIADE detector CL33 in a distance of 14.5 cm from the surface, with Anti-Compton shields, same condition for simulations. (For results with the PuBeNi neutron source, due to the low statistics around the 9000 keV peak, a selection of a range from 8560 to 9500 keV were used to determine the peak-to-total ratio in measured data, for simulation, a 9 MeV gamma point source was used as the PuBeNi neutron source was not yet implanted, therefore the P/T ratio here is very different.)

instead of the whole gamma spectrum for ^{22}Na. For results with the PuBeNi neutron source, due to the low statistic around the 9000 keV peak (obtained from neutron capture reactions in ^{58}Ni following moderation of the neutron field), a selection of a range from 8560 to 9500 keV were used to determine the peak-to-total ratio.

All the experimental data were compared with simulation results, which can be seen in Table 4.1 and Figures 4.11 and 4.12.

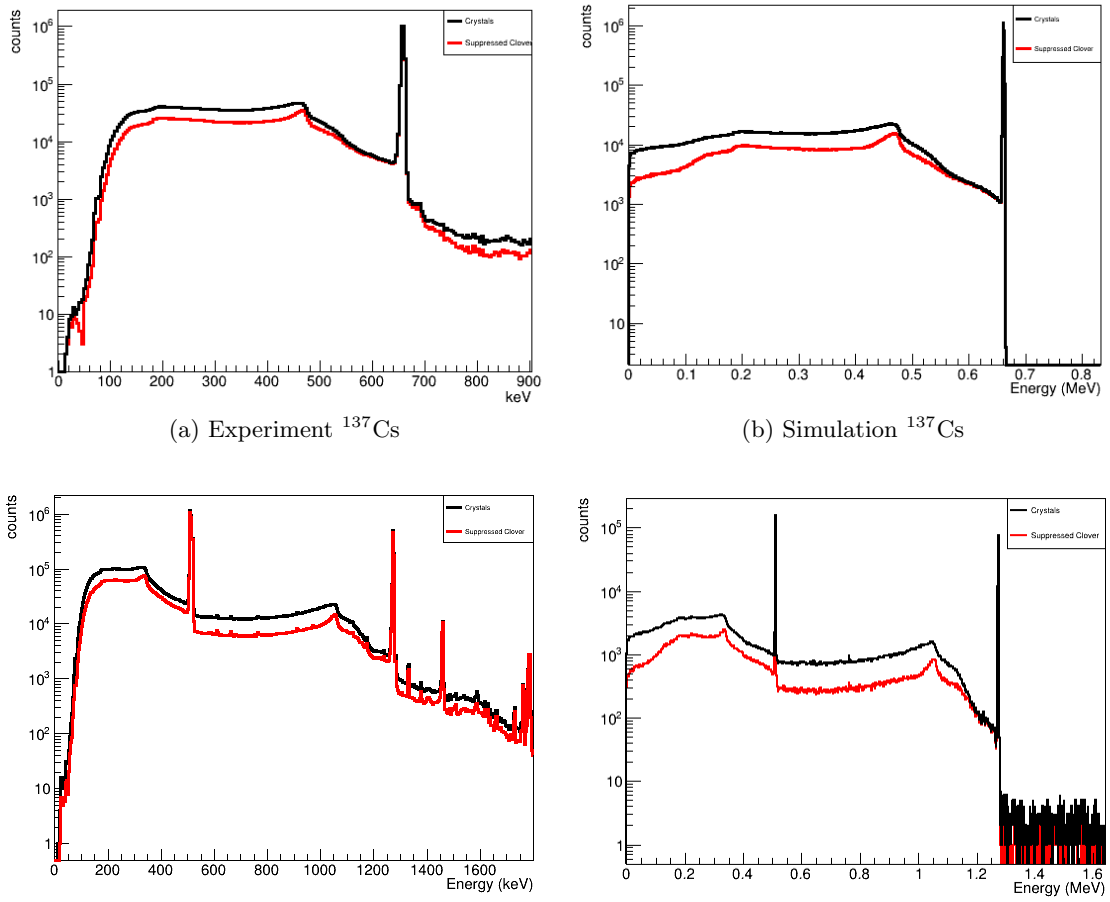

(a) Experiment ^{137}Cs

(b) Simulation ^{137}Cs

(c) Experiment ^{22}Na

(d) Simulation ^{22}Na

Figure 4.11: Every spectra for the ^{137}Cs and ^{22}Na sources in suppressed analysis mode (in red) and crystal analysis mode (in black), taken with the prototype ELIADE detector CL33 at a distance of 14.5 cm from the surface. The measured spectrum includes a room background peak of ^{40}K in 1460 keV (not present in the ^{137}Cs spectrum due to the scale). Simulated in the same configuration, without natural room background. Displayed with logarithmic "Counts" axis.

For the ^{137}Cs and ^{60}Co source, P/T in crystals mode and Suppressed mode from experiment and simulation are in good agreement. While for the ^{22}Na source, a slightly

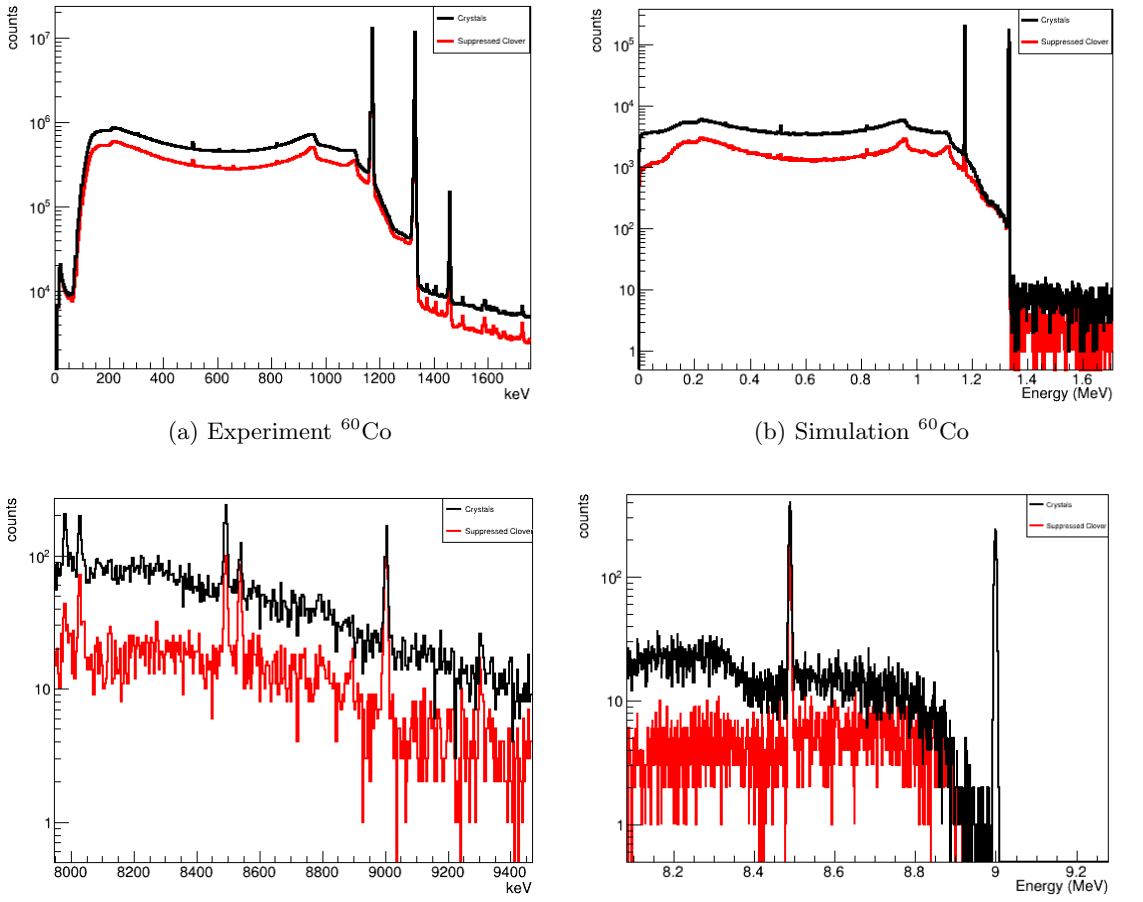

(a) Experiment ^{60}Co

(b) Simulation ^{60}Co

(c) Experiment PuBeNi

(d) Simulation 9MeV

Figure 4.12: Spectra for the ^{60}Co and PuBeNi sources in suppressed analysis mode (in red) and crystal analysis mode (in black), taken with the prototype ELIADE detector CL33 at a distance of 14.5 cm from the surface. The measured spectrum includes a room background peak of ^{40}K in 1460 keV (not present in the PuBeNi spectrum due to the scale). Simulated in the same configuration, without natural room background. Displayed with logarithmic "Counts" axis.

bigger difference in the P/T ratio is related to the use of mixture background sources (^{60}Co) for energy calibration when taking the measurement. For PuBeNi source, due to the low statistics and lack of time, the implantation of the neutron source is not finished in simulation, instead a 9 MeV point gamma ray source was used in the simulation to be compared with experimental data, therefore the peak-to-total ratios in this energy peak

will be different for the measured and simulated data. However, it can still be comparable since the interest energy range for the test is in the same range.

4.6.2 Add-back factor

At this point, a standard source holder was designed and 3D printed, so we started some test measurements in a distance range from 0 to 25 cm from the centre of detector surface. So the analysis from now on is varied on distance. Also since Add-back factor analysis is not required for Compton suppression, for better comparison with simulated result, the measurements related to this were taken with CL29 which has all four crystals working but no Compton suppression. As well as the efficiency and resolution measurements.

As discussed in chapter 4.4.2, the calculated Add-back factors measured over the energy range from 661 keV to 9000 keV for the ELIADE detector is shown in Figure 4.13 at a distance of 25 cm. A weighted second-order function of the form,

$$F = a + b(x), \qquad x = \ln(E_\gamma), \tag{4.3}$$

was fitted to the experimental values for gamma-ray energies greater than 661 keV, using a logarithmic fitting. The parameters of the best fit were found to be -1.5704 and 0.4221 for a, b respectively. These experimental add-back factors are close to those measured for other clover HPGe detectors [Wil+96] [Riz+16].

An Add-back factor over the distance from 0 to 25 cm is also shown in Figure 4.14.

In this figure, the add-back factor reduces from a distance of surface to around 10 cm, and then nearly linear.

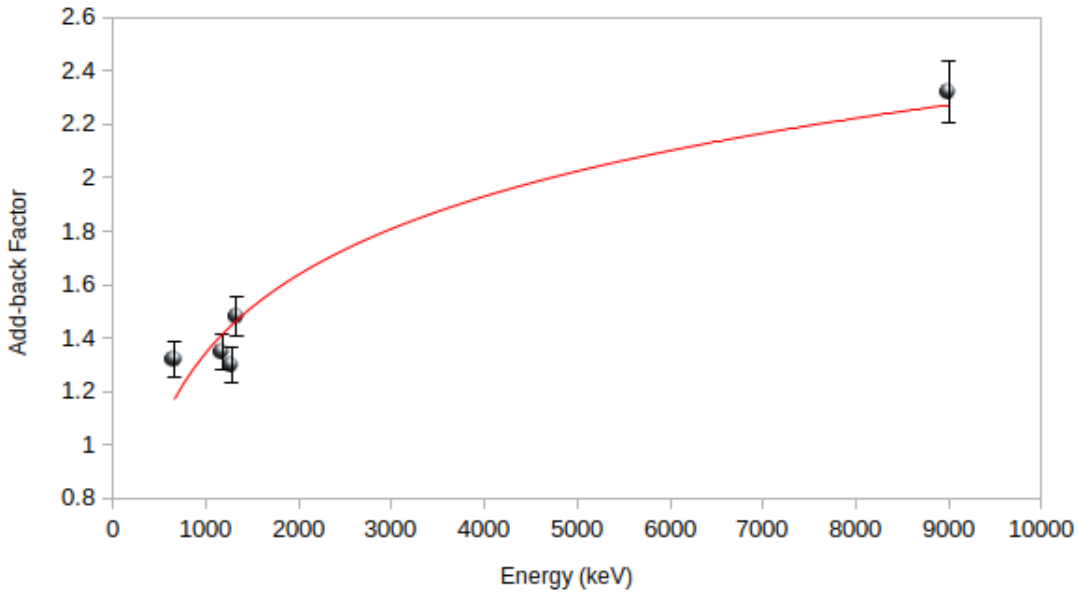

Figure 4.13: Measured add-back factors over energies of the ELIADE detector is shown. (Measured with CL29 which has four crystals working but without Compton suppression.)

4.6.3 Efficiency

The relative efficiency functions for the prototype ELIADE detector were determined using ^{152}Eu source. Figure 4.15 shows the measured relative full energy peak efficiencies for four cores in crystals. The energy calibration is determined in function $E_\gamma = A + B * Ch$, where E_γ is the gamma-ray energy, Ch is the spectral channel number for the center of the peak corresponding to E_γ, A and B are constants to be determined for calibration. Table 4.2 shows the details of efficiency measurements using ^{152}Eu source with CL29.

4.6.4 Energy resolution

In addition to determining the peak-to-total ratios and relative photopeak efficiency for the ELIADE prototype detector, the energy resolution was examined as well. The energy

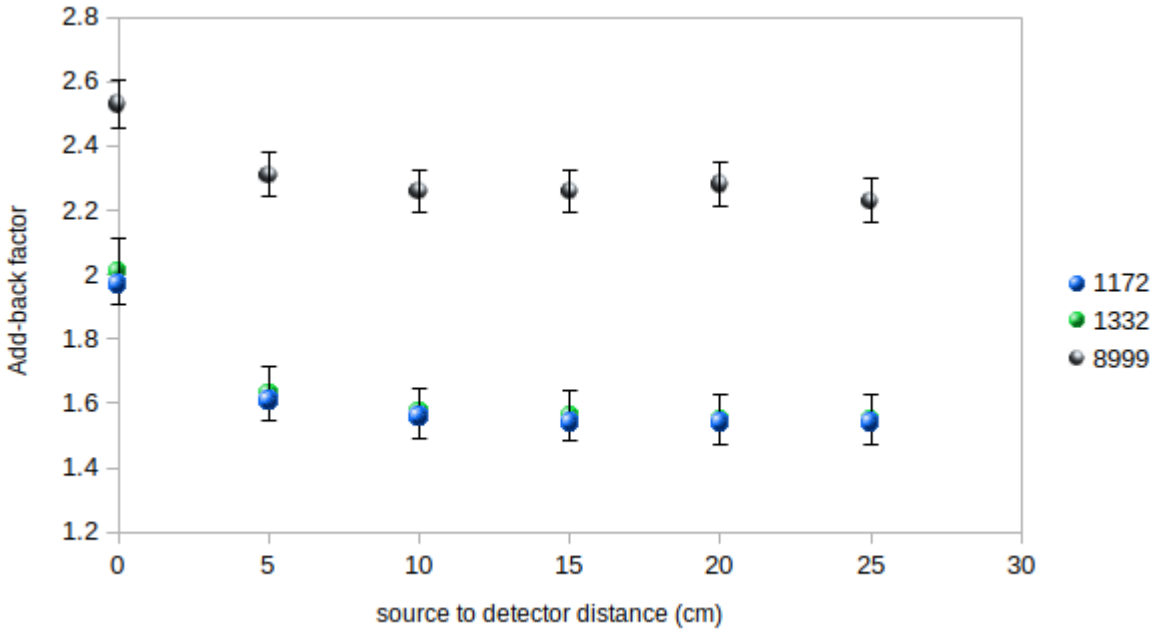

Figure 4.14: Measured add-back factors over distance of the ELIADE detector is shown. (Measured with CL29 which has four crystals working but without Compton suppression, source placed in the centre of detector surface.)

resolution function is usually quoted as the Full-Width at Half-Maximum (FWHM) of photopeaks as a function of gamma-ray energy. A ^{152}Eu source was used during the energy resolution measurement. Figure 4.16 and Table 4.3 shows the measured FWHM in four crystals with ELIADE detector CL29.

4.7 Summary

In this chapter, details of the experiment set up, apparatus and test sources were presented, as well as the DELILA Acquisition including time gates and energy thresholds. Three analysis modes: *Crystals*, *Add-back* and *suppressed* were discussed. Performance both

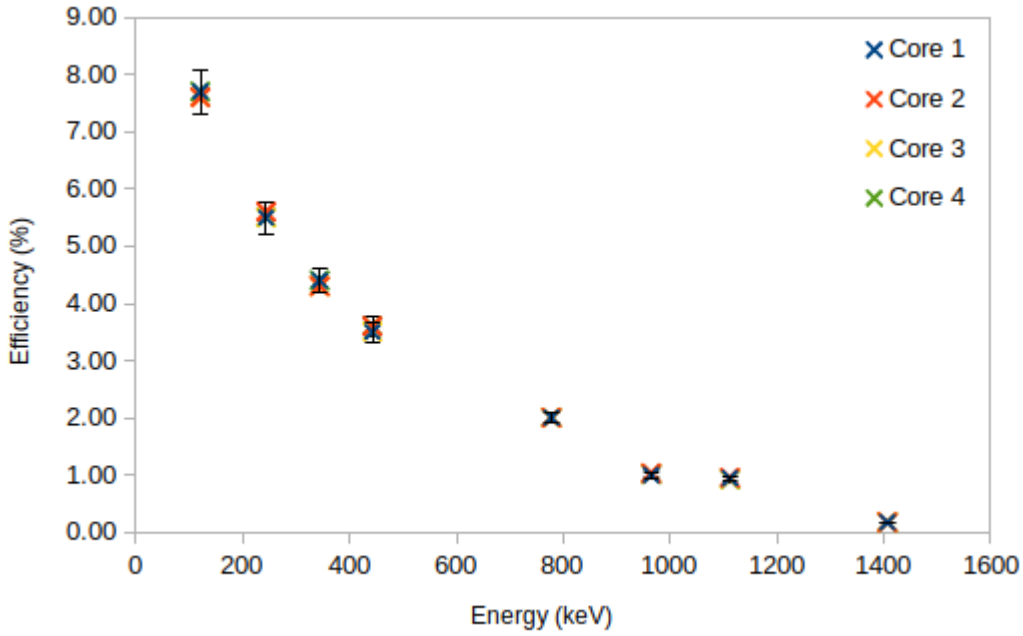

Figure 4.15: Relative efficiency of the ELIADE detector in four crystals is shown. Measured with CL29.

Energy	**Core 1**	**Core 2**	**Core 3**	**Core 4**
keV	%	%	%	%
121.7	7.7	7.6	7.6	7.7
244.6	5.5	5.6	5.5	5.5
344.2	4.4	4.3	4.3	4.4
443.9	3.5	3.6	3.5	3.6
778.8	2.0	2.0	2.0	2.0
965.6	1.0	1.0	1.0	1.0
1112.1	0.9	0.9	0.9	0.9
1407.9	1.7	1.7	1.7	1.7

Table 4.2: Relative efficiency measurements for ^{152}Eu source, measured with CL29.

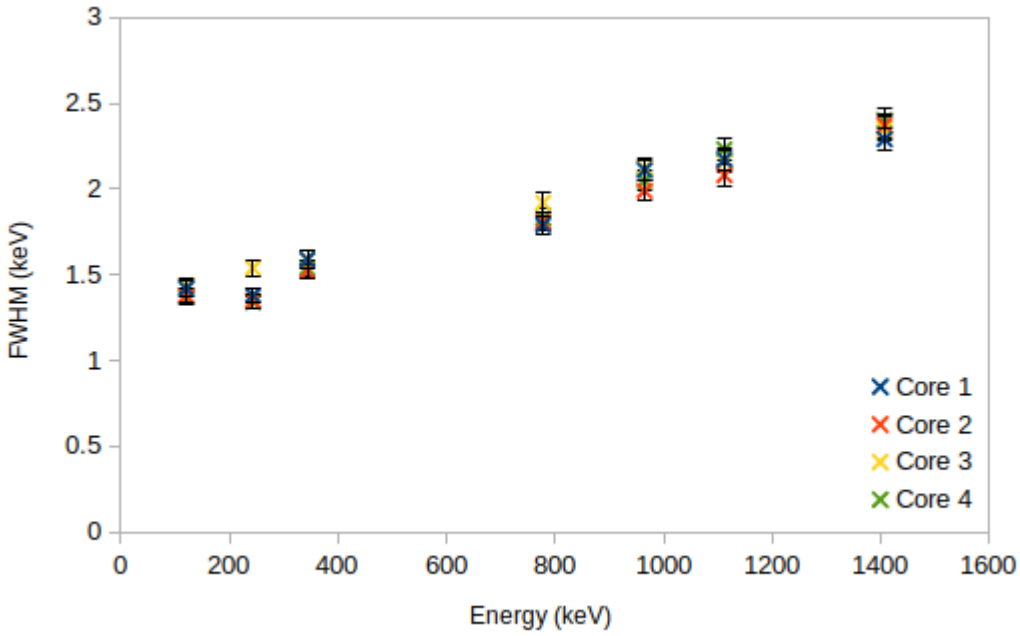

Figure 4.16: FWHM energy resolution (in keV) of the ELIADE detector in four crystals is shown. Measured with CL29.

Energy	**Core 1**	**Core 2**	**Core 3**	**Core 4**
keV	keV	keV	keV	keV
121.7	1.42	1.38	1.44	1.37
244.6	1.38	1.35	1.54	1.34
344.2	1.59	1.52	1.59	1.54
778.8	1.79	1.81	1.92	1.83
965.6	2.11	1.99	2.12	2.05
1112.1	2.17	2.08	2.16	2.23
1407.9	2.29	2.37	2.35	2.4

Table 4.3: FWHM energy resolution measurements for ^{152}Eu source. Measured with CL29.

in experiment and simulation were shown and compared. A test of passive shielding in simulation was done with Pb and densimet material, peak-to-total ratio and absolute efficiency were shown and discussed.

The sensitivity of a High-Purity Germanium gamma-ray spectrometer was evaluated through experimental measurements of three key indicators: photopeak efficiency, peak-to-total ratio, and energy resolution. Results on these three parameters were tested and discussed. Add-back factor as a function of energy was presented. All these measurements were conducted using the prototype ELIADE 32-fold segmented HPGe clover detector CL33 (3 crystals with Compton suppression) and CL29 (4 crystals without Compton suppression).

Chapter 5

ELIADE gamma-ray spectrometer

5.1 HPGe developments

Composite Clover detectors

An array specifically designed for nuclear spectroscopy requires certain key characteristics, including a large efficiency, high granularity, high throughput, and high sensitivity, which refers to its ability to detect a peak over the Compton continuum. Composite Clover detectors were developed in the 1990s with the primary aim of improving Doppler correction [Duc+99]. These detectors consist of four 25% relative efficiency HPGe crystals, clustered together in one cryostat, operating in add-back mode. In add-back mode, when several crystals are triggered simultaneously, their energies are summed up, resulting in a single add-back spectrum. This add-back technique allows for a total relative efficiency of 130% for the entire detector. The smaller size of the crystals reduces their solid angle, resulting in less Doppler broadening of peaks. As a consequence, these detectors were positioned at a 90° angle relative to the beam direction. Composite Clover detectors are known for their high reliability and lower sensitivity to radiation damage compared to large volume detectors due to the smaller size of their crystals. As a result, they have become a standard tool in the field of gamma-ray spectroscopy research. Moreover, their original design also allows them to be used as gamma-ray polarimeters [Jon+95]. Alongside these developments, other advancements in HPGe technologies have emerged, such as crystal encapsulation [Ebe+96], which facilitates easier maintenance by protecting the HPGe crystal within a sealed aluminum canister.

The technology of crystal encapsulation has made it possible to create composite detectors like the EUROBALL cluster detector [Ebe+90], which consists of 7 large volume crystals enclosed in protective casings.

Segmented Clover detectors

A significant advancement came with the introduction of HPGe segmentation [Gut90], which marked a major step forward in the array's granularity. The crystal is divided into multiple subsections, or segments, with each segment having a smaller solid-angle compared to the whole crystal. The segmentation is achieved by implanting boron on the external surface of the n-type crystal in a specific 2D pattern, creating several electrodes instead of a single one. Holes generated in the crystal are then collected in these segments, allowing for direct information about the interaction location. The electrons, on the other hand, are all collected on the n+ Li-contact, called the Core, which retains the full energy information of the crystal.

This segmentation technique has shown great potential for Doppler broadening correction and has been utilised in various arrays designed for low-multiplicity, high velocity in-beam measurements, including MINIBALL (6-fold) [Ebe+01], EXOGAM (16-fold) [Sim+00] and ELIADE (32-fold). By employing segmentation together with digital electronics, the analysis of the leading-edge shape of output signals enables precise localization of the first interaction with sub-segment precision. This feature has inspired the concept of developing an array capable of performing gamma-ray tracking, such as a HPGe shell.

5.2 ELIADE array description

The ELI Array of DEtector, or ELIADE, is a set of detectors located at the ELI-NP (Extreme Light Infrastructure - Nuclear Physics) research facility in Magurele, Romania, which is part of the ELI project. ELIADE is a unique array of detectors that is used to detect and measure the properties of high-energy photons and particles produced by the high-power laser systems at ELI-NP. It provides unique capabilities for the characterization of the high-energy photons and particles produced by the ELI-NP laser systems, and is used for a wide range of research applications, including high-energy physics, nuclear physics, material science and medical physics. It consists of 8 segmented Clover 32-folded High

Purity Germanium (HPGe) detectors arranged at a distance up to 25 cm from the target into two rings at 90 ° and 135 ° to the beam direction. Each ring comprises four Clover detectors. In order to enhance sensitivity to the high-energy gamma-rays, four large volume ancillary (3 in x 3 in) $CeBr_3$ detectors are installed in the 90 ° ring in a way that the polar angle between the Clover and $CeBr_3$ detectors in the ring is 45 ° with respect to the target position. See Figure 5.1.

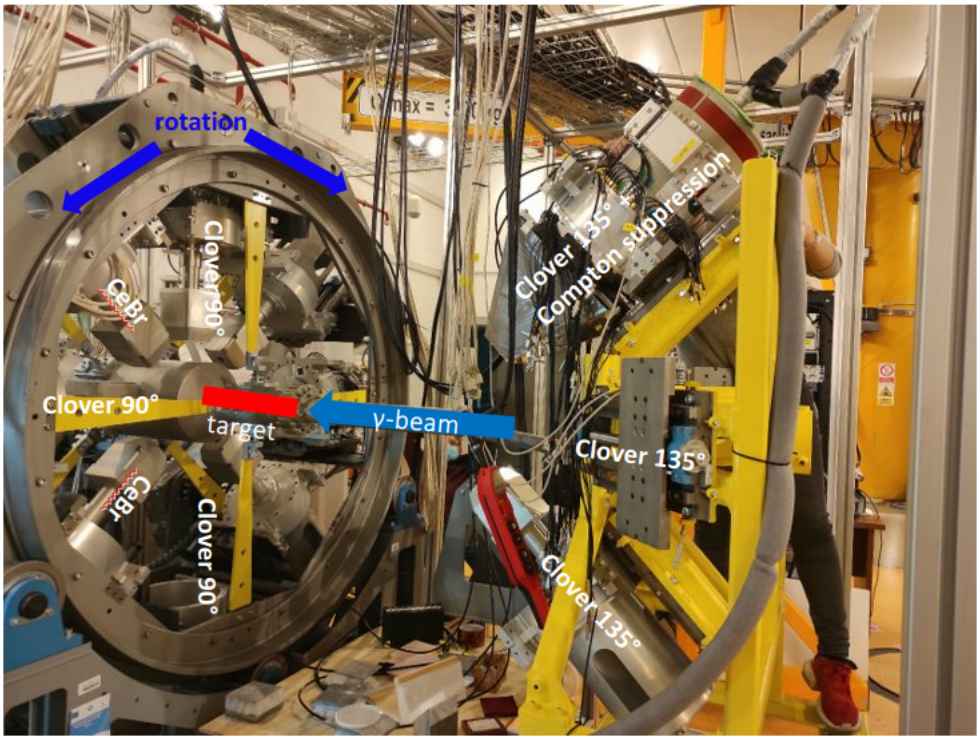

Figure 5.1: The ELIADE gamma-ray spectrometer partly installed in the experimental hall. Clover and CeBr3 detector arrangements in the 90° structure on the left, the 135° structure on the right. [The author can be seen behind the frame :)]

Due to the very high photon beam intensity, a very large number of 511 keV photons from positron annihilation will reach the detectors together with the high energy photons from the NRF reaction of interest. This number can be decreased by the use of passive shields, designed in a modular fashion that allows them to become one of the user-defined

experimental conditions. In the ELIADE configuration, active Compton suppression shields are also used. These shields are of modular type being composed of three different types of shields: a rear side shield made of BGO, a side shield made of BGO and a back catcher made of CsI. The detector's cryostats are fitted with holders for the modular anti-Compton shields. [Ur+16].

5.2.1 32-Fold segmented HPGe clover detectors

The approaches aimed at decreasing the radiation background inadvertently diminish the advantages offered by a high brilliance gamma beam. To fully capitalise on the gamma beam's capabilities and the high detection efficiency for gamma rays, the current Technical Design Report (TDR) suggests employing segmented clover detectors. This allows for the optimal utilisation of the gamma beam's characteristics while maintaining a favorable detection efficiency for gamma rays.

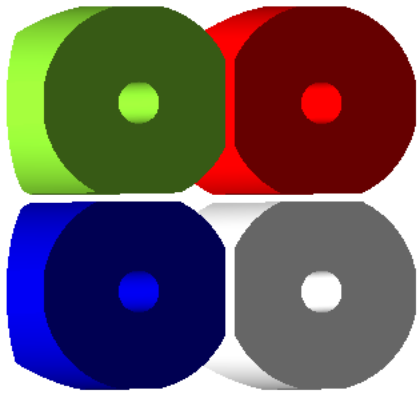

Figure 5.2: The rear view of the ELIADE HPGe clover reveals its configuration, which consists of four HPGe cylinders cut to meet at flat sides with a slight 0.6 mm gap between them. A central electrical contact will be established through a 10 mm diameter hole bored in the center of the clover. (GEANT4 view)

Each of the eight detectors in the ELIADE array will incorporate a HPGe clover (manufactured by Canberra), which will consist of four HPGe cylinders cut to align along flat edges, enabling efficient packing into a square geometry, see Figure 5.2. These four HPGe

crystals will be housed within a common vacuum cryostat and maintained at a temperature of approximately 100 K through a metal cooling structure extending into a liquid nitrogen dewar. The initial diameter of the four cylinders will be 60 mm, but they will be cut along chords to ensure that the inner surfaces are at least 27.2 mm away from the central axis, while the outer sides maintain a minimum distance of 29.3 mm from the central axis.

Figure 5.3: The side view of the ELIADE HPGe clover reveals its configuration. The HPGe will be tapered on the outer faces, and in cones on the corners, on an angle of 22.5° to a depth of 36.2 mm. (GEANT4 view)

The HPGe clover has a total length of 90 mm, with the first 36.2 mm tapered at an angle of 22.5° along the outer faces and in a cone around the corners, as illustrated in the Figure 5.3. This tapering facilitates close-packing of the detectors in the array. Additionally, a hole will be bored along the central axis, starting from the back (as shown in the Figure 5.2) and extending to a depth of 75 mm, which is approximately 15 mm from the front face of the clover.

One key distinction between the ELIADE HPGe crystals and standard coaxial HPGe detectors is the segmentation of the outer boron-implanted surface. Thin gaps will be left between implanted areas, resulting in longitudinal segmentation of each of the four crystals into four quadrants. Additionally, a lateral segmentation line will divide the crystals into front and back sections, as depicted in the Figure 5.4. This arrangement will yield a total

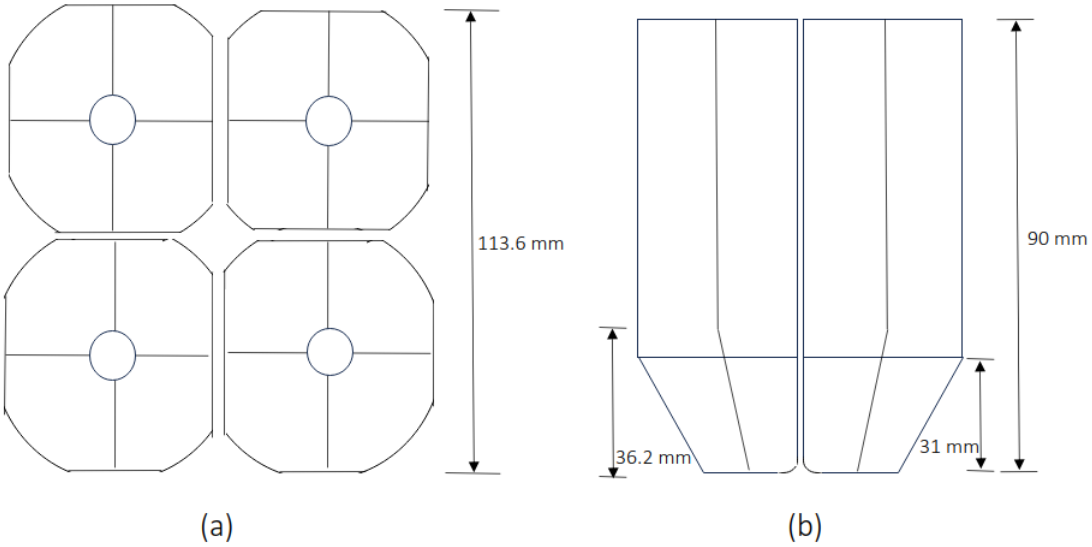

Figure 5.4: Each ELIADE HPGe crystal will be electrically segmented longitudinally along two axes as shown in (a), in addition to being segmented laterally at a depth of 31 mm, as shown in (b). These segments are not physical, they are a consequence of the segmentation of the boron-implanted electrical contacts.

of eight outer-contact segments per crystal, amounting to thirty-two segments per clover. In addition to these, there will be four central core contacts, bringing the total number of electrical signals from the clover to thirty-six. The longitudinal segmentation will be situated at the mid-lines of the squared-off crystals, while the lateral segmentation line will be positioned at a depth of 31 mm. The primary purpose of this segmentation is to enable three-dimensional localization of gamma-ray interactions within the HPGe detector. With charge-sensitive preamplifiers, all thirty-six electrical signals will be read out, providing precise energy information from the core contact and position localization signals from the outer contacts.

5.2.2 10-fold segmented Compton suppression shields

Each ELIADE detector will be equipped with a Compton-suppression shield, comprising ten optical segments made of scintillator materials: eight segments will be composed of

bismuth germanate (BGO), and the remaining two segments will be made of cesium iodide (CsI). This shield design incorporates front, side, and back shields, allowing the suppression shield to cover the tapered part of the HPGe clover. The arrangement of the suppressor segments in relation to the HPGe clover is depicted in Figure 5.5. The front shields will consist of four physically separated pieces, each containing one optically-segmented BGO crystal, with a thickness of 1 cm. The side shields, symmetrically arranged as shown in Figure 5.6, will have a thickness of 2 cm and will house four optical segments in the same casing.

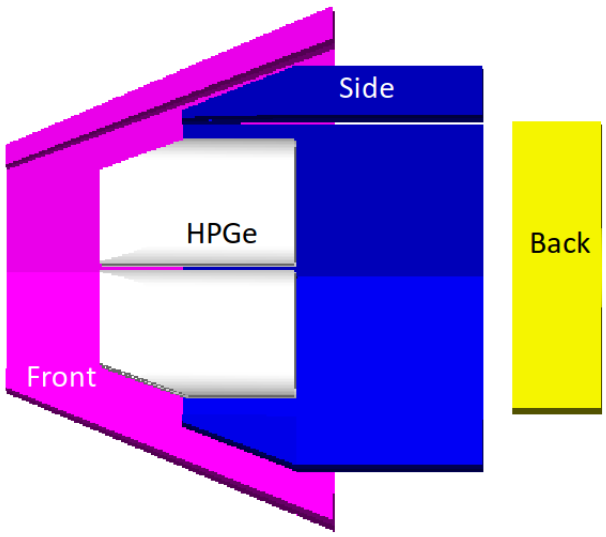

Figure 5.5: The Compton-suppression shield, shown in relation to the HPGe clover. (GEANT4 view)

The back shields are made of two square optical segments of CsI, as shown in Figure 5.6. Each CsI segment will be housed in a separate casing with a thickness of 3.7 cm. To accommodate the cold finger from the liquid nitrogen dewar of the HPGe detector, the inner corner of each back suppressor square will be cut. This optical segmentation allows for gamma-ray position sensitivity and the capability to suppress specific regions of the HPGe detector by using different regions of the suppression shield. The implementation of segment-specific suppression, based on which suppression shield elements were hit, will be

further discussed in Chapter 7.

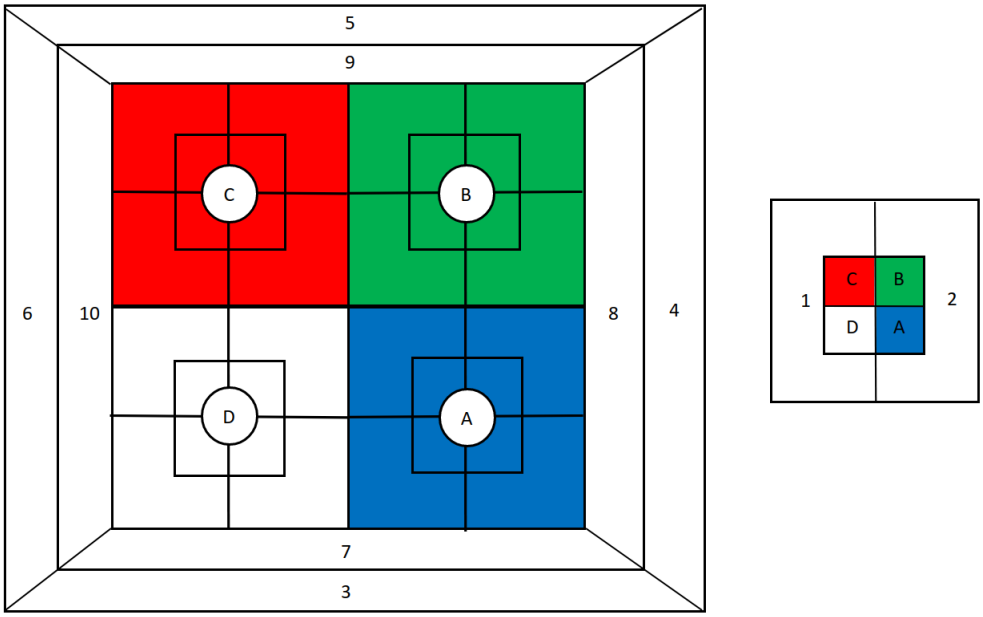

Figure 5.6: Schematic of the relationships between the suppressor segments and the crystals in a clover. The back suppressors are positioned to the side (numbered as 1 and 2), while the front (numbered from 3-6) and side (numbered from 7-10) suppressors are depicted at the same level as the crystals.

5.3 Measuring and optimising the performance of ELIADE detector

The ELIADE Compton-suppression shield prototype was procured from Canberra-Packard by ELI-NP. With the construction of a single-detector test stand where both prototypes could be mounted together (Figure 5.7), performance measurements of the combined system became feasible. While the primary aim of these tests was to verify the correct functioning of the devices, they also offered an opportunity to assess the capabilities of the combined devices and aid in generating accurate predictions of ELIADE's performance. Having reliable predictions of the array's performance under various experimental conditions is

crucial for effective planning of future experiments.

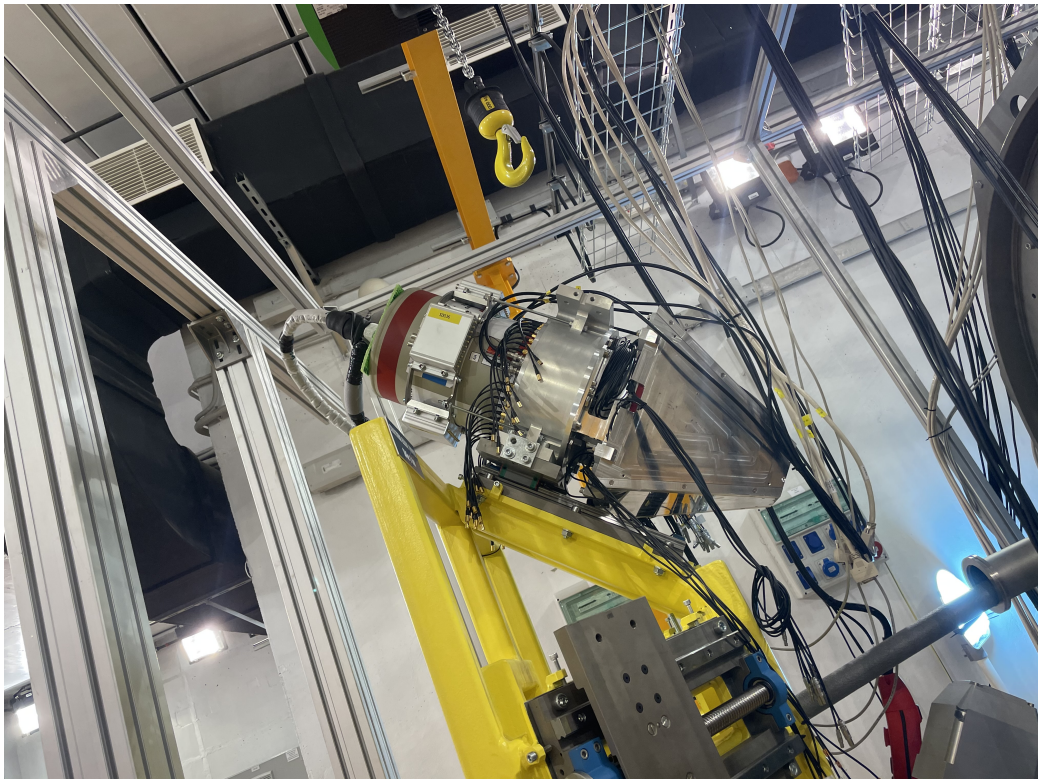

Figure 5.7: The ELIADE prototype test stand, photograph with detector and suppressor mounted, fully instrumented.

Calibration sources were utilised for initial tests, but they provided limited information, especially for higher gamma-ray multiplicities. To address this, a Plutonium-Beryllium neutron source was also used for higher energy tests, considering that predicting the array's performance for certain analysis methods involves more complexities than simply scaling results from one detector to multiple detectors.

Throughout the development of the ELIADE array, predictions have played a critical role, even when physical references were unavailable. Initially, simulations were the primary means of predicting the array's capabilities, but uncertainties arose due to the lack of suitable references for comparison. Thus, one of the main objectives of this study is to

create accurate predictions for experiments with ELIADE. To achieve this, the simulation was significantly improved by comparing it with data from the prototype.

Accurate simulations have benefits beyond performance predictions. Another goal of this work was the development of optimised energy and multiplicity-dependent analysis methods, as detailed in chapter 7. The simulation's speed and versatility allowed for practical exploration of these methods and determination of their effectiveness across various combinations of gamma-ray energy and multiplicity.

Chapter 6

GEANT4 simulation

The initial versions of the simulation used in this study were primarily developed as tools to aid in the design of the Compton-suppression shield. The geometry of the ELIADE clover detectors was accurately simulated based on the design drawings, and various configurations of the Compton-suppression shield were tested. Moreover, the simulation was utilised to determine the optimal position of the lateral segmentation line for the ELIADE HPGe clovers and to conduct preliminary investigations into the development of algorithms for first-interaction position determination. The simulation proved valuable for all these purposes. However, its accuracy could not be adequately validated against a closely related physical reference until the prototype detectors were designed and constructed.

6.1 Principle of GEANT4

The ELIADE simulation is fundamentally a Monte Carlo simulation that involves the interactions of gamma rays with matter, utilising the GEANT4 simulation toolkit [Ago03]. It employs established models of electromagnetic processes to generate paths for gamma rays, which are "emitted" from a user-defined point in a three-dimensional "environment" and travel in randomised directions.

GEANT4 (GEometry ANd Tracking 4) is a powerful toolkit that employs extensive Monte-Carlo (MC) methods to simulate particle tracks in various materials. Developed through a global collaboration of scientists, GEANT4 is written in object-oriented C++ programming

language. Its applications span a wide range of fields, including particle physics, nuclear physics, accelerator design, space engineering, and medical physics [Ago03]. The simulation of a complex radiation detector like ELIADE can be achieved by constructing it from simpler geometrical shapes (cylinders, cubes, cones, spheres, etc.) and defining the properties of the constituent materials of these objects. Additionally, users can define the energies, emission locations, and emission directions of the particles to be considered in the simulation. For this study, the ELIADE simulation was carried out using GEANT4 version 10.06 (with patch 03).

The materials used to construct the components in the ELIADE detector simulation were determined based on the atomic numbers and average atomic masses of the constituent elements. For solids and liquids, the materials' definitions included their bulk densities, while for gases, temperature and pressure values were also required. In the case of mixed materials, the definitions needed values and percentages for each constituent element. All the standard elements in this simulation including the materials for the Compton shields (BGO and CsI), for consistency, are taken from the GEANT4 database. For the three main mixed materials, details can be seen in Table 6.1.

Materials	**Components**
Stainless Steel	C 0.1%, Si 0.7%, Cr 18%, Mn 1%, Fe 71.2 Ni 9%
DURAL support	Al 94%, Cu 4%, Mg 1%, Mn 1%
Densimet	W 97%, Ni 1.5%, Fe 1.5%

Table 6.1: Table of components of mixed materials used in simulation

The simulation included only electromagnetic processes, and it defined photons, electrons, and positrons as the particles involved. Gamma rays were assigned the following potential physical processes: photoelectric absorption, Compton scattering, and pair production. The interaction probabilities for these processes, based on gamma ray energies and material properties, were calculated using the built-in models of GEANT4 [Ago03]. To ensure the simulation's efficiency, a cut-off was applied to prevent an excessive number of low-energy electrons generated from the cascade of electron ionisations in High-Purity Germanium detection. Low-energy particles were assumed to be fully absorbed by the material. To account for the short mean ranges of low-energy particles, a range cut was implemented. For

all particles, including electrons generated by ionisation or low-energy photons produced by Bremsstrahlung, a mean range cut of 1 mm was applied. Consequently, only a few ionisation interactions were typically simulated before considering the remaining energy to be absorbed.

The physics lists used in this work were G4DecayPhysics, G4RadioactiveDecayPhysics, G4EmStandardPhysics and Neuron HP. Which are in general use of interactions on low energy simulations.

In GEANT4, a particle gun was utilised to emit gamma rays of specific energies from a position representing the center of the ELIADE array. The angular direction of the emitted particles was randomised using two uniformly distributed random numbers, rand1 and rand2, generated from the drand48() function, ranging from 0 to 1.

Within the GEANT4 framework, intricate geometries are constructed by assembling basic shapes like cubes, cones, cylinders, and spheres, or their combinations. Each shape is assigned specific material properties. To create a complete detector geometry or experimental setup, an "experimental wall" is defined, acting as a large cube made of air in the ELIADE simulation. Subsequently, all components of the detector are incorporated by positioning them within this simulated mother wall, utilising its three-dimensional reference system. See Figure 6.1.

Instead of directly creating histograms and spectra from the simulation, a concise version of the total information generated was saved in binary format to data files. Each event written to the data file contained the total energy deposited by gamma-rays in each of the HPGe crystals and in each segment of the suppression shield. Moreover, for each HPGe crystal, the three-dimensional position of each gamma-ray interaction relative to the middle of the face of the clover, along with the resulting energy of the gamma ray, were recorded. This information was sufficient to determine the deposited energies in each crystal of the HPGe clover and to identify which suppressor and crystal segments were affected in each detector. By doing this, the need to process unnecessary information, such as energy depositions in inactive parts of the detector or tracking information for individual electrons in the crystals, was eliminated. Only the resulting total energy depositions that are essential for analysis were retained.

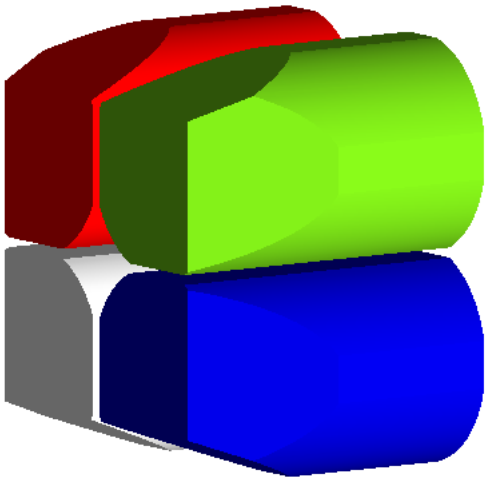

Figure 6.1: The simulation of the ELIADE detector assembling in many smaller shapes. (GEANT4 view)

The primary advantage of saving the condensed information to data files was the ability to reuse this information for testing different analysis procedures. This proved crucial for both the refinements discussed in this chapter and the comparisons of optimisation schemes discussed in chapter 7. Generating the simulated data was a time-consuming process, often requiring days or weeks of computing time to generate the data sets used. By separating the data generation from the data analysis, the more time-intensive part of the process was performed fewer times, allowing for an increased number of refinements to be made to the analysis procedures. This approach significantly improved the efficiency and effectiveness of the overall simulation and analysis process.

6.2 Model of ELIADE clover detector

In chapter 4.6, specific measurements were provided for the ELIADE HPGe clover. These measurements correspond to the production detectors that will make up the ELIADE array, although the crystal geometry for the prototype was slightly different. Each cylindrical crystal used to construct the HPGe clover of the prototype initially had a diameter of 60 mm. However, they were cut on the inner surfaces to a depth of 26 mm from the central axis (instead of 27.2 mm) and 28.5 mm on the outer sides (instead of 29.3 mm). Consequently,

the forward taper ends at a depth of 30 mm instead of 36.2 mm to maintain the taper angle of 22.5 °. Nevertheless, the length, inter-crystal separation, and inner core measurements remain the same.

Another significant distinction between the HPGe clovers lies in the location of the lateral depth segmentation line. For the prototype, it was set at a depth of 30 mm, whereas the production detectors will have it at a depth of 31 mm. To ensure accurate comparison to the real data from the prototype and reliable predictions using the simulation, the slightly different clover design was incorporated into the prototype simulation. The assumption was that once the simulation of the prototype detector was refined based on the prototype detector data, changing the geometry to that of the production crystals would not compromise the predictive capabilities of the simulation.

6.3 Model of Compton suppressors

A small difference became apparent while the tests of the prototype suppression shields were being performed. The side shields, housed in a common aluminum casing, were not designed to have diagonal boundaries between physical segments, and the central segmentation lines were shifted in order to use equal-size BGO crystals. This design flaw has been corrected in the production suppression shields, and it had very little impact on the peak-to-total ratio or efficiency of the simulated prototype. However, this more accurate prototype design was incorporated in order to allow for better comparison with the real prototype results. A comparison of the design that will be used for the production suppression shields and the segment design of the prototype side shields can be seen in Figure 6.2.

Another distinction between the prototype and production models of the suppression shields is the variation in the width of the dense metal collimators on the front edges of the front shields. This difference in width caused an issue as the collimators were too large to allow the front shields to be properly close-packed, necessitating a slight pulling back of the shields. Additionally, the aluminum casing near the back of the front shields did not close-pack properly when the collimators were removed. Since these factors could potentially affect the probability of suppressing scattered events and, consequently, impact the peak-to-total ratio values, back-shifts were introduced to adjust the positions of the

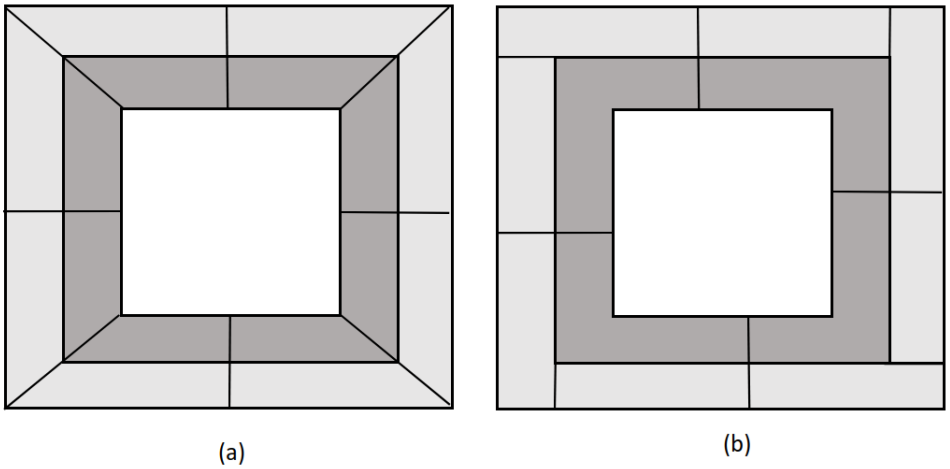

Figure 6.2: A rear view comparison of the shapes of the optical segments in the side shields: (a) the design for the production models; (b) the design of the prototype side shields.

front shields for both detector back variations. A 1 cm shift was applied to match the actual prototype collimator size. To assess the influence of these back-shifts on the counts and FWHM, a simulation was conducted, and further details can be found in Table 6.2.

Sources	**Designed**	**Prototype**	**Difference**
Counts (^{60}Co)	240000±12000	230000±14000	0.044%
FWHM (1.173MeV)	2.628	2.635	0.257%
FWHM (1.332MeV)	2.721	2.704	0.649%
Counts (15MeV)	7100000±350000	7100000±330000	0.097%
FWHM (15MeV)	9.830	9.785	0.457%
Counts (20MeV)	7300000±400000	7300000±360000	0.006%
FWHM (20MeV)	12.466	12.425	0.329%

Table 6.2: The influence of back-shifts showed in simulation, with an incident of 10^7 gamma rays.

6.4 Energy resolutions

As discussed in chapter 2.5.3, HPGe detectors have an inherent energy resolution. However, the contributing effects that lead to this resolution cannot be directly modeled by GEANT4. Consequently, the energy spectra generated in the simulation are idealised, with all energies known to the precision of the data output. To enable a visual comparison between the simulated and experimental spectra, a resolution function was applied to the spectra of the simulated prototype. This uncertainty was applied on an event-by-event basis for each of the four crystals, using the measurements of photopeak resolution made in chapter 4.

6.5 Validation

With the purchase of the ELIADE detectors and one prototype set of Compton suppression shield, after the detector annealing work, some separate source measurements can be done. By simulation the exact experimental conditions under which data were collected with the prototype detector and suppression shield pieces, the accuracy of the simulation could be tested.

For each source, 10 million events with emission into 4π radians were simulated to generate spectra for comparison with the experiment and to calculate peak-to-total ratios. Regarding gamma-ray emission, each source had to be simulated slightly differently. For ^{137}Cs, a single gamma source, 10 million gamma rays of 661 keV were generated. For ^{60}Co, a multiplicity-2 source, 10 million events consisting of both a 1173 keV and a 1332 keV gamma ray, emitted in uncorrelated directions, were simulated. Similarly, for ^{22}Na, 10 million events with gamma rays of 511 keV and 1247 keV were generated. The comparisons between the simulated and experimental spectra are presented in Figures 6.3, 6.4 and 6.5.

The normalization factor used in the comparison was based on the peak area of photopeaks. For sources like ^{60}Co and ^{22}Na, which have more than one peak, the normalization was based

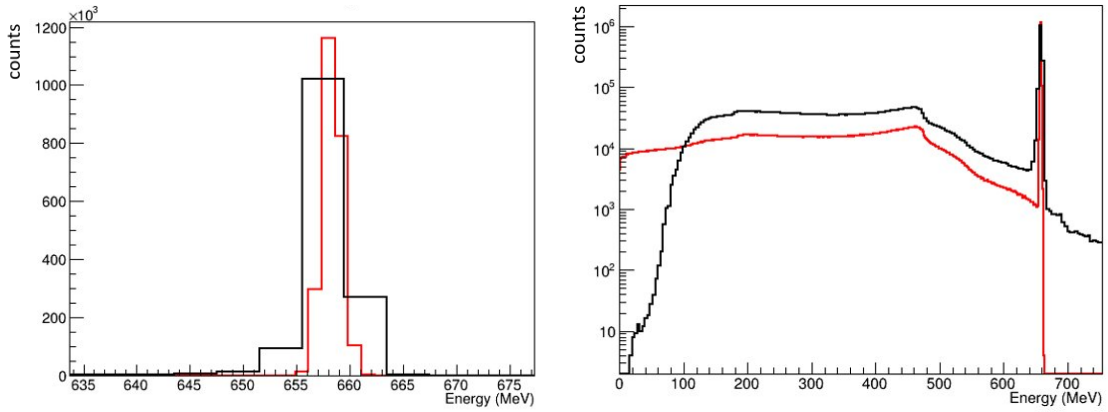

(a) (b)

Figure 6.3: Comparison between the measured (black) and simulated (red) spectra for the ^{137}Cs test source. (a) compares the normalised photopeak from the real and simulated data; (b) compares the spectra for the crystal spectrum.

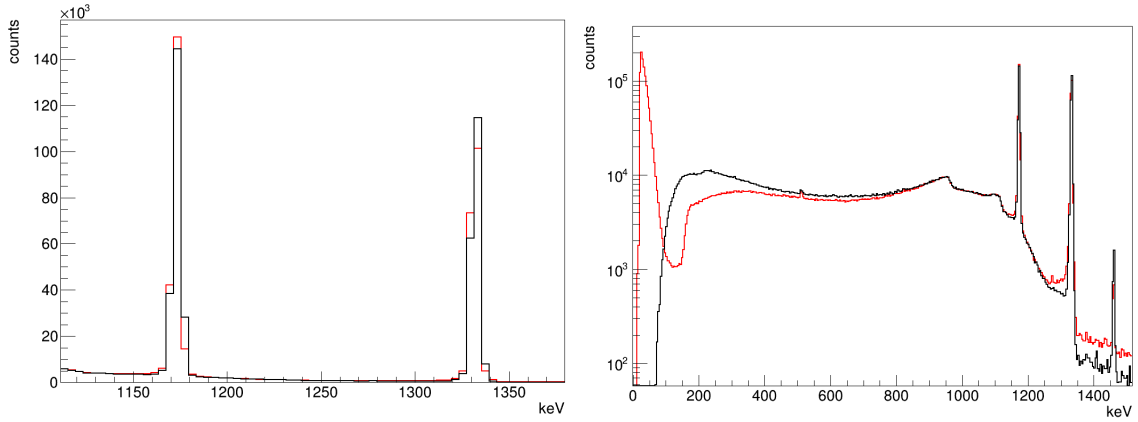

(a) (b)

Figure 6.4: Comparison between the measured (black) and simulated (red) spectra for the ^{60}Co test source. (a) compares the normalised photopeaks from the real and simulated data; (b) compares the spectra for the crystal spectrum, the lower energy from simulation is due to the set of a threshold which does not influence in this measurement.

on the lowest-energy photopeak. Despite this, the higher-energy peaks in the simulation matched their experimentally determined counterparts exceptionally well. Additionally, there was a close agreement between the overall shape of the background spectra in the

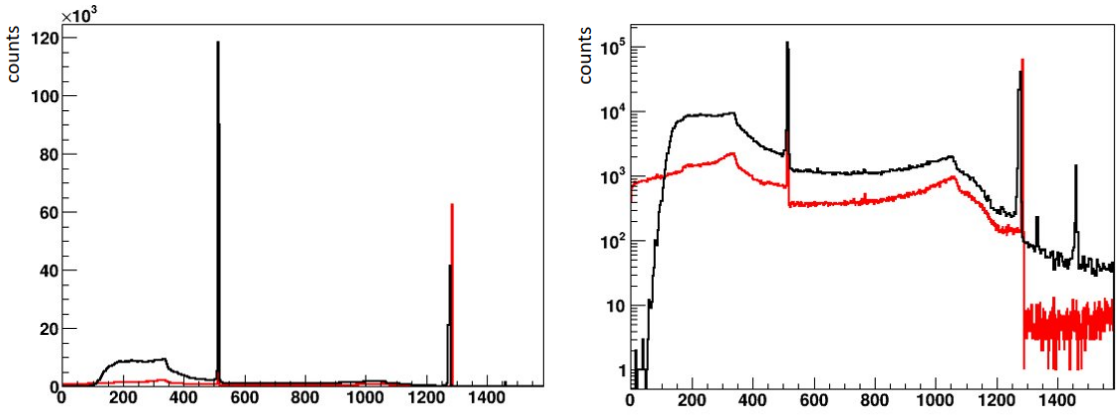

(a) (b)

Figure 6.5: Comparison between the measured (black) and simulated (red) spectra for the ^{22}Na test source. (a) compares the normalised photopeaks from the real and simulated data; the shift on 1247 keV peak is due to the calibration of energy when the simulated result is normalised , also the simulated higher 1247 keV peak is due to different setting of the abundance/annihilation ratio. The influence is negligible for now since the analysis is based on single peaks which can be varied. However, this should be improved for whole source test in future work. (b) compares the spectra for the crystal spectrum.

simulation and the experiment.

A minor difference was observed in the number of low-energy counts in the background region. Below the lowest-energy Compton edges, the simulation consistently predicted a slightly higher number of counts (except for the ^{60}Co source, influenced by the threshold setting), although the difference was not significant. The discrepancy around the Compton edge was due to the resolution function used during the generation of simulated spectra for the comparisons. As gamma rays backscatter out of the detector, most of these events occur near the front of the detector where the electric fields are the weakest, leading to poorer energy resolutions in those regions [Scr+05]. This effect could not be accounted for since the resolution of front-only events is based on all events in the first 2 cm of the crystals.

Table 6.3 summarised the compared peak-to-total ratios. The resulting peak-to-total values from simulation varies by a small amount (0.4-2.8%), the main cause of these discrepancies is the difference in the number of low-energy counts, such as the subtraction of

x-rays from the fluorescence.

Sources	Measured	Simulation
^{137}Cs	26.7(3)%	26.3%
^{60}Co	16.2(8)%	18.0%
^{22}Na	27.2(3)%	24.4%

Table 6.3: Comparison between experimentally determined and simulated peak-to-total ratios (P/T) for test sources.

A simulation of the efficiency curves was also carried out. 10 million single gamma rays with energies from 1 to 10 MeV were simulated and sorted in order to determine efficiency values (see Figure 6.6).

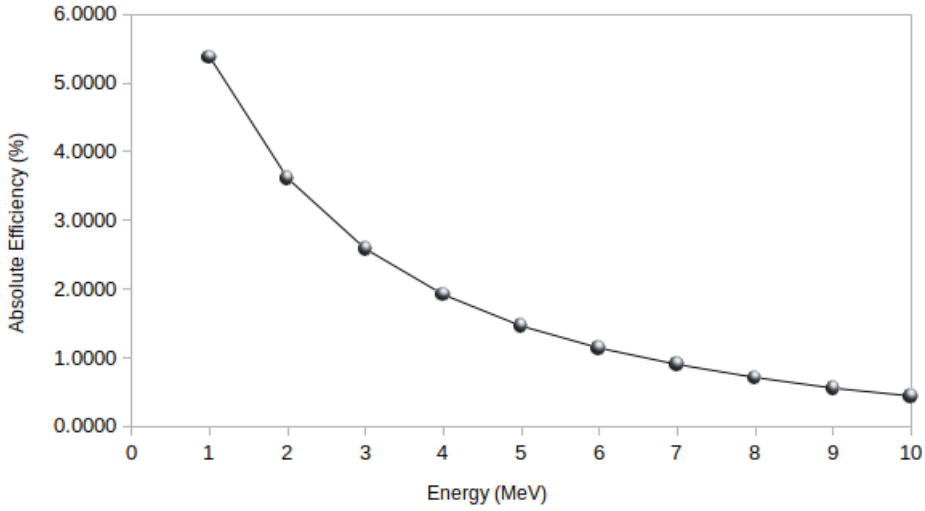

Figure 6.6: Simulated efficiency values in an energy range from 1-10 MeV

A validation of Compton suppressor detectors in efficiency is also finished. The source used in the anti-Compton validation measurements is ^{137}Cs, placed in a distance of 5 cm from the BGO detector and 10 cm from CsI back catcher, all running for 5 mins. Table 6.4 shows the validation results. The efficiency was calculated as the ratio between the number

of detected photon within any sensitive cube and the number of emitted photons.

Detector	**Measured**	**Simulated**
BGO front shield	5.1(2)%	5.3%
BGO side shield	5.2(2)%	4.9%
CsI back catcher	1.9(1)%	1.2%

Table 6.4: Table of anti-Compton shielding validation efficiency results

From this figures and table, it is clear that the agreement is good for the clover detector and anti-Compton shielding implanted in GEANT4 simulation.

Chapter 7

Optimisation schemes

The impressive detection efficiency of the ELIADE array, a key design feature, presents a challenge when investigating high-multiplicity events, particularly in the context of high-spin studies in nuclear structure. The enhanced efficiency, stemming from the array's large crystal size and their central positioning, results in a notable probability of multiple gamma rays hit the same detector. This scenario can lead to complications, where even if one gamma ray fully deposits its energy, the corresponding event's energy is subtracted from the photopeak. Consequently, both photopeak efficiency and peak-to-total ratio decreases as the probability of multiple gamma-ray energy depositions in a crystal rises. Moreover, instances where one gamma ray hits a HPGe crystal while another hits a suppressor segment of the same detector can result in false suppression, further reducing detection efficiency due to the mistaken rejection of real full-energy depositions.

This chapter delves into the exploration of analysis techniques aimed at mitigating the consequences of high-multiplicity events. The focus is on reducing the adverse effects on peak-to-total ratio and detection efficiency. The chapter investigates the performance of these techniques using simulation, with the aim of optimising ELIADE's sensitivity for different experimental conditions. The ultimate goal is to enhance the achievable peak-to-total ratio and absolute efficiency.

The two optimisation methods will be referred to as: *Summing schemes*, to optimise crystal and detector summing, *suppression schemes*, to minimise false suppression. Employing these methods will enhance the sensitivity of ELIADE experiments in the future.

7.1 Summing schemes

As discussed in chapter 4, the main purpose of using segmented clover germanium detectors is to obtain high detector efficiency without diminishing the energy resolution and timing characteristics. When a gamma-ray hits on a segmented clover detector, it may interact with one of the segments/crystals and either be absorbed or scattered, causing partial absorption of energy which contributes to the background noise of its spectrum. In ELIADE detectors, segments are closely packed together with only rear-side support, which minimises the amount of material surrounding them. This leads to a result that the scattered gamma-ray can pass into an adjacent segment without energy loss from the material between them and interact again. There is also a chance that the scattered gamma-ray may escape the detector. As the energy goes up, the probability of secondary scatterings increases. Single event and multiple events are defined by the number of segments which interacted [FAB+92]. Multiple events are also time correlated events, by adding up these events, information from scattered gamma-rays that remain within the detector can be added back to the full energy peak, recovering the energy of the incident gamma-ray that was scattered with partial energy absorption. Therefore, the clover detector can reconstruct events involving scattered gamma-rays that are detected, and it can be operated in two modes: single crystal mode and add-back mode [RKs12].

As discussed in chapter 4, the add-back mode has been used to sum energy contributions in multiple HPGe crystals of the same detector, and detector summing was shown to produce an increase in photopeak area as well. For lower energies, the optimising results of add-back mode is limited, however, as the energy increases, the influence of add-back to the peak-to-total ratio becomes significant, as the probability of multiple gamma-rays interacting becomes non-zero, see Figure 7.1.

Though these trends can easily be understood intuitively, the specific multiplicities at which detector summing, crystal summing or lack of summing are best are not obvious. In addition, there will be a significant energy dependence to these trends. In order to examine these trends, and to compare the utility of different crystal and detector summing, three

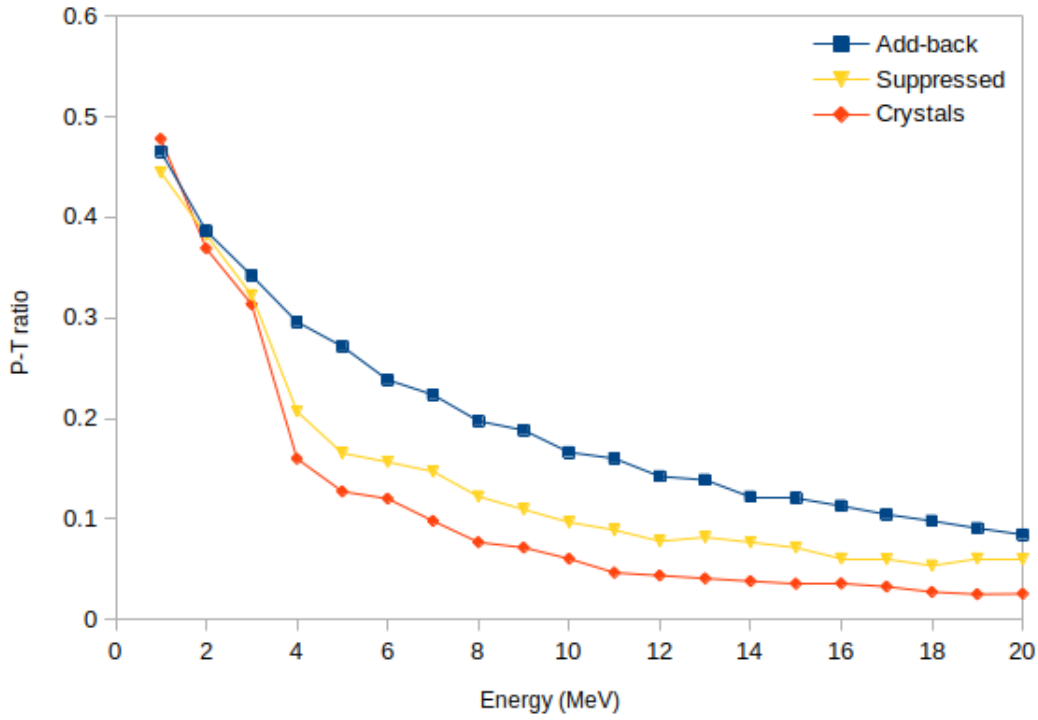

Figure 7.1: Simulated peak-to-total ratios as a function of gamma-ray energy for different analysis modes.

add-back schemes were tested and compared for a range of gamma-ray energies. The drops on the suppressed and crystals modes between 2 and 4 MeV is likely to be where the effect of reaction circles dominates.

Add-back Schemes

Two of the add-back schemes to be investigated have already been discussed. These are the "Crystals" and "add-back" analysis modes explored with both the prototype detector, and with the simulation of the ELIADE detector.

In addition to these approaches, the feasibility of an intermediate method, known as "Segments Add-back," was investigated. This method utilises the segmentation of the ELIADE crystals by analyzing the segment hit patterns within the crystals. For each event,

a determination is made whether the energies in each crystal should be individually added to the energy spectrum (similar to the Crystals mode) or summed together (similar to the Add-back mode), based on the observed segment hit patterns.

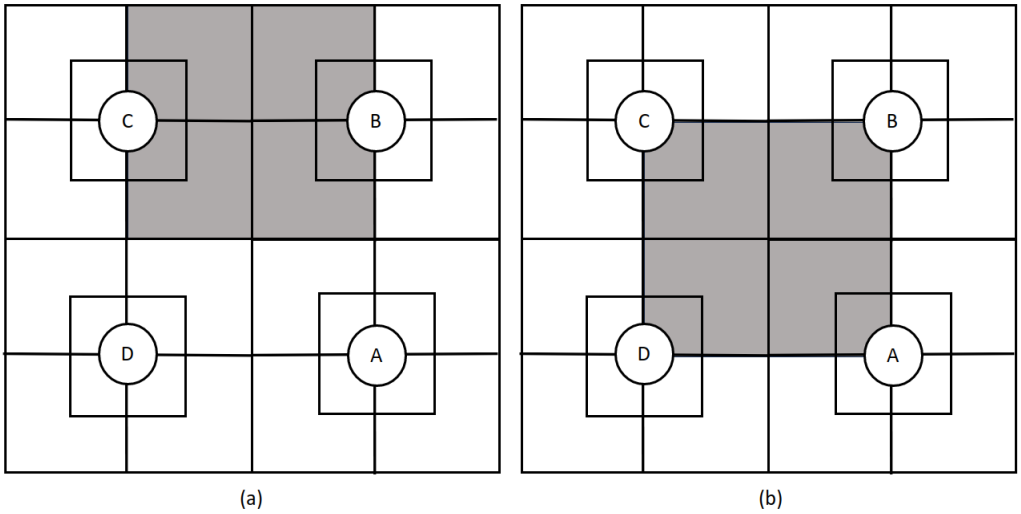

Figure 7.2: The segments within which interactions need to take place for the summation of crystal energies in segments add-back mode (a) shows the segments that may be hit for a two crystal interaction to be added, (b) shows the same for events with three or more crystals with interactions.

The Segments Add-back algorithm varies based on the number of crystals hit (Folds) and operates as follows:

- If a single crystal is hit, its energy is directly used.
- If only two crystals are hit:
  - they are diagonally separated, their energies are used individually.
  - they are adjacent, their hit patterns are examined. If each crystal has only the four segments adjacent to the other crystal hit, their energies are summed. Otherwise, the energies of the crystals are used separately.

- If three or four crystals are hit, the hit patterns of each crystal are checked. If both inner segments in each crystal are the only segments hit, their energies are added together. Otherwise, the energies of the crystals are used separately.

Figure 7.2 shows the segments that need to be hit in order for the energy summing of the crystals to occur in the case of two crystals and three or four crystals.

7.2 Suppression schemes

For events with low energies, like those of standard sources simulated in chapter 4, the approach of suppressing all coincidences between a suppression shield segment and an HPGe crystal produced the highest peak-to-total ratio. This was due to the reduction in the number of background counts achieved through this method. However, as the energy of the events increases, there arises a chance that full-energy depositions within a clover might be suppressed due to another gamma-ray interaction with a portion of the suppression shield. This false suppression leads to a decrease in the detection efficiency as the photopeak counts are suppressed. The probability of this scenario can be mitigated through the use of a collimator, although at higher energies, there's the possibility of gamma rays scattering from the collimator into the clover.

The concept of false suppression is depicted in Figure 7.3. The hit pattern linked to gamma-ray interactions, as outlined in both 7.3a and 7.3b, would be identical. However, employing the suppression based on the crystal-suppressor coincidence for this event would yield different results. In case (a), suppressing this event would remove a count that contributes to the background, whereas in case (b), it would result in the removal of a full-energy deposition count from the photopeak.

Figure 7.4 shows the coincidence pattern that illustrates the importance of the ten suppressor segments for the suppression of single-crystal events, a method was devised to mitigate the amount of false suppression in higher crystals events. This pattern indicates a clear result: there is a considerably higher probability of a nearby suppressor segment (front suppressors) vetoing an interaction in a crystal, compared to a suppressor located further away (back suppressors). Given the extensive segmentation of the ELIADE suppression

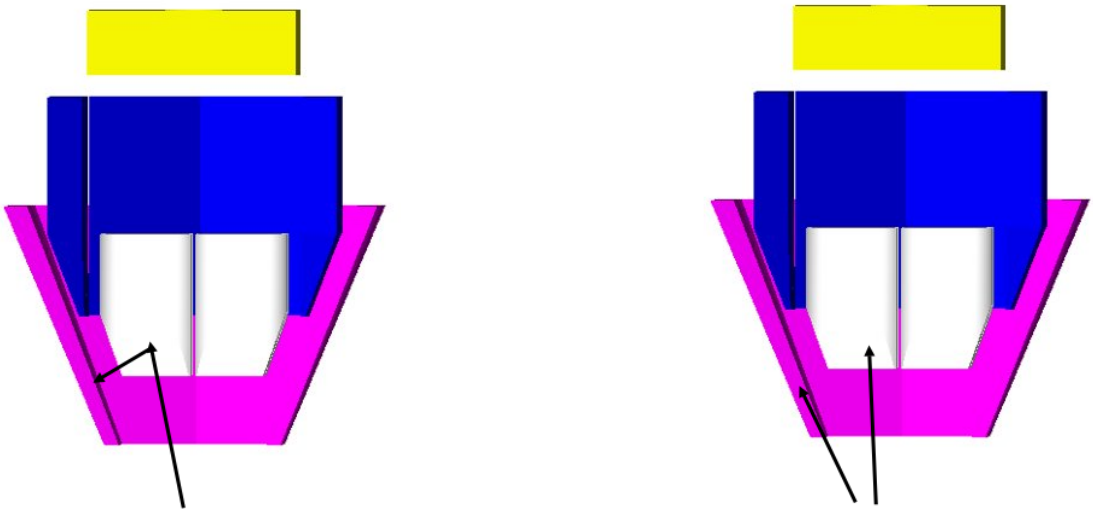

(a) (b)

Figure 7.3: The problem associated with the suppression of higher energy events. In case (a), suppressing this event would remove a count that contributes to the background, whereas in case (b), it would result in the removal of a full-energy deposition count from the photopeak. Magenta is the front BGO shield, blue is the side BGO shield, yellow is the back CsI shield and gray is the HPGe crystals.

shield, it became possible to explore suppression schemes where not every segment of the shield would veto an interaction in a specific HPGe crystal. This implies that, for scenarios in which it is more probable that an interaction in a suppressor segment is due to a second gamma ray rather than Compton scattering, the suppressor interaction can be disregared, and the energy in the HPGe crystal can be used.

It is essential to acknowledge that exploring every potential suppression scheme is unlikely. With an ELIADE detector having ten segments that can be either active or inactive for suppression in a given crystal interaction, designing a scheme comes down to making ten on/off decisions. However, this leads to a big number of possible combinations, which is too many to be systematically investigated (Figure 7.5). Let along in simulation, an extension of twenty segments Compton suppressor was also implanted for the initial design of ELIADE array.

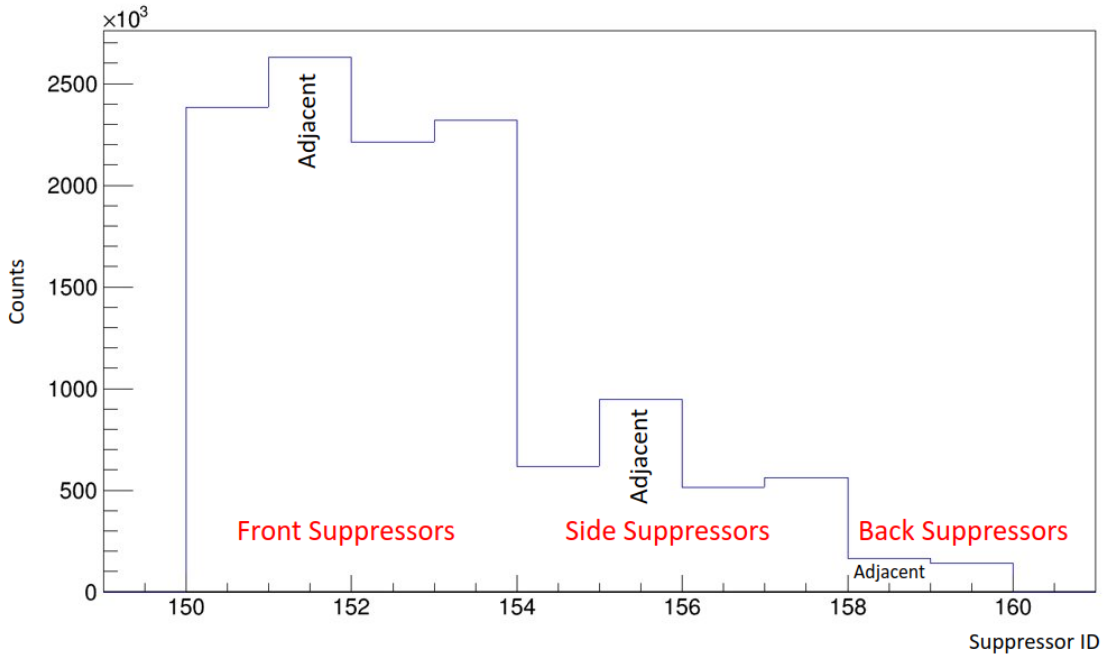

Figure 7.4: Histogram of hits in the suppressor segments due to Compton scattered gamma rays from one crystal for the simulated detector. These events involve a single crystal (crystal D) being hit along with at least one suppressor segment. The histograms illustrate the count of hits for each suppressor, categorised into front, side, and back suppressors. The number of counts decreases as the distance to the crystal. The labelled "Adjacent" is the suppressor segments that are adjacent to crystal D which also have significantly higher counts than their neighbours.

A significant constraint on the number of interested schemes is the improbability of discovering a scheme in which distant segments suppress events in a crystal while closer ones do not. The coincidence patterns between the suppressors and each crystal, as illustrated in Figure 7.4, lend support to this idea. These figures clearly demonstrate that the "Adjacent" suppressors to a crystal encounter the majority of scattered events from that crystal. Conversely, the farther or opposing segments experience progressively fewer counts of scattered events.

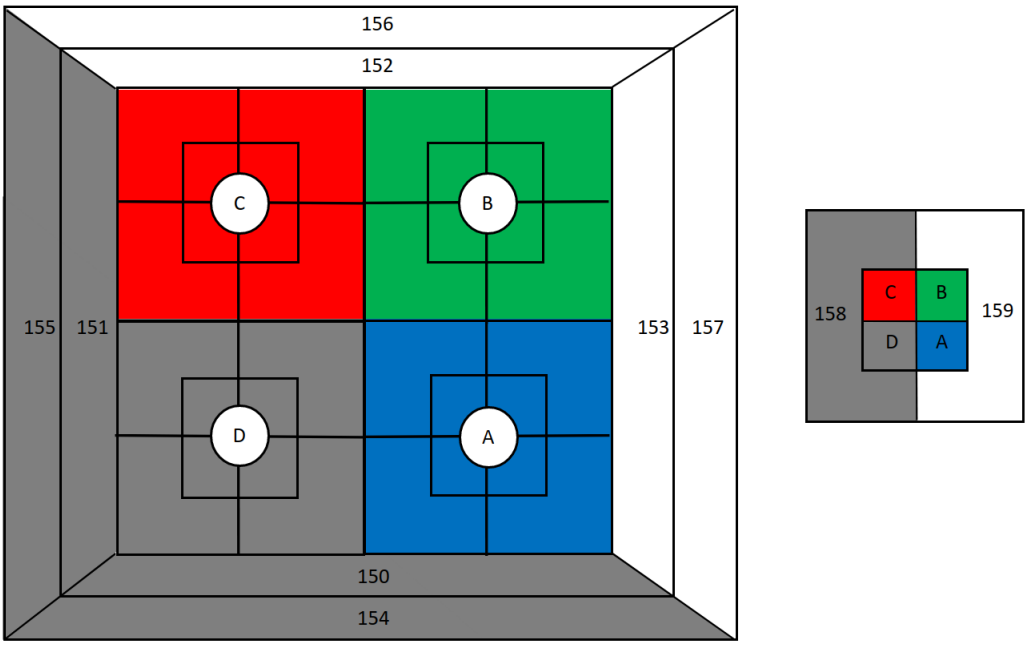

Figure 7.5: Numbered suppressor segments and selected crystal D shows the adjacent suppressor segments. The back suppressors are positioned to the side (numbered as 1 and 2), while the front (numbered from 3-6) and side (numbered from 7-10) suppressors are depicted at the same level as the crystals.

7.3 Results and discussion

At each of the gamma-ray energies and folds, the peak-to-total ratio and absolute efficiency were determined from simulation for all combinations of the summing and suppression schemes.

Summing Schemes

Figure 7.6 shows the add-back factors of ^{137}Cs, ^{60}Co source and 9 MeV gamma beam source in segments add-back schemes. Fold is the number of crystals hit, since the selection of crystal segments is included in the segments add-back algorithm, the number of folds is up to 4. From this figure, it can be seen that for the standard source, the influence of multiple folds is limited. This is due to the small probability of multiple crystal events occuring in the low energy range. However, it shows a significant increasing of add-back factor for the

9 MeV gamma beam source since it is much more likely to have the 4 crystals events in higher energies. Thus, it appears that segments add-back scheme has effectively served its intended purpose as an intermediate scheme in this context, especially for higher energies.

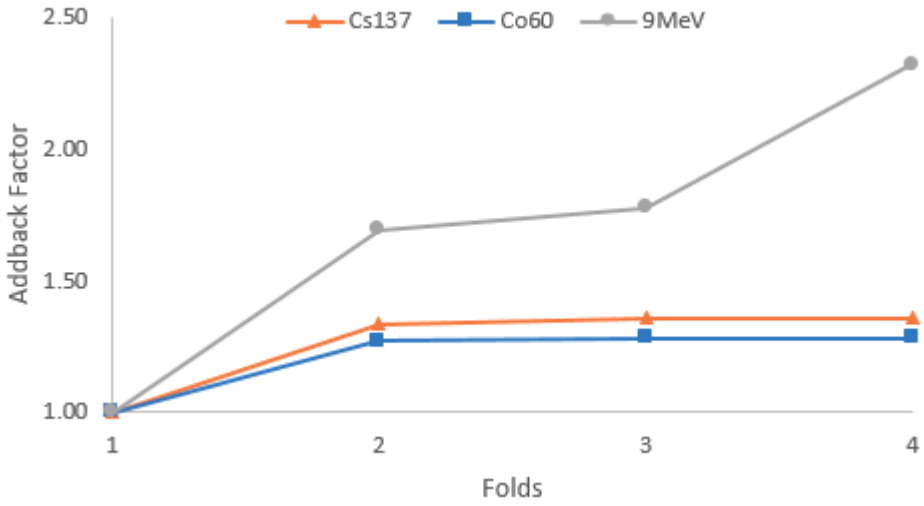

Figure 7.6: Peak-to-total ratios for different energies using Segments Add-back Scheme.

Suppression Schemes

In the suppression scheme, two key features are considered, the distance of Compton suppression shields to the HPGe detector and the segmentation of suppressors. Figure 7.7 shows the peak-to-total ratio in different Compton rejection modes, from which one can be seen the influence in each of the suppressors to the spectra. In this figure, AC, FC, SC and BC represents the active segment of the whole Compton suppressor, Front shield only, Side shield only, and Back shield only mode. In each mode, the event will be rejected only when it hit the active suppressor and at least one HPGe crystal. It is clearly that the whole Compton suppression mode is the best scheme for both lower and higher energies. But it also shows a slightly bigger difference on the back shield rejection mode for 9 MeV, this is due to the larger number of counts in the back CsI detector.

Other than different parts of Compton shields, taking into account the segmentation of

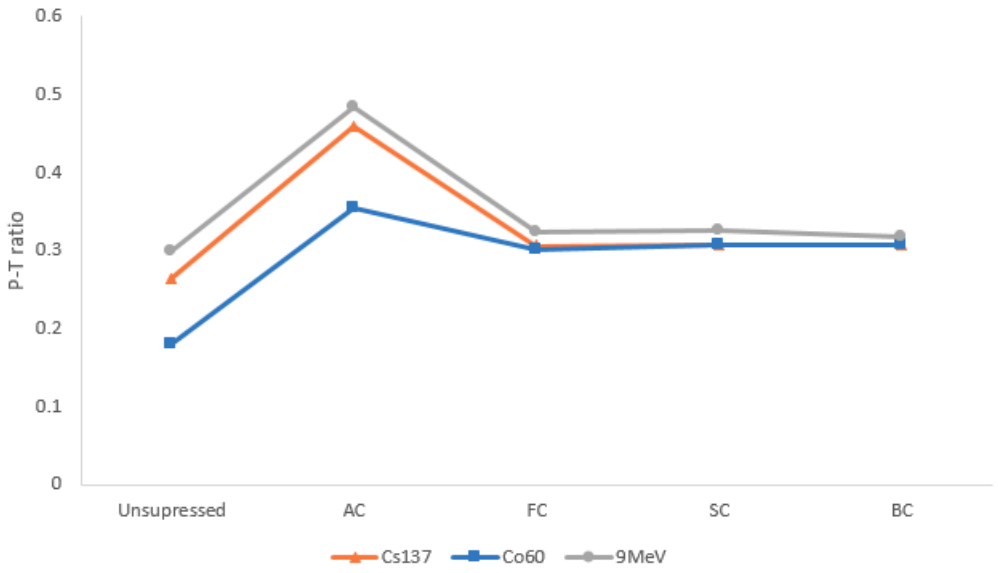

Figure 7.7: Peak-to-total ratios in different active suppressor rejection mode.

suppressors may also improve the quality of spectrum. Figure 7.8 shows the results of peak-to-total ratios in Unsuppressed mode, Suppressed mode and Segmented-suppressed mode. Unsuppressed mode is obviously the initial spectrum without Compton suppression, Suppressed mode is the non-selection event rejection mode which reject all the events that hit on both suppressor and crystal. Segmented-suppressed mode is a selective rejection mode as discussed before, only the adjacent suppressor and crystal hit events will be remove from the spectrum. In this figure, the Segmented-suppressed rejection mode shows less peak-to-total ratios on the ^{137}Cs and ^{60}Co source, this is because in the lower energy case, the chance of two or more crystal events is less, therefore the counts on the further suppressor is more likely to be seen as a secondary gamma ray from a neighboured suppressor and will not be rejected, which will cause the slightly increased the background counts. However, this problem is become less influenced as the energy goes up. In 9 MeV, the Segmented-suppressed rejection mode improves the peak-to-total ratio significantly.

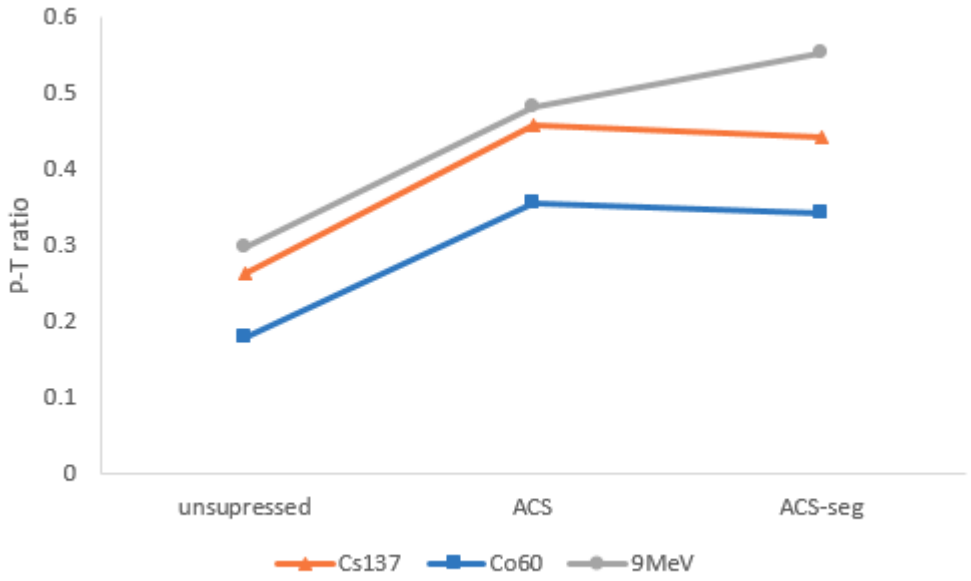

Figure 7.8: Peak-to-total ratios in unsuppressed mode, suppressed mode and segmented-suppressed mode.

7.4 Summary

In this chapter, a thorough exploration was conducted to optimise the sensitivity of ELIADE experiments under various experimental conditions. The focus was on addressing challenges associated with higher energy events when employing a high-efficiency detector. In each instance, the ELIADE simulation established in chapter 6 was employed to assess different summing and suppression modes. The objective of these assessments was to identify the most effective configurations for different scenarios involving gamma-ray energy and multiple crystal events.

While the energies and multiple crystal scenarios examined were somewhat idealised and not directly indicative of any specific experiment, they encompassed a diverse range, leading to the revelation of several overarching trends. The intention is that the outcomes derived from this comprehensive study of summing and suppression schemes can aid ELIADE experiments in approximating anticipated values for peak-to-total ratios and absolute efficiency

pertinent to their real-world experiments. Furthermore, the techniques employed here can serve as a foundation for evaluating schemes under more realistic conditions, specific to experiments utilising ELIADE.

Chapter 8

Conclusions and future directions

8.1 Conclusions

To assess the operational efficiency of the prototype ELIADE detector along with its corresponding Compton-suppression shield, conventional nuclear physics electronics were employed for instrumentation. Standard gamma-ray sources were utilised to ascertain peak-to-total ratios (P/T) for distinct ELIADE configurations, as well as to derive relative efficiency curves. The measured peak widths stemming from these test sources served to formulate energy resolution functions, while also revealing differences in energy resolution between the front and back sections of the HPGe clover.

Based on the combined performance measurements of the prototype components, adjustments were made to simulations of the ELIADE prototype detector and suppression shield. A meticulous comparison was undertaken, evaluating the P/T values and efficiencies against the measured data. Several of the refinements were of a general nature, permitting their application to simulations of the forthcoming stages of the ELIADE array. These refined simulations facilitated the projection of ELIADE's performance at various developmental phases, providing valuable suggestions to researchers for the design of experiments involving ELIADE.

Facilities like the VEGA system in ELI-NP will extend the scope of nuclear studies beyond the current limitations. Nevertheless, the boundaries of experimentation will be defined by potential yields and the detection efficiencies of experimental setups. With these consid-

erations in mind, ELIADE was devised. Its large crystals and a close source-to-detector distance, leading to significantly heightened detection efficiencies. The incorporation of Compton-suppression shields further bolsters these efficiencies. However, the substantial detector size introduces the potential for false suppression or summation when dealing with high-energy gamma-ray events.

To address these challenges and fully exploit ELIADE's adaptable design, two distinct approaches: Summing schemes and Suppression schemes, were explored to optimise the detector's sensitivity under different conditions. The detector's simulation was utilised to evaluate and compare various summing and suppression schemes, including some that hadn't been previously considered. This approach was also employed to assess the performance of different ELIADE configurations. The implementation of these optimised schemes will enhance the detector's sensitivity, ultimately improving the precision of results obtained with ELIADE.

As discussed in chapter 7, experiments with lower energy (usually below 3 MeV), to obtain better results, it is suggested to use the Crystal summing scheme and Suppressed mode. However for experiments with higher gamma ray energies, especially from 9 MeV up to 19.5 MeV, it is suggested to use the Segments Add-back summing scheme and Segmented-Suppressed Anti-Compton rejection mode for analysis, to obtain the best results.

8.2 Future directions

As discussed before, it is essential to acknowledge that exploring every potential suppression scheme is unlikely. With an ELIADE detector having ten segments that can be either active or inactive for suppression in a given crystal interaction, designing a scheme comes down to making ten on/off decisions. However, this leads to a big number of possible combinations, which is too many to be systematically investigated (Figure 7.5). Let along in simulation, an extension of twenty segments Compton suppressor was also implanted for the initial design of ELIADE array.

The simulation developed and validated in this work is already integrated into the forth-

coming stages of developing other crucial algorithms essential for the experimental plan of the ELIADE array. Although the analysis on the optimisation schemes is limited to a single HPGe detector, the whole ELIADE array is also implanted in the simulation, however due to the lack of test and time, this part will be the next step to explore. The optimisation schemes can be extended, for example different detector configuration with collimations and passive shieldings. A larger energy range, especially on higher energies can be tested in the future, these can precise the selection on the combination of detector settings in experiments with VEGA system. The two optimisation schemes can be combined and tested when ELIADE is fully installed, in that case, a searching procedure can be developed and provide a clearer suggestion on the experiment design in future.

Bibliography

[Ago03] S. Agostinelliae. "Geant4-a simulation toolkit". In: *Nuclear Instruments and Methods in Physics Research Section A: Accelerators, Spectrometers, Detectors and Associated Equipment* (2003).

[AJ01] C.Rischel A.Rousse and J.C.Gauthier. "Femtosecond x-ray crystallography". In: *Rev. Mod. Phys. 73, 17 (2001)* (2001).

[Ama+09] S. Amano et al. "Several-MeV -ray generation at NewSUBARU by laser Compton backscattering". In: *Nucl. Instr. Meth. A, 602 (2009), pp. 337-341* (2009).

[AT63] F. Arutyunian and V. Tumanian. "The Compton effect on relativistic electrons and the possibility of obtaining high energy beams". In: *Phys. Lett. 4 (1963) 176-178* (1963).

[Axe+63] P. Axel et al. "New Resonances in Photon Transition Strength Functions". In: *Phys. Rev. Lett. 10, 299* (1963).

[Bal+17] D. L. Balabanski et al. "New light in nuclear physics: The extreme light infrastructure". In: *EPL 117 28001* (2017).

[Baz+99] D. Bazzacco et al. "Test of the MARS prototype segmented germanium detector, INFN and Dipartimento di Fisica, Padova, Itaty." In: *LNL Annual Reports* (1999).

[BB80] H. Beil and R. Bergere. "Report CEA-N-2144," in: *CEN, Saclay, France (1980)* (1980).

[Ben+11] A. Ben-Ismaïl et al. "Compact and high-quality gamma-ray source applied to 10 m-range resolution radiography". In: *Appl. Phys. Lett. 98, 264101 (2011)* (2011).

[BK87a] U.E.P. Berg and U. Kneissl. “Recent Progress on Nuclear Magnetic Dipole Excitations”. In: *Annu. Rev. Nucl. Part. Sci 37 (1987), 33-69* (1987).

[BK87b] U.E.P. Berg and U. Kneissl. “Recent progress on nuclear magnetic dipole excitations”. In: *Ann. Rev. Nucl. Part. Sci. 37 (1987) 33-69* (1987).

[Boh+84] D. Bohle et al. “New magnetic dipole excitation mode studied in the heavy deformed nucleus 156Gd by inelastic electron scattering”. In: *Phys. Lett. B, 137 (1984), p. 27* (1984).

[BW52] J.M. Blatt and V.F. Weisskopf. *Theoretical Nuclear Physics, chapter 12*. John Wiley Sons, Inc. New York, 1952.

[C+16] Richter C et al. “First clinical application of a prompt gamma based in vivo proton range verification system”. In: *Radiother Oncol. 2016 Feb;118(2):232-237* (2016).

[Can+74] C. Canali et al. “Hot hole anisotropic effect in silicon and germanium”. In: *Solid State Comm. 15 7 (1974) 1213* (1974).

[Car83] L.S. Cardman. “Photon Tagging, Present Practice and Future Prospects”. In: *Magnetic Spectrometer Workshop, Willianmsburg, Virginia, USA* (1983).

[CG53] S. A. Colgate and F. C. Gilbert. “Electron-Positron Annihilation in Flight”. In: *Phys. Rev. 89, 790* (1953).

[CM61] R .J. Cence and B .J. Moyer. “Photoprotons Produced by 245±15-Mev Gamma Rays on Carbon”. In: *Phys. Rev. 122, 1634* (1961).

[Cor+13] S. Corde et al. “Femtosecond x rays from laser-plasma accelerators”. In: *Rev. Mod. Phys. 85, 1* (2013).

[CZS16] D.J. Corvan, M. Zepf, and G. Sarri. “A high-energy, high-flux source of gamma-rays from all-optical non-linear Thomson scattering”. In: *Nuclear Instruments and Methods in Physics Research Section A: Accelerators, Spectrometers, Detectors and Associated Equipment* (2016).

[D+16] Rigamonti D et al. “Performance of the prototype LaBr3 spectrometer developed for the JET gamma-ray camera upgrade”. In: *Rev Sci Instrum 87, 11E717 (2016)* (2016).

[Dab89] W. Dabrowski. “Transport equations and Ramo’s theorem”. In: *Prog. Quant. Electr., 13 (1989), pp. 233-266* (1989).

[DB91] G. Desobry and A. Boyer. “Bremsstrahlung review: an analysis of the Schiff spectrum”. In: *Med Phys. 1991 May-Jun;18(3):497-505.* (1991).

[DD88] M.A. Delaplanquue and R.M. Diamond. “GAMMASPHERE, A National Gamma-Ray Facility”. In: *A Proposal, March 1988* (1988).

[Des70] R.Y. Deshpande. “Energy balance method for pulse shape determination in solid-state ionization chamber”. In: *Nucl. Instr. and Meth., 82 (1970), p. 51* (1970).

[Duc+92] G. Duchene et al. “Proc, Workshop on Large Gamma-Ray Detector Arrays (Chalk River, Ontario, Canada)”. In: *AECL 10613 (1992), 359-364* (1992).

[Duc+99] G. Duchene et al. “Clover: a new generation of composite Ge detectors”. In: *Nucl. Instrum. Methods A, 432 (1999), pp. 90-110* (1999).

[DZ13] T. Aumann D. Savran and A. Zilges. “Experimental studies of the pygmy dipole resonance”. In: *Prog. Part. Nucl. Phys. 70, 210 (2013). 10.1016* (2013).

[Ebe+01] J. Eberth et al. “MINIBALL A Ge detector array for radioactive ion beam facilities”. In: *Prog. Part. Nucl. Phys., 46 (2001), pp. 389-398* (2001).

[Ebe+90] J. Eberth et al. “Development of composite Ge detectors for EUROBALL”. In: *Nucl. Phys. A, 520 (1990), p. 669c* (1990).

[Ebe+92] J. Eberth et al. “Development of a composite Ge detector for EUROBALL”. In: *Prog. Part. Nucl. Phys., 28 (1992), p. 495* (1992).

[Ebe+96] J. Eberth et al. “ncapsulated Ge detectors: Development and first tests”. In: *Nucl. Instrum. Methods Phys. Res. A, 369 (1) (1996), pp. 135-140* (1996).

[Ebe+97] J. Eberth et al. “Development of segmented Ge detectors for future -ray arrays”. In: *Prog. Part. Nucl. Phys. 38 29–37* (1997).

[FAB+92] F.A.Beck et al. “The Clover detector”. In: *AECL–10613(v2)* (1992).

[FF61] C. R. Hatcher F. D. Seward and S. C. Fultz. “Measurement of the Annihilation-in-Flight Cross Section at 0° for 8.5-Mev Positrons”. In: *Phys. Rev. 121, 605* (1961).

[Fil+15] D. Filipescu et al. “Perspectives for photonuclear research at the Extreme Light Infrastructure - Nuclear Physics (ELI-NP) facility”. In: *2015 Eur. Phys. J. A 51 185* (2015).

[Fra+04] C. Fransen et al. “Parity assignments to strong dipole excitations of 92Zr and 96Mo”. In: *Phys. Rev. C 70, 044317* (2004).

[FRM69] F.R.Metzger. “Width of the 2.186-MeV 1 Level in Nd144”. In: *Phys. Rev. 187, 1700 (1969)* (1969).

[Ful+62] S. C. Fultz et al. “Photoneutron Cross-Section Measurements on Gold Using nearly Monochromatic Photons”. In: *Phys. Rev. 127, 1273 (1962)* (1962).

[Gal+18] S. Gales et al. “The extreme light infrastructure - nuclear physics (ELI-NP) facility: new horizons in physics with ultra-intense 10 PW lasers and 20 MeV brilliant gamma beams.” In: *Rep. Prog. Phys. 81, 094301* (2018).

[GJ98] G.Gilmore and J.Hemingway. “Practical Gamma-ray spectrometry”. In: *John Wiley Sons (1998), 220* (1998).

[Gl82] F.S. Goulding and D.A. landis. “IEEE Trans. Nucl. Sci.” In: *NS-29, 3 (1982) 1125-1140* (1982).

[Gla98] T. Glasmacher. “Coulomb excitation at intermediate energies”. In: *Annu. Rev. Nucl. Part. Sci., 48 (1998), p. 1* (1998).

[Gli+05] Y. Glinec et al. “High-Resolution -Ray Radiography Produced by a Laser-Plasma Driven Electron Source”. In: *Phys. Rev. Lett. 94, 025003* (2005).

[Gov+94] K. Govaert et al. “Polarised bremsstrahlung nuclear resonance fluorescence set-up at the 15 MeV linac in Gent”. In: *Nucl. Instrum. Methods Phys. Res A 337 (1994) 265* (1994).

[Gut90] D. Gutknecht. “Photomask technique for fabricating high purity germanium strip detectors”. In: *Nucl. Instrum. Methods Phys. Res. Sect. A, 288 (1) (1990), pp. 13-18* (1990).

[Haj+08] R. Hajima et al. “Proposal of nondestructive radionuclide assay using a high-flux gamma-ray source and nuclear resonance fluorescence”. In: *J. Nucl. Sci. and Tech, 45 (2008), p. 441* (2008).

[Hau08] E. Haug. “Bremsstrahlung cross-section with screening and Coulomb corrections at high energies”. In: *Radiation Physics and Chemistry 77(3):207-214* (2008).

[HF57] E. Hayward and E.G. Fuller. “Photon Self-Absorption and Scattering by the 15.1-Mev Level in C12”. In: *Phys. Rev. 106, 991* (1957).

[IL95] H. Ibach and H. Lüth. *Solid-State Physics, Second Edition*. Spring Verlag,p 444, 1995.

[JA62] P. A. Tipler J.S. O'Connell and P. Axel. "Elastic Scattering of 11.5—17.7-Mev Photons by Au Measured with a Bremsstrahlung Monochromator". In: *Phys. Rev. 126, 228* (1962).

[Jon+95] P.M. Jones et al. "Calibration of the new composite CLOVER detector as a compton polarimeter for the eurogam array". In: *Nucl. Instrum. Methods A, 362 (1995), p. 556* (1995).

[JR83] C. Jacoboni and L. Reggiani. "The Monte Carlo method for the solution of charge transport in semiconductors with applications to covalent materials". In: *Rev. Mod. Phys. 55, 645* (1983).

[KB01] T. Kröll and D. Bazzacco. "Simulation and analysis of pulse shapes from highly segmented hpge detectors for the gamma-ray tracking array mars". In: *Nucl.Instrum.Meth.A 463 (2001) 227-249* (2001).

[Kne+75] U. Kneissl et al. "The quasimonoenergetic photon facility at the Giessen 65 MeV electron linear accelerator". In: *Nucl. Instrum. Methods 127 1 (1975) 1-10* (1975).

[Kne+96] U. Kneissl et al. "Investigation of nuclear structure by resonance fluorescence scattering". In: *Prog. Part. Nucl. Phys., 37 (1996), pp. 349-433* (1996).

[Kne90] U. Kneissl. "Photoexcitation of low-lying, isovector 1+ states in deformed nuclei". In: *Prog. Part. Nucl. Phys. 24 (1990), p. 41* (1990).

[Kno+82] J. Knowles et al. "A high resolution bremsstrahlung monochromator for photonuclear experiments Author links open overlay panel". In: *Nucl. Instrum. Methods Phys. Res. 193 (1982) 463-483* (1982).

[Kno10] G. F. Knoll. *Radiation Detection and Measurement, 4th Edition*. John Wiley Sons, Inc., 2010.

[Kos+10] K. Kosaka et al. "Angular Distribution of Bremsstrahlung from Copper and Tungsten Targets Bombarded by 18, 28, and 38MeV Electrons". In: *Nucl. Sci. Tech. 47 (2010), 286-294* (2010).

[KZ12] U. Kneissl and A. Zilges. "The nuclear resonance fluorescence method". In: *Landolt-Börnstein: Group I: Elementary Particles, Nuclei and Atoms (Springer-Verlag, Berlin, Heidelberg, 2012), Vol. 25B, pp. 30–47* (2012).

[Las+87] R.M. Laszewski et al. "Giant M1 resonance in 90Zr". In: *Phys. Rev. Lett. 59, 431* (1987).

[Las+88] R.M. Laszewski et al. "Distribution of M1 transitions in 208Pb". In: *Phys. Rev. Lett. 61 (1988) 1710-1712* (1988).

[Las86] R. Laszewski. "Photon interactions below 9 MeV in Ba and Ce". In: *Phys.Rev.C 34 (1986) 1114-1116* (1986).

[Leo94] R. Leo. *Techniques for Nuclearand Particle Physics Experiments, Second Edition*. Spring Verlag, p 35, 1994.

[Li+06] T.C. Li et al. "First evidence for spin-flip M1 strength in 40Ar". In: *Phys. Rev. C 73, 054306* (2006).

[Lin+91] S. Lindenstruth et al. "Measurements and simulations of low energy, thick target bremsstrahlung spectra". In: *Nucl. Instrum. Methods Phys. Res. A. 300 2 (1991), 293-296* (1991).

[Lit+98] V.N. Litvinenko et al. "First UV/visible lasing with the OK-4/Duke storage ring FEL". In: *Nucl. Instr. Meth. Phys. Res. A407, 8* (1998).

[LM96] V.N. Litvinenko and J.M.J. Madey. "Intense Compton -ray source from the Duke storage ring FEL". In: *Nucl. Instr. Meth. Phys. Res. A375, 580* (1996).

[Loh+13] B. Loher et al. "The high-efficiency -ray spectroscopy setup 3 at HIS". In: *Nucl. Instr. Meth. Phys. Res. A723, 136* (2013).

[Met59] R. R. Metzger. "Resonance fluorescence in nuclei". In: *Prog. in Nucl. Phys. 7, 54-88* (1959).

[Mih+00] L. Mihailescu et al. "Influence of anisotropic electron drift velocity on the signal shapes of closed-end HPGe detectors". In: *Nucl. Instr. and Meth., A 447 (2000), p. 350* (2000).

[Mil63] R.H. Milburn. "Electron Scattering by an Intense Polarized Photon Field". In: *Phys. Rev. Lett. 10, 75* (1963).

[MO69] M. Martini and G. Ottaviani. “Ramo’s theorem and the energy balance equations in evaluating the current pulse from semiconductor detectors”. In: *Nucl. Instr. and Meth. 67, 1 (1969) 177-178* (1969).

[Moo51] P. B. Moon. “Resonant nuclear scattering of gamma-rays: Theory and preliminary experiments”. In: *Proc. Phys. Soc. A64, 76* (1951).

[Mor+82] R. Moreh et al. “Strong E2 and M1 transitions in 40Ca”. In: *Phys. Rev. C 25, 1824* (1982).

[Mös58] R.L. Mössbauer. “Kernresonanzfluoreszenz von Gammastrahlung in Ir191”. In: *Zeitschrift für Physik volume 151, pages 124–143* (1958).

[MS58] L. Grodzins M. Goldhaber and A.W. Sunyar. “Helicity of Neutrinos”. In: *Phys.Rev. 109 (1958) 1015-1017* (1958).

[MW51] M. May and G. Wick. “On the polarization of high energy bremsstrahlung and of highenergy Pairs”. In: *Phys. Rev., 84 (1951), p. 265* (1951).

[Nat63] M.I. Nathan. “Anisotropy of the conductivity of n-type germanium at high electric fields”. In: *Phys. Rev., 130 (1963), p. 2201* (1963).

[NS79] P.J. Nolan and J.F. Sharpey-Schafer. “The measurement of the lifetimes of excited nuclear states”. In: *Rep. Prog. Phys. 42 1* (1979).

[NVZ14] N.V.Zamfir. “Nuclear Physics with 10 PW laser beams at Extreme Light Infrastructure – Nuclear Physics (ELI-NP)”. In: *The European Physical Journal Special Topics volume 223, pages 1221–1227 (2014)* (2014).

[OCo+62] J.S. OConnell et al. “Elastic Scattering of 11.5-17.7-Mev Photons by Au Measured with a Bremsstrahlung Monochromator”. In: *Phys.Rev. 126 (1962) 228-239* (1962).

[OCo61] J.S. OConnel. “Simple Broad-Range Magnetic Spectrometer”. In: *Rev. Sci. Instrum, 32 (1961) 1314* (1961).

[Ohg+94] H. Ohgaki et al. “Linearly polarized photons from Compton backscattering of laser light for nuclear resonance fluorescence experiments”. In: *Nucl. Instr. Meth. Phys. Res.A353, 384* (1994).

[Ott+75] G. Ottaviani et al. “Charge carrier transport properties of semiconductor materials suitable for nuclear radiation detectors”. In: *IEEE Trans. on Nucl. Sci., 22 (1975), pp. 192-204* (1975).

[PB02] N. Pietralla and Z. Berant. “Parity Measurements of Nuclear Levels Using a Free-Electron-Laser Generated g-Ray Beam”. In: *Phys. Rev. Lett. 88, 012502* (2002).

[Pei92a] A. Peisert. “INFN report on Silicon microstrip detectors”. In: *(1992) 28)* (1992).

[Pei92b] A. Peisert. “Silicon microstrip detectors”. In: *INFN report* (1992).

[PF94] F.A. Beck P.J. Nolan and D.B. Fossan. “Large arrays of escape-suppressed gamma-ray detectors”. In: *Annu. Rev. Nucl. Part. Sci. 44 (1994) 561* (1994).

[Pie+02a] N. Pietralla et al. “Identification of the J=1 two-phonon state of 88Sr”. In: *Phys. Rev. C 65, 047305* (2002).

[Pie+02b] N. Pietralla et al. “Parity measurements of nuclear dipole excitations using FEL-generated -rays at HIS”. In: *Nucl. Instr. Meth. Phys. Res. A483, 556-559* (2002).

[Pie+09] N. Pietralla et al. “Competition between excited core states and 1 single-particle excitations at comparable energies in 207Pb from photon scattering”. In: *Phys. Lett. B 681, 134* (2009).

[PJ 85] P.J. Twin P.J. Nolan D.W. Gifford. “The performance of a bismuth germanate escape suppressed spectrometer”. In: *Nucl. Instr. and Meth., A236 (1985), p. 95* (1985).

[PJ60] R. V. Pound and G. A. Rebka Jr. “Apparent Weight of Photons”. In: *Phys. Rev. Lett. 4, 337–341* ((1960)).

[Po03] N. Pietralla and others. “Nuclear Structure Physics with a Free Electron Laser, in Frontiers of Nuclear Structure 2002, P. Fallon and R. Clark Eds.” In: *AIP Conference Proceedings 656, American Institute of Physics, New York, pp. 365-372* (2003).

[Pre+99] W.H. Press et al. “Numerical Recipes in C, The Art of Scientific Computing”. In: *Cambridge University Press (1999) Second Edition, 549* (1999).

[Rad88a] V. Radeka. “Low Noise Techniques in Detectors”. In: *Nucl. Part. Sci 38, (1988) 217-277* (1988).

[Rad88b] V. Radeka. “Low Noise Techniques in Detectors”. In: *Nucl. Part. Sci 38, (1988) 224* (1988).

[Reg+77] L. Reggiani et al. “Hole drift velocity in germanium”. In: *Phys.Rev.B 16 (1977) 2781* (1977).

[Ric95] A. Richter. “Probing the nuclear magnetic dipole response with electrons, photons and hadrons”. In: *Prog. Part. Nucl. Phys, 34 (1995) 261* (1995).

[Riz+16] U. Rizwan et al. “Characteristics of GRIFFIN high-purity germanium clover detectors”. In: *Nucl. Instrum. Methods A, 820 (2016), pp. 126-131, 10.1016/j.nima.2016.03.016* (2016).

[RKs12] R.Kshetri. “Modeling of clover detector in addback mode”. In: *JINST 7 P07008* (2012).

[Roc+72] G. Roche et al. “Bremsstrahlung Cross-Section Formula Including a High-Order Coulomb Correction”. In: *Phys. Rev. A 5, 2403* (1972).

[Sav+05] D. Savran et al. “Parity assignments in 172,174Yb using polarized photons and the K quantum number in rare earth nuclei”. In: *Phys. Rev. C 71, 034304* (2005).

[Sch+05] R. Schwengner et al. “The photon-scattering facility at the superconducting electron accelerator ELBE”. In: *Nucl. Instrum. Methods Phys. Res. A.555 (2005), 211-219* (2005).

[Sch+07] R. Schwengner et al. “Dipole response of 88Sr up to the neutron-separation energy”. In: *Phys. Rev. C 76, 034321* (2007).

[Sch+94] B. Schlitt et al. “A Sectored Ge-Compton-Polarimeter for Parity Assignments in Photon Scattering Experiments”. In: *Nucl. Instr. a. Meth. in Phys. Res., A337 (1994), pp. 416-426* (1994).

[Sch+98] G.J. Schmid et al. “Gamma-ray polarization sensitivity of the Gammasphere segmented germanium detectors”. In: *Nucl. Instr. Meth. A417 (1998) 95-110* (1998).

[Sch46] L.I. Schiff. “Resonance Fluorescence of Nuclei”. In: *Phys. Rev. 70, 761* (1946).

[Sch51] L.I. Schiff. “Energy-Angle Distribution of Thin Target Bremsstrahlung”. In: *Phys. Rev. 83, 252* (1951).

[Scr+05] H. Scraggs et al. “TIGRESS highly-segmented high-purity germanium clover detector”. In: *Nucl. Instrum. Methods Phys. Res. A 543.2 431-440* (2005).

[She+99] S.L. Shepherd et al. “Measurements on a prototype segmented Clover detector”. In: *Nucl. Instr. and Meth. in Phys. Res. A434, 373-386 (1999)* (1999).

[She98] Sarah Shepherd. *Isolated Hit Probability and Linear Polarisation*. 1998. URL: https://ns.ph.liv.ac.uk/posters/sls/poster.html. (accessed: 01.02.2023).

[Shi55] M. Shibuya. “Hot Electron Problem in Semiconductors with Spheroidal Energy Surfaces”. In: *Phys. Rev. 99, 1189* (1955).

[Sim+00] J. Simpson et al. “The EXOGAM Array: A Radioactive Beam Gamma-Ray Spectrometer”. In: *APH N.S., Heavy Ion Physics 11 (2000) 159-188* (2000).

[Söd+21] P.-A. Söderström et al. “Characterization of a plutonium–beryllium neutron source”. In: *Applied Radiation and Isotopes 167* (2021).

[SRa39] S.Ramo. “Currents Induced by Electron Motion”. In: *P.I.R.E., 27 (1939), p. 584* (1939).

[Tan+20] K. A. Tanaka et al. “Current status and highlights of the ELI-NP research program”. In: *Matter and Radiation at Extremes, 2020, 5(2) 024402* (2020).

[TL11] N. Tsoneva and H. Lenske. “Pygmy quadrupole resonance in skin nuclei”. In: *Phys. Lett. B 695, 174 (2011).10.1016* (2011).

[TMu76] T.Mukoyama. “Range of electrons and positrons”. In: *Nucl. Instr. Meth 134 (1976) 125-127* (1976).

[Ton+10] A.P. Tonchev et al. “Spectral Structure of the Pygmy Dipole Resonance”. In: *Phys. Rev. Lett 104, 072501* (2010).

[Ur+16] C. Ur et al. “Nuclear Resonance Fluorescence Experiments at ELI-NP”. In: *Romanian reports in physics 68* 506 (2016).

[UZ06] N. Pietralla U. Kneissl and A. Zilges. “Low-lying dipole modes in vibrational nuclei studied by photon scattering”. In: *J. Phys. G: Nucl. Part. Phys. 32 R217* (2006).

[UZ96] H.H. Pitz U. Kneissl and A. Zilges. “Investigation of nuclear structure by resonance fluorescence scattering”. In: *Prog. Part. Nucl. Phys. 37, 349* (1996).

[Vas70] D.G. Vass. “The charge collection process in semiconductor radiation detectors”. In: *Nucl. Instr. and Meth., 86 (1970), p. 5* (1970).

[Vey+79] A. Veyssière et al. “The quasi-monochromatic photon beam used in photoneutron experiments from 20-120 MeV at the 600 MeV Saclay Linac”. In: *Nucl. Instr. and Meth., 165 (1979), p. 417* (1979).

[Wel+09] H.R. Weller et al. “Research opportunities at the upgraded HIS facility”. In: *Prog. Part. Nucl. Phys 62, 257* (2009).

[Whi05] J. C. Whitaker. *The Electronice Handbook*. Crc Press, Book., 2005.

[Wie+81] K. Wienhard et al. “Parities of Strong Dipole Ground State Transitions in 88Sr”. In: *Zeitschrift für Physik A Atoms and Nuclei volume 302, pages 185–186 (1981)* (1981).

[Wil+96] M. Wilhelm et al. “The response of the euroball cluster detector to -radiation up to 10 MeV”. In: *Nucl. Instrum. Methods Phys. Res. A, 381 (2–3) (1996), pp. 462-465* (1996).

[WM53] J.W Weil and B.D. McDaniel. “The production of protons from carbon by monoenergetic gamma rays”. In: *Phys. Rev., 92 (1953), p. 391* (1953).

[Yu+19] J.Q. Yu et al. “PCreation of Electron-Positron Pairs in Photon-Photon Collisions Driven by 10-PW Laser Pulses”. In: *Phys. Rev. Lett. 122, 014802* (2019).

[Zil+22] A. Zilges et al. “Photonuclear reactions—From basic research to applications”. In: *Prog. Part. Nucl. Phys. 122 (2022), Article 103903* (2022).